

# Wind-Generated Waves in Fjords and Coastal Areas



Konstantinos Christakos

Thesis for the degree of Philosophiae Doctor (PhD)  
University of Bergen, Norway  
2021

UNIVERSITY OF BERGEN



# Wind-Generated Waves in Fjords and Coastal Areas

Konstantinos Christakos



Thesis for the degree of Philosophiae Doctor (PhD)  
at the University of Bergen

Date of defense: 02.09.2021

© Copyright Konstantinos Christakos

The material in this publication is covered by the provisions of the Copyright Act.

Year: 2021

Title: Wind-Generated Waves in Fjords and Coastal Areas

Name: Konstantinos Christakos

Print: Skipnes Kommunikasjon / University of Bergen

# Scientific environment

The study was carried out at the Geophysical Institute, University of Bergen, Norway, the Division for Oceanography and Marine Meteorology at the Norwegian Meteorological Institute, Bergen, Norway, and the Marine Research Unit at the Finnish Meteorological Institute, Helsinki, Finland. The author has been enrolled in the Norwegian Research School on Changing Climates in the coupled Earth System (CHESS) throughout this study. The Norwegian Public Roads Administration funded the PhD position under the Coastal Highway Route E39 project. The research at the Finnish Meteorological Institute was partly financed by the EU mobility program (Erasmus+).



**Norwegian  
Meteorological  
Institute**



**ILMATIETEEN LAITOS  
METEOROLOGISKA INSTITUTET  
FINNISH METEOROLOGICAL INSTITUTE**



**UNIVERSITY OF BERGEN**



# Acknowledgements

First and foremost, I would like to express my gratitude to my main supervisor, Birgitte R. Furevik, and co-supervisors, Øyvind Breivik and Laura Tuomi, for sharing their knowledge and guiding me through this PhD project. Birgitte, I would like to thank you for introducing me to coastal wave modelling, fruitful discussions, and for being very supportive. Øyvind, thank you for the thoughtful discussions and your help in decision making. Laura, thank you for sharing your experience in coastal modelling and for your great hospitality during my research stays at the Finnish Meteorological Institute. I was privileged to work at the Division of Oceanography and Marine Meteorology at the Norwegian Meteorological Institute and the Marine Research Unit at the Finnish Meteorological Institute which provided me a great scientific environment to pursue my research. I thank the Norwegian Public Roads Administration for funding this PhD under the Coastal Highway Route E39 project; a special thanks to Jørn Arve Hasselø and Magne Gausen for a great collaboration. I want to express my appreciation to Anne Karin Magnusson and Magnar Reistad for sharing some historical information about wave modelling in Norway. Furthermore, I would like to thank Jan-Victor Björkqvist, Ole Johan Aarnes, and Mika Malila for valuable scientific discussions. I would also like to thank Martin Mathiesen and Torleif Lothe for introducing me to the met-ocean field back in 2013. Special thanks to my friends, Leonidas Tsopouridis, George Varlas and Ioannis Cheliotis, for our discussions and for sharing experiences during this journey. Last but not least, I would like to thank my family for their support and encouragement through my studies.



# Abstract

Accurate predictions of coastal and fjord wave conditions are vital for several sectors such as fish farming, fisheries, as well as coastal and maritime infrastructure. In complex coastlines such as the Norwegian coast with thousands of islands, islets, and narrow fjords, accurate wave prediction is challenging. In addition to the necessity of using a state-of-the-art nearshore wave model with high spatial resolution, there is a need for high quality and resolution of forcing fields such as wind, surface currents and bathymetry. Moreover, in such areas, satellite remote sensing techniques are not reliable due to the proximity to the land. The observations are thus mainly limited to point measurements, e.g., wave buoys. In recent years, the Norwegian Public Roads Administration has conducted one of the largest measurement campaigns for wind, wave, and current conditions along the Norwegian coast. The campaign aims to obtain the essential data to construct a ferry-free E39 highway route. It provides observations for advanced met-ocean studies in coastal areas and fjords that previously have not been possible. Using these unique measurements together with a high-resolution wave simulation system based on a spectral wave model, this thesis advances our knowledge about coastal and fjord waves.

Papers I-III investigate wind-generated gravity waves in a complex coastal system with narrow fjords, partly exposed to some of the most energetic offshore waves at the western coast of Norway in the Norwegian Sea. In Paper I, we investigate the importance of wind forcing on coastal and fjord wave conditions. The results indicate that a high-resolution wind forcing is essential to obtain a realistic wind field in complex fjord topography. The best model performance is found at the exposed to open sea locations using high-resolution wind forcing. Local phenomena such as lee effects and wind channelling significantly affect the wave estimates. During extreme cases, simulations without wind forcing are unable to predict the wave height accurately in any of the fjord locations. Paper II focuses on the performance of three different deep-water source term formulations in narrow fjords, known as the Komen approach (based on a pressure-pulse white-capping), the saturation-based white-capping approach, and the observation-based scheme (ST6). The results pinpoint that the fetch geometry has a distinct effect on the model's accuracy at inner fjord locations. The saturation-based white-capping approach performs most accurate in fjords with mixed swell–wind sea conditions. In narrow fetch geometries without swell, all source term packages overestimate the wave energy, with ST6 showing the highest sensitivity to fetch geometry and local wind variations. At inner locations and during strong wind conditions, the results illustrate that the white-capping in ST6 is relatively weak compared to its strong wind input. In Paper III, we quantify the impact of surface currents on wave conditions in fjords and coastal areas. The results highlight the significant role of ocean surface

currents on wave modulation at inner fjords. In such areas, the incorporation of ocean forcing considerably improves the wave height estimates. Wave-current interaction is also found to have an effect on wave characteristics such as the relative frequency, spectral bandwidth, and directional spreading in narrow fjords.

# Outline

This thesis consists of an introductory part (Chapter 1 to 4) that provides the framework for three scientific papers. Chapter 1 presents the introduction and objectives. The scientific background of spectral wave modelling and met-ocean observations in fjords and coastal areas is given in Chapter 2. Chapter 3 provides a summary of the main results, as well as the concluding remarks. Perspectives and outlook are given in Chapter 4. The three scientific papers (Chapter 5) included in the thesis are:

- I. **Christakos, K.**, B.R. Furevik, O.J. Aarnes, Ø. Breivik, L. Tuomi, and Ø. Byrkjedal (2020), *The importance of wind forcing in fjord wave modelling*, Ocean Dynamics, 70, 57–75.
- II. **Christakos, K.**, J.V. Björkqvist, L. Tuomi, B.R. Furevik, and Ø. Breivik (2021), *Modelling wave growth in narrow fetch geometries: The white-capping and wind input formulations*, Ocean Modelling, 157, 101730.
- III. **Christakos, K.**, J.V. Björkqvist, Ø. Breivik, L. Tuomi, B.R. Furevik, and J. Albretsen, *The impact of surface currents on the wave climate in narrow fjords*, Ocean Modelling, *under review*.

## Additional contributions

Apart from the papers listed above for evaluation of the PhD thesis, I have (co-)authored other relevant peer-reviewed publications:

- A. **Christakos, K.**, G. Varlas, I. Cheliotis, C. Spyrou, O.J. Aarnes, and B.R. Furevik (2020), *Characterization of Wind-Sea- and Swell-Induced Wave Energy along the Norwegian Coast*, Atmosphere, 11, 166.
- B. Stefanakos, C.N., B.R. Furevik, Ø. Knutsen, and **K. Christakos** (2020), *Nearshore Wave Modelling in a Norwegian Fjord*, Proceedings of the ASME 2020 39th International Conference on Ocean, Offshore and Arctic Engineering, Volume 6B: Ocean Engineering.



# Contents

<b>Scientific environment</b>	<b>i</b>
<b>Acknowledgements</b>	<b>iii</b>
<b>Abstract</b>	<b>v</b>
<b>Outline</b>	<b>vii</b>
<b>1 Introduction</b>	<b>1</b>
1.1 Wave forecasting and hindcasting in Norway . . . . .	2
1.1.1 Open ocean . . . . .	2
1.1.2 Fjords and coastal areas . . . . .	4
1.2 Objectives . . . . .	6
<b>2 Scientific background</b>	<b>7</b>
2.1 Modelling of spectral waves . . . . .	7
2.1.1 Variance density spectrum . . . . .	7
2.1.2 Kinematics . . . . .	8
2.1.3 Action balance equation . . . . .	8
2.2 Wave conditions in fjords and coastal areas . . . . .	13
2.2.1 The wave climate on the west coast of Norway . . . . .	13
2.2.2 Area of investigation . . . . .	13
2.2.3 Modelling system . . . . .	13
2.2.4 Met-ocean observations . . . . .	15
<b>3 Summary of the papers</b>	<b>21</b>
<b>4 Perspectives and outlook</b>	<b>27</b>
<b>5 Scientific results</b>	<b>31</b>



# Chapter 1

## Introduction

As wind blows over the ocean surface, it generates surface waves (vertical motions of the ocean surface). When the restoring force is gravity, they are known as wind-generated gravity waves or surface gravity waves. There are two types of these waves: wind sea (short-crested and irregular waves) and swell (long-crested and regular waves). Wind sea is under the influence of the local wind. When waves leave the generation area, or their phase velocity exceeds the local wind speed, they are called swell.

Precise prediction of surface gravity waves is essential for safe marine navigation. Coastal areas often need extra attention from seafarers due to islands, islets and variation in depth that affect the wave conditions through different processes, such as refraction, shoaling, and depth-induced breaking. Both traditional coastal activities (e.g., fish farming, fisheries, tourism, and maritime transport) and new developments, including floating urban areas, wind turbines, wave energy converters, floating solar panels, floating bridges, and autonomous ships, demand reliable and detailed information on wave conditions. This information is essential for designing structures, estimating load and response, and finding the optimal weather windows for operations.

According to the National Transport Plan 2014-2023 (*The Norwegian Ministry of Transport and Communications*, 2013), the Norwegian government has the ambition to develop a modern transport system for easier, faster, and safer travel and transport of goods. The Coastal Highway Route E39 project is a central part of this plan. The project, which the Norwegian Public Roads Administration carries out, aims to design and construct bridges and tunnels for fjord-crossings creating a ferry-free E39 highway route (*Dunham*, 2016). In addition to a large campaign for met-ocean observations in several fjords along the route between Kristiansand and Trondheim, the project requires accurate high-resolution met-ocean estimates to be used for load and response calculations. The simulations of surface waves are vital for floating bridge design. For instance, penetration of low-frequency waves such as swell in fjords can induce large vertical displacements/oscillations in such structures (*Aalberg*, 2017). Moreover, *Dai et al.* (2021) associated the wave field inhomogeneity in a fjord with a possible response and fatigue damage of a floating bridge.

During the last decades, predictions of surface waves based on spectral models (see Section 2.1) have achieved a high degree of reliability in open seas. We can hence predict with higher accuracy integrated wave parameters, including significant wave height, wave period, and direction up to a week in advance (e.g., *Bidlot et al.*, 2002;

*Janssen*, 2008; *Janssen and Bidlot*, 2018). This achievement has been attained mainly by (i) the improved quality of the wind input due to the systematic development of numerical weather prediction models, (ii) the improvements in the deep-water source terms (i.e. wind input, white-capping and quadruplet wave-wave interactions, see Section 2.1.3) of spectral models (*Babanin*, 2011), and (iii) an increased number of available wave measurements from in situ sensors (e.g., wave buoys) to remote sensing (e.g., satellite altimeters) that have been extensively used to calibrate the spectral models (e.g., *Amarouche et al.*, 2019; *Cavaleri and Sclavo*, 2006; *Martínez-Asensio et al.*, 2013).

Despite the significant improvements of wave predictions in the open sea, their accuracy is still insufficient in the coastal and semi-enclosed seas (*Cavaleri et al.*, 2018). The models have not been extensively validated in complex coastal systems, and their predictions are overall less reliable compared to the respective ones for the open sea. For validation/calibration purposes, coastal measurements are limited mainly to in situ observations due to restrictions of satellite remote sensing techniques (proximity to land). In situ measurements are expensive, usually restricted in number and limited in duration in coastal areas. In addition, this type of measurements at a nearshore site describes conditions in a limited area, a few hundred meters around the point of observation, since the wave conditions can vary significantly in space due to local characteristics such as exposure to open sea, presence of islands, islets, varying depth, tidal currents, and variation in wind field induced by topographic effects. Given the varying topography along complex coastlines, such as the Norwegian coast, model results are expected to be valid for limited (geographically-restricted) areas, and generalisation of conclusions must be dealt with caution.

## 1.1 Wave forecasting and hindcasting in Norway

### 1.1.1 Open ocean

From the first half of the 20th century, the Norwegian Meteorological Institute (MET Norway) and its regional department in Bergen, known as *Vêrvarslinga på Vestlandet*, was sending gale warnings using telegraph/radio (*kystradiostasjon*) for fishing banks in the open seas. Even if these warnings were not based on actual wave predictions, they indicated dangerous sea states. The beginning of the Norwegian oil era in the 1970s led to significant developments in wave forecasting and hindcasting. By the end of the 1960s, Odd Haug from MET Norway created a hybrid model that combines swell components with a parametric wind sea evolution, known as the Norwegian Wave Model, NOWAMO (*Guddal*, 1985; *Haug*, 1968). Apart from forecasting, this model contributed to the development of the first Norwegian wave hindcast (*Haug*, 1981). In 1982, MET Norway, supported by the oil company Statoil (now Equinor), started implementing the WINCH model, which was based on the second-generation wave model (2G) developed by Oceanweather Inc. (*Oceanweather Inc.*, 2018). The model was run in a grid resolution of 75 km in the North Sea and most of the Norwegian Sea and the Barents Sea nested into a 150 km grid covering a large part of the North Atlantic. The model was used for operational wave forecasting until 2001. Besides, MET Norway used the WINCH model to produce historical data over a period of about

50 years starting from 1955 and covering areas of the Norwegian continental shelf (*Skjæveland and Sætre, 2016*).

On December 12, 1990, a severe storm passed over the North Sea, with significant wave heights reaching up to 13 m at the Ekofisk oil and gas site (located in the central North Sea). At that time, it was already known for several years that the seafloor under Ekofisk's platforms was subject to subsidence. The sea floor had sunk by 4 meters and compensatory actions had been taken (e.g., extending platform legs by 6 meters in 1986, and building a large wall around the central platform, completed in 1989) to compensate for the deck height being closer to the sea surface and thereby being more exposed to extreme wave crests. However, the considerable storm damages on the Ekofisk platforms highlighted the need for both accurate forecasts and advanced measurements. The operator at that time, Phillips Petroleum Norway (now ConocoPhillips), contacted MET Norway to develop a special forecasting service for Ekofisk, known as the EXWW (Ekofisk eXtreme Wave Warning) project. Until today, the system has been sending warnings when high waves are expected, where the target parameter is a statistical maximum crest height (formulae based on *Forristall (2000)*). The parameter also includes variations of water level due to tides and atmospheric effects. Met-ocean measurements have been of paramount importance for the oil and gas industry. The EXWW system has made Ekofisk one of the most well-equipped locations in the open seas, including a wave buoy, two altimeter systems based on laser and radar techniques, a marine radar, and stereo cameras.

In 1999, MET Norway started using operationally the third-generation wave model WAM (*The Wamdi Group, 1988*). The first operational model (based on WAM) was known as the WAM50 (50 km grid), covering most of the North Atlantic and running parallel to WINCH for some years. In 2007, WAM10 became operational with a finer grid (10 km) for the Nordic Seas and boundary conditions from WAM50 (*Carrasco and Gusdal, 2014*). Two years later, MET Norway started running operationally the WAM model in a domain that covered areas off the Scandinavian coast (4 km resolution) and used boundaries from WAM10 (*Carrasco and Gusdal, 2014*). In 2015, WAM4 with a 4 km grid covering the Nordic Seas started running operationally, replacing WAM10. The WAM model was also applied for hindcast purposes, such as in the development of the NORA10 hindcast (*Reistad et al., 2011*) which was initiated by the oil and gas industry. NORA10 has been widely used not only in offshore sector but also in climate and renewable energy studies (e.g., *Aarnes et al., 2012, 2017; Bruserud et al., 2016; Furevik and Haakenstad, 2012; NORSOK N-003:2017, 2017; Semedo et al., 2014; Solbrekke et al., 2020; Varlas et al., 2017*). The hindcast covers the Nordic seas with a 10 km grid, nested into a 50 km grid covering most of the North Atlantic. In 2020, the NORA EI, a revised version of NORA10, became openly available (*Haakenstad et al., 2020*). MET Norway is currently producing a new version, known as NORA3, with a 3 km grid resolution based on the WAM model.

Wave observations have played a key role in wave model developments in the open seas. Wave buoys, altimeters or platform-based remote sensing sensors are often deployed in the vicinity of oil platforms/rigs to provide detailed observations for model validation and advance our knowledge on wave conditions in the open seas e.g., extreme waves (*Cavaleri et al., 2017; Donelan and Magnusson, 2017; Dysthe et al., 2008; Magnusson and Donelan, 2013; Magnusson et al., 2019*).

## 1.1.2 Fjords and coastal areas

Advancements in coastal wave predictions arose much later compared to offshore areas. Wave models developed for open seas have been considered until recently as too computationally expensive to be operated on fine coastal grids. In the second half of the 20th century, several wave propagation models such as the spectral refraction/refraction–diffraction models (e.g., *Isobe*, 1987; *Izumiya and Horikawa*, 1987; *Kirby*, 1986; *Le Méhauté and Wang*, 1982; *Longuet-Higgins*, 1957; *O’Reilly and Guza*, 1993) were developed. These models were limited to coastal areas where the assumption of spatially homogeneous offshore boundary wave spectrum was valid and local wave growth was limited. Thus, the first prediction system for coastal waves in Norway (*Torsethaugen et al.*, 1998) was established in 1997 by SINTEF and MET Norway, and it was based on a refraction (ray-tracing) model following the study by *Mathiesen* (1987). The forecast system was set up for the coastal area near Stad in the western Norwegian coast, providing prediction of wave parameters such as wave height, period and direction, and a ray-tracing diagram with some associated text.

In the evening of 26 November 1999, the tragic accident of the high-speed ferry MS “Sleipner” (*Eidesen et al.*, 2000) became the starting point for the first operational wave forecast along the whole Norwegian coast. The ferry ran aground on a rock on its way from Stavanger to Bergen, close to Ryvarden lighthouse (north of Haugesund). It is considered the most severe ferry accident in Norwegian history, with 16 people dead and 69 being rescued from the sea. The accident happened during a strong wind from the southwest, with wave heights exceeding the ferry’s limitations. After the accident, the government stated that wave forecasts should be developed in coastal areas with high-speed traffic. Thus, the Polytec R&D Institute (now NORCE), with funding from the Norwegian Coastal Administration, started the development of the fine-scale (100 m) wave forecast along the Norwegian coast (*Segtnan et al.*, 2013). In collaboration with MET Norway, the system, known as CoastEx covering a few selected areas, became operational in 2003. The first CoastEx forecast was run by MET Norway based on a look-up table, input from the offshore wave forecast (WAM), and pre-generated maps of integrated wave parameters (wave height, period and direction). The maps had been created by Polytec R&D Institute based on the steady-state wave model STWAVE (*Massey et al.*, 2011). The CoastEx approach is based on a diagnostic model assuming (i) steady-state (i.e. the wind has remained steady for enough long time for the wave field to reach fetch-limited or fully developed conditions) and (ii) a uniform wind field over the domain. This approach is suitable for small coastal domains without significant variations in the wind field and the offshore (boundary) waves.

Hence, MET Norway used a dynamical downscaling technique to develop its own coastal forecast in 2005. It was based on a high resolution (500 m) prognostic spectral model SWAN (*Booij et al.*, 1999) nested into a coarser wave model (WAM), referred to as WAM/SWAN (*Breivik et al.*, 2009; *Furevik and Reistad*, 2006; *Gusdal et al.*, 2010). The term “dynamical downscaling” means that the boundary conditions to SWAN were provided by WAM as a two-dimensional wave spectrum. The SWAN was running in a non-stationary mode and it was forced by fine resolution (4–5 km) wind. The forecast was running operationally for the areas of Trondheimsleia and Karmøy, at the western Norwegian coast.

During 2012–14, the project *MyWave: A pan-European concerted and integrated*

*approach to operational wave modelling and forecasting a complement to GMES My-Ocean services* coordinated by the MET Norway led to the development of the operational coastal wave product, known as WAM800. The forecast is based on the spectral model WAM using boundaries from a coarser model grid (WAM4) and wind forcing (AROME2.5/MEPS with 2.5 km grid resolution) to calculate the wave conditions. The whole coast of Norway is covered by 5 domains with a fine grid of 800 m. The WAM800 has been the coastal operational model at MET Norway since 2015.

During the last decade, the CoastEx system has been developed covering the whole Norwegian coast (in 2017) and including, in addition to integrated wave parameters along selected fairways, an indication of crossing waves (*BarentsWatch*, 2016).

Over the last years, the Coastal Highway Route E39 project has initiated several coastal research wave studies based on spectral models (e.g., *Stefanakos et al.*, 2020; *Wang et al.*, 2018). In addition to the spectral representation of waves, *Wang* (2020) showed developments on a large-scale coastal phase-resolved wave model in terms of computational cost, efficiency, and accuracy for the E39 project.

Apart from coastal forecast systems, the need for historical data to estimate extremes (return values) for the coastal wave climate led to the application of statistical downscaling methods. These methods were used to create direction-dependent transfer functions between an open ocean hindcast and high-resolution nearshore simulations during a common training time period (typically a few years). *Brevik et al.* (2009), using a training period of 16 months of WAM/SWAN simulations, found the statistical downscaling of about 50 years of the WINCH hindcast in the Karmøy area, to be very efficient and comparable to measurements.

Compared to 1999, seafarers have nowadays more advanced information on the wave conditions along the Norwegian coast. Nevertheless, the complexity of coastal areas affects the model precision and the lack of coastal wave observations to verify/calibrate the wave prediction systems has been a limitation for further development of the wave modelling. As described by *Cavaleri et al.* (2018), the accuracy of wave predictions is still not sufficient in the coastal and semi-enclosed seas. *Furevik* (2017) found that the current Norwegian wave forecasts show poor performance in several fjords and coastal areas, indicating the need for improvements. These operational forecast models use an old approach for deep-water source terms and the effect of ocean forcing is not included. In addition, the grid of the WAM800 model and its wind forcing have coarse spatial resolutions for narrow fjords. Hence, the aforementioned factors affecting the performance of the current coastal wave forecasts and the need for high-quality wave estimates in the Coastal Highway Route E39 project constituted the study's motivation.

## 1.2 Objectives

Fjords are deep, long, and narrow water channels often associated with strong winds induced by steep mountains and variable surface currents. In typical (shallow) nearshore regions, the deep-water source terms of spectral wave models have a minor impact on wave evolution (*Battjes, 1994; Holthuijsen, 2007*). However, in fjords, deep-water source terms and wave-current interaction may play a key role in wave growth. To our knowledge, there have been no investigations to quantify their effect on the wave growth in fjords.

This study's overall objective is to advance our understanding of wind-generated (gravity) waves in fjords and coastal areas. This is pursued by implementing the third-generation spectral wave model SWAN, in a complex coastal system with narrow fjords and taking advantage of the Coastal Highway Route E39 project's unique measurement campaign to systematically study and quantify the effects of the forcing, the fetch geometry, and the deep-water source terms on the evolution of the wave field. The specific objectives and research questions leading to the three scientific papers are

- How important is the forcing for accurate modelling of wave conditions in a fjord system? What is the effect of local wind and surface currents on coastal and fjord wave climate? (Paper I and III)
- How does the geometry of the fjords affect the wave model accuracy? (Paper II-III)
- How do the different types of the deep-water source term formulations perform in the narrow fjord geometry? (Paper II)
- What is the limitation of pure wave propagation (no wind forcing) to reproduce realistic wave conditions in exposed fjords, and, related to this, how important are the open ocean boundary conditions for fjord wave climate? (Paper I)

# Chapter 2

## Scientific background

### 2.1 Modelling of spectral waves

#### 2.1.1 Variance density spectrum

Looking at the ocean surface, we notice the random and irregular nature of wind-generated waves. Due to this irregularity, a deterministic approach to describe the sea surface is impractical. On the contrary, a stochastic approach is more feasible since average parameters, e.g., wave height, period and direction, change slower in time and space compared to the individual wave characteristics. For a statistically stationary sea state, the sea surface elevation ( $\eta$ ) at any point in time and space can be described as the sum of a large number of harmonic waves (Eq. 2.1), which are independent of each other. The application of the central limit theorem to this description shows that the surface elevation is a Gaussian process.

$$\eta(x, y, t) = \sum_{i=1}^N \sum_{j=1}^M a_{i,j} \cos(2\pi f_i t - k_i x \cos \theta_j - k_i y \sin \theta_j + \Theta_{i,j}) \quad (2.1)$$

Here,  $a_{i,j}$ ,  $\Theta_{i,j}$ ,  $\theta_j$ ,  $k_i$ , and  $f_i$  are random amplitude (Rayleigh distributed), random phase (uniformly distributed between 0 and  $2\pi$ ), direction, wavenumber, and (linear) frequency of each wave component ( $i, j$ ). This model for describing the surface elevation is known as the random-phase/amplitude model (e.g., *Holthuijsen, 2007*).

The variance of the sea surface elevation is given by:

$$\langle \eta^2 \rangle = \int_0^\infty \int_0^{2\pi} E(f, \theta) d\theta df \quad (2.2)$$

where  $E$  is the variance density spectrum ( $\rho_w g E$  is the energy density spectrum, where  $\rho_w$  is the water's density and  $g$  is the acceleration due to gravity). The description of surface waves using the variance density spectrum is called the spectral representation of waves. The integrated wave parameters can be estimated using the  $n$ th-order moment of the density spectrum:

$$m_n = \int_0^\infty f^n E(f) df \quad (2.3)$$

For instance, the significant wave height ( $H_s$  or  $H_{m0}$ ) and the mean wave period ( $T_{m01}$ ) are estimated as  $4\sqrt{m_0}$  and  $m_0/m_1$ , respectively.

## 2.1.2 Kinematics

In the linear wave theory, the propagation velocities of waves in Cartesian coordinates and spectral space are given by the wave train's kinematics (e.g., *Whitham, 1974*):

$$(c_x, c_y) = \left( \frac{d\mathbf{x}}{dt}, \frac{d\mathbf{y}}{dt} \right) = \mathbf{c}_g + \mathbf{u}_c, \quad (2.4)$$

$$c_\sigma = \frac{d\sigma}{dt} = \frac{\partial\sigma}{\partial D} \left( \frac{\partial D}{\partial t} + \mathbf{u}_c \cdot \nabla D \right) - c_g \mathbf{k} \cdot \frac{\partial \mathbf{u}_c}{\partial s}, \quad (2.5)$$

$$c_\theta = \frac{d\theta}{dt} = -\frac{1}{k} \left( \frac{\partial\sigma}{\partial D} \frac{\partial D}{\partial m} + \mathbf{k} \cdot \frac{\partial \mathbf{u}_c}{\partial m} \right). \quad (2.6)$$

Here,  $\sigma$  is the relative circular (or radian) frequency,  $\mathbf{c}_g (= \frac{\partial\sigma}{\partial\mathbf{k}})$  is the group velocity,  $c_x$  and  $c_y$  are the propagation velocities in  $x, y$ -space,  $c_\sigma$  and  $c_\theta$  are the propagation velocities in  $\sigma, \theta$ -space,  $\mathbf{u}_c$  is the ambient current,  $D$  is water depth,  $s$  is the space coordinate in the wave propagation direction ( $\theta$ ) while  $m$  is a coordinate perpendicular to  $s$ . The absolute circular frequency  $\omega (=2\pi f)$  equals the sum of  $\sigma$  and the multiplication of wavenumber and  $\mathbf{u}_c$  (the Doppler shift),

$$\omega = \sigma + \mathbf{k} \cdot \mathbf{u}_c, \quad (2.7)$$

where  $\sigma$  is given by the dispersion relation,

$$\sigma^2 = g|\mathbf{k}| \tanh(|\mathbf{k}|D). \quad (2.8)$$

## 2.1.3 Action balance equation

The phase-averaged information on the sea state is contained in the variance density spectrum  $E$ . The most popular wave models, e.g., WAM, WAVEWATCHIII (*The WAVEWATCH III® Development Group, 2016*) and SWAN, use the action density  $N = E/\sigma$  instead of  $E$  since only the former is conserved during propagation in the presence of ambient current (*Holthuijsen, 2007; Whitham, 1974*). The change of the action density  $N(\sigma, \theta; x, y, t)$  at a grid point is given by the action balance equation:

$$\frac{\partial N}{\partial t} + \nabla \cdot [(\mathbf{c}_g + \mathbf{u}_c)N] + \frac{\partial(c_\sigma N)}{\partial\sigma} + \frac{\partial(c_\theta N)}{\partial\theta} = \frac{S}{\sigma}. \quad (2.9)$$

The left-hand side of the equation contains the kinematic part. The first term denotes the local rate of change of  $N$  in time, and the second term represents the propagation of energy in  $x, y$ -space, including the effect of shoaling. The third and fourth terms indicate the effect of  $\sigma$ -shift and refraction due to variations in surface currents and depth.

The action balance equation's right-hand side consists of the term  $S/\sigma$ ;  $S$  represents the main non-conservative source or sink terms, including the physical processes of generation, dissipation, and redistribution of wave energy at a grid point.

Eq. (2.9) can be re-written in Cartesian coordinates

$$\frac{\partial N}{\partial t} + \frac{\partial(c_x N)}{\partial x} + \frac{\partial(c_y N)}{\partial y} + \frac{\partial(c_\sigma N)}{\partial \sigma} + \frac{\partial(c_\theta N)}{\partial \theta} = \frac{S}{\sigma}, \quad (2.10)$$

or in spherical coordinates (e.g., *SWAN team*, 2017; *The Wamdi Group*, 1988)

$$\frac{\partial N}{\partial t} + \frac{\partial(c_\lambda N)}{\partial \lambda} + \frac{1}{\cos \phi} \frac{\partial(c_\phi N \cos \phi)}{\partial \phi} + \frac{\partial(c_\sigma N)}{\partial \sigma} + \frac{\partial(\tilde{c}_\theta N)}{\partial \theta} = \frac{S}{\sigma}, \quad (2.11)$$

where  $\lambda$  and  $\phi$  are longitude and latitude,  $c_\lambda$  and  $c_\phi$  are propagation velocities in geographic space, and  $\tilde{c}_\theta$  is the propagation velocity  $c_\theta$  in spherical coordinates.

The six main physical processes that contribute to  $S$  are

$$S = S_{\text{in}} + S_{\text{ds}} + S_{\text{nl4}} + S_{\text{nl3}} + S_{\text{fric}} + S_{\text{brk}}, \quad (2.12)$$

where the first three terms are known as the deep-water (typically depth which is equal or greater than half the wavelength) source terms:  $S_{\text{in}}$  is the energy input by wind,  $S_{\text{ds}}$  is the dissipation induced by white-capping, and  $S_{\text{nl4}}$  is the nonlinear wave energy transfer due to quadruplet wave interactions. The last three terms, which have their major contribution in shallow water, consist of the triad nonlinear interaction  $S_{\text{nl3}}$ , the bottom friction  $S_{\text{fric}}$ , and the depth-induced wave breaking  $S_{\text{brk}}$ .

### Wind input

Two processes describe the transfer of energy by the wind to surface waves:

- The resonance mechanism (Phillips, 1957)  
The mechanism describes the generation of waves on the sea surface initially at rest by a random pressure distribution induced by turbulent wind. The pressure field can be expressed as the superposition of harmonic pressure waves propagating in wind direction. When a pressure wave and a free surface wave are in-phase, then the pressure wave transfers energy to the surface wave by resonance. This transfer of energy contributes to wave generation at the initial stages. Assuming a constant wind blowing over the sea surface, the energy transfer is constant over time, leading to a linear wave growth in time.
- The feed-back mechanism (Miles, 1957)  
After the generation of a surface wave by the resonance mechanism, the wave creates a disturbance of the wind profile resulting in minimum air pressure on the lee side of the wave crest and a maximum on the windward side of the wave crest. Thus, when the sea surface moves down (windward side), the wind pushes the surface down, and when the sea surface moves up (lee side), the wind pulls the surface up, following the same motion and transferring wind energy to surface waves. This wave growth is exponential in time since the wave grows faster as it becomes larger.

According to these two mechanisms, the total wave growth by wind can be expressed as the sum of linear ( $A$ ) and exponential ( $BE$ ) term:

$$S_{\text{in}}(\sigma, \theta) = A + BE(\sigma, \theta). \quad (2.13)$$

The linear term  $A$  is given by *Cavaleri and Rizzoli* (1981), while several expressions can be found for  $B$  (e.g., *Plant*, 1982; *Snyder et al.*, 1981; *Yan*, 1987) in spectral models. The  $S_{\text{in}}$  term depends mainly on wind direction, friction velocity ( $u_*$ ), and wave characteristics (i.e., frequency, direction and phase velocity). The estimation of  $u_*$  is based on a wind drag formula (e.g., *Fan et al.*, 2012; *Guenther et al.*, 1992; *Rogers et al.*, 2012; *Zijlema et al.*, 2012) that uses as input the wind speed at 10 m above the sea level ( $U_{10}$ ). The effect of surface currents on  $S_{\text{in}}$  is considered using the relative wind ( $\mathbf{U}_r = \mathbf{U}_{10} - \mathbf{u}_c$ ).

The linear term  $A$  found to have a minor effect on  $S_{\text{in}}$  in this study (not shown), and it is thus neglected. The reader can refer to Paper II (Chapter 5) for more details about the different formulations of  $B$ .

### White-capping

The term white-capping (or white horses) is used to describe the wave breaking in deep water. The dissipation by white-capping in wave models has a general form of

$$S_{\text{ds}}(\sigma, \theta) = -\Psi E(\sigma, \theta), \quad (2.14)$$

where  $\Psi$  describes the statistical properties of white-capping. Some of the main models/approaches for estimation of  $\Psi$  in spectral models are:

- The pressure pulse model of *Hasselmann* (1974)  
The white-cap creates a pressure pulse on the lee-wind side of the breaking crest, acting against the rise of sea surface and sinking wave energy. In this wave dissipation process, the white-caps transport energy from the waves to turbulence and surface currents. This method is also known as the Komen approach since *Komen et al.* (1984) formulated it in a numerical wave model. In this approach,  $\Psi$  is a function of mean wave parameters, i.e., the mean steepness ( $\tilde{S}$ ) and mean wavenumber ( $\tilde{k}$ ). However, these dependencies are proved to be problematic in mixed wind sea and swell conditions (see *van der Westhuysen et al.*, 2007, and references therein).
- The saturation-based method  
The saturation-based method is an alternative to the Komen approach, expressed by *Alves and Banner* (2003), and further developed in the spectral wave models by *van der Westhuysen et al.* (2007). The method expresses white-capping without the  $\tilde{S}$  and  $\tilde{k}$  dependencies using instead the spectral saturation, which is positively correlated to the breaking probability. The wave breaking starts when the spectral saturation at that frequency exceeds a threshold. Extensions are made by *Arduin et al.* (2010), who added a direction-dependent spectral saturation, a cumulative term (smoothing of the surface by large wave breakers) and a dissipation term ( $S_{\text{turb}}$ ) due to wave turbulence interactions.

- The observation-based model, known as ST6, (*Babanin et al., 2010*)  
The white-capping in ST6 is an observation-based formulation consisting of an inherent and cumulative dissipation term. Contrary to the saturation-based method, the waves start breaking when the spectral density at a specific frequency exceeds a spectral density's limit based on the spectral saturation. In addition to white-capping, ST6 contains formulations for wind input and non-breaking dissipation.

The reader can refer to Paper II (Chapter 5) for more details about the different formulations of  $\Psi$ .

### Nonlinear wave-wave interactions

The nonlinear wave-wave interactions are important processes that affect wave growth. They re-distribute energy among the wave components by resonance. The nonlinear wave-wave interactions can be categorized in:

- Quadruplets  
The quadruplet wave-wave interactions exchange energy between two pairs of wave components that fulfil the resonance conditions. If the conditions are met (the frequency, wavenumber, and direction of the two pairs match), the energy is distributed among the four-wave components (quadruplet). The resonance conditions can be expressed mathematically,

$$\begin{cases} \mathbf{k}_1 + \mathbf{k}_2 = \mathbf{k}_3 + \mathbf{k}_4 \\ \sigma_1 + \sigma_2 = \sigma_3 + \sigma_4 \end{cases}, \quad (2.15)$$

The mechanism is responsible for transferring energy from the spectral peak (i) to lower frequencies shifting the peak frequency to lower values and (ii) to higher frequencies for which the mechanism of white-capping dissipates the energy. Since a full computation of the quadruplet is not feasible for practical applications due to high computational cost, it is estimated using the Discrete Interaction Approximation (DIA) (*Hasselmann and Hasselmann, 1985; Hasselmann et al., 1985*) in this study, with the following configurations in frequencies:

$$\begin{cases} \sigma_2 = \sigma_1 \\ \sigma_3 = \sigma_1(1 + \lambda) \\ \sigma_4 = \sigma_1(1 - \lambda) \end{cases}, \quad (2.16)$$

where  $\lambda$  is equal to 0.25 (default).

- Triads  
The triad wave-wave interactions transfer energy from lower to higher frequencies in very shallow water. The triads resonance conditions are met if the sums of wavenumber vectors and frequencies of two wave components are equal to the wavenumber vector and frequency of a third wave component. These resonance conditions cannot be fulfilled in deep water since the dispersion relation (linear

theory) does not permit this wave components' combination (e.g., *Holthuijsen, 2007*). Sensitivity analysis showed that these interactions have a minor effect on fjord wave applications (not shown), and they thus were neglected in this study.

### Bottom friction

The bottom friction model in this study is according to the JONSWAP empirical model (*Hasselmann et al., 1973*) expressed in (e.g., *SWAN team, 2017*):

$$S_{\text{fric}}(\sigma, \theta) = -C_b \frac{\sigma^2}{g^2 \sinh^2 kD} E(\sigma, \theta), \quad (2.17)$$

where  $C_b$  is a bottom friction coefficient set to  $0.067 \text{ m}^2 \text{ s}^{-3}$  in the SWAN simulations, as suggested for depth-limited wind sea conditions by *Bouws and Komen (1983)*.

### Depth-induced wave breaking

The energy dissipation due to the depth-induced wave breaking in this study is parameterized according to *Eldeberky and Battjes (1996)*, which is based on the bore model of *Battjes and Janssen (1978)*, in SWAN (e.g., *SWAN team, 2017*):

$$S_{\text{brk}}(\sigma, \theta) = \frac{D_a}{\int_0^{2\pi} \int_0^\infty E(\sigma, \theta) d\sigma d\theta} E(\sigma, \theta) = -\alpha_{\text{BJ}} \frac{Q_b \bar{\sigma}}{\beta^2 \pi} E(\sigma, \theta). \quad (2.18)$$

Here  $D_a (< 0)$  is the average rate of energy dissipated during the breaking process per unit area,  $\beta = H_{\text{rms}}/H_{\text{max}}$ ,  $H_{\text{rms}}$  is the root-mean-square wave height,  $H_{\text{max}} = \gamma D$  is the maximum possible wave height in depth  $D$ ,  $\gamma$  is the breaking coefficient,  $\bar{\sigma}$  is the mean relative circular frequency, and  $Q_b$  is the fraction of depth-induced breakers depending critically on  $\beta$ . In this study, we used the default values for  $\gamma = 0.73$  and  $\alpha_{\text{BJ}} = 1$ .

### Generations of spectral wave models

There are three generations of spectral models with the main differences:

- The first-generation models, e.g., *Gelci et al. (1956)*, *Pierson (1966)*, *Cavaleri and Rizzoli (1981)*, use a parameterized wind input, enforcing a high-frequency tail to feature the white-capping and the quadruplet effects.
- The second-generation models, e.g., *Barnett (1968)*, *Yamaguchi et al. (1988)*, *Zakharov and Pushkarev (1999)*, are similar to the first-generation, but with the quadruplet effects being estimated via parametric formulas, e.g., JONSWAP spectrum.
- The third-generation models, e.g., WAM (*The Wamdi Group, 1988*), SWAN (*Booij et al., 1999*), and WAVEWATCHIII (*The WAVEWATCH III® Development Group, 2016*), are currently the most advanced wave prediction (spectral) models, which estimate the quadruplet explicitly, e.g., through DIA, allowing thus the spectrum to develop without any theoretical shape restriction.

## 2.2 Wave conditions in fjords and coastal areas

### 2.2.1 The wave climate on the west coast of Norway

The wave climate in the west part of Norway is characterized by mixed swell–wind sea conditions. Fig. 2.1 illustrates regions dominated by swell (green) or wind sea (blue) along the Norwegian coast, based on a wave energy flux’s analysis by *Christakos et al.* (2020). Swell waves reaching the coastline are mostly generated by cyclones in the North Atlantic Ocean. The highest swell energy reaching the coast is detected in the Norwegian Sea due to its exposure to ocean waves originating from the North Atlantic (e.g., *Christakos et al.*, 2020; *Semedo et al.*, 2014). Swell is weaker in the Norwegian coastal areas located in (i) the North Sea due to sheltering by the British Isles and (ii) in the Barents Sea due to propagation over a longer distance (swell decay). In coastal areas located in the Norwegian Sea, the wind sea has a dominant southwest direction parallel to the coastline following the dominant wind pattern. However, the wind sea is often characterized by high temporal and spatial variations due to the frequent passages of extra-tropical cyclones and coastal wind phenomena (*Barstad and Grønås*, 2005, 2006; *Christakos*, 2013; *Christakos et al.*, 2014, 2016; *Jonassen*, 2012).

The wave climate in fjords differs from the typical coastal climate since (i) the wave direction is steered by the fjord axis, (ii) the propagation of swell depends on the exposure to open sea, and (iii) the local wind sea growth depends on the local wind which is steered by the topography and fjord geometry. The fjord locations can be categorized into:

- Exposed to open sea (or outer) locations: where the offshore waves (e.g., swell or old wind sea) dominate the wave climate, but the local wind sea can be comparable depending on the fjord geometry, the exposure to open sea (partly exposed locations) and the weather conditions, e.g., strong wind channelling.
- Sheltered (or inner) locations: where the local wind sea dominates the wave climate and swell is nearly absent.

### 2.2.2 Area of investigation

In this thesis, the study area is a complex coastal system with narrow fjords, partly exposed to the Norwegian Sea, at the west coast of Norway (red rectangle in Fig. 2.1). According to *Christakos et al.* (2020), this region has some of the most energetic offshore wave climate along the Norwegian coast. Moreover, with its dense grid of met-ocean observations (section 2.2.4), this fjord system is a natural laboratory for coastal and fjord wave studies. Simulations of wind-generated wave simulations are performed using the third-generation spectral model SWAN.

### 2.2.3 Modelling system

#### Dynamical downscaling & boundary conditions

The intrusion of both wind sea and swell from the open sea to the nearshore areas requires full two-dimensional (2D) spectra as offshore boundary conditions to the coastal

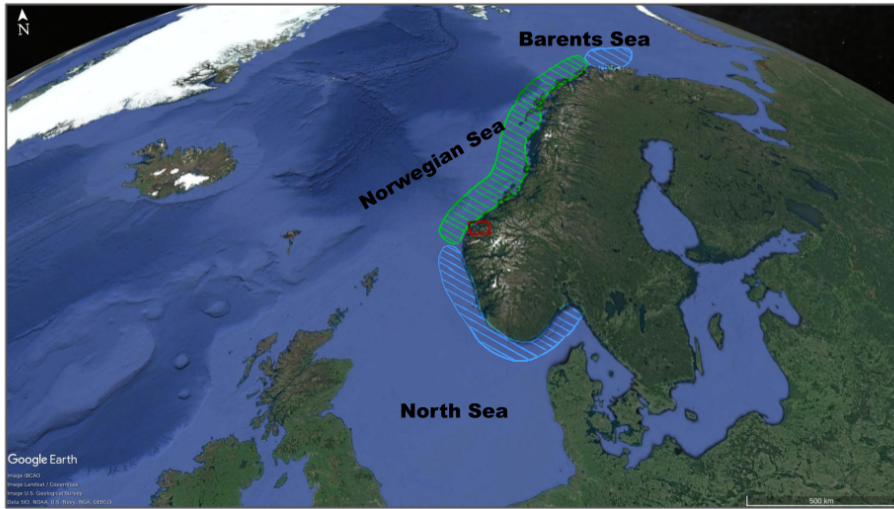


Figure 2.1: Conceptual illustration of areas with the dominant swell (green) and wind sea (blue) along the coast of Norway, based on the analysis of the climatology of the wave energy flux by Christakos *et al.* (2020). The red rectangle indicates the location of the fjord system studied in Papers I-III (Chapter 5).

wave model. As discussed by Breivik *et al.* (2009), this type of nested setup with full 2D wave spectral information on the offshore boundaries is known as dynamical down-scaling. In this way, the nested model can resolve fine-scale phenomena because of its high-resolution bathymetry and wind field, which is not possible by a coarse grid of open ocean wave model e.g., WAM.

The offshore boundary conditions for SWAN simulations in Papers I-III (Chapter 5) were provided by the NORA10 hindcast 2D spectra with 3-hourly temporal resolution. The spectral nesting and interpolation of offshore boundaries were according to Breivik *et al.* (2009). The wave component of NORA10 hindcast is a  $10 \text{ km} \times 10 \text{ km}$  WAM model forced by HIRLAM (Undén *et al.*, 2002) winds nested inside a  $50 \text{ km} \times 50 \text{ km}$  WAM model forced by ERA-40 (Uppala *et al.*, 2005) winds, as described by Reistad *et al.* (2011). The NORA10 grid covers a significant part of the North Atlantic, allowing a realistic propagation of long waves (swell) to the Norwegian coast. Information regarding the NORA10 hindcast is also provided in Papers I-III (Chapter 5). To achieve high spatial resolution nearshore and resolve coastal and fjord features, we used two (one-way) nested domains in SWAN with horizontal resolutions of  $1 \text{ km}$  (D1: outer) and  $250 \text{ m}$  (D2: inner), as presented in Fig. 2.2. The computation on the D1 grid used wave boundary conditions from NORA10, while the finer D2 grid used boundary conditions from D1. The SWAN model was running in a non-stationary mode with spherical coordinates and a time step of  $10 \text{ min}$  with 4 iterations of the implicit scheme (sensitivity analyses with smaller time steps showed minor differences). Finally, 36 directions and 32 discrete frequencies from  $0.04 \text{ Hz}$  to  $1 \text{ Hz}$  (logarithmically spaced) were used. Experiments with a higher number of directions (72) illustrated no significant differences in wave height estimates (not shown).

### Atmospheric forcing

In Papers I-III (Chapter 5), SWAN was forced with atmospheric forcing by WRF0.5, a downscale product of the reanalysis ERA-Interim (Dee *et al.*, 2011) based on the Advanced Research WRF-ARW (Skamarock *et al.*, 2008) state-of-the-art numerical weather prediction model version 3.5.0. The WRF0.5 wind fields have a spatial resolution of 0.5 km and 1-hourly temporal resolution. In Paper I, in addition to WRF0.5, wind fields with coarser spatial resolutions, such as ERA5 (Hersbach *et al.*, 2020), NORA10 (Reistad *et al.*, 2011), and AROME2.5 (Müller *et al.*, 2017), were used to force the SWAN model. More details about the different wind forcing are provided in Paper I (Data and methods).

### Ocean forcing

In Paper III (Chapter 5), we forced the SWAN model with surface currents by Norkyst800 (Albretsen *et al.*, 2011). Norkyst800 is a high spatial resolution (800 m) operational coastal ocean modelling system covering the entire Norwegian coast and predicts ocean currents, salinity, temperature, and water level with a 1-hour temporal resolution. It is based on the numerical model ROMS (Regional Ocean Modeling System; <http://myroms.org>). Norkyst800 was developed by the Institute of Marine Research in collaboration with the MET Norway and the Norwegian Institute for Water Research. The forcing fields contain wind and freshwater (river) discharge which are essential for nearshore applications. The model output is available via the Thredds Service at MET Norway.

### Bathymetry

The bathymetry (bottom topography) data was derived by *EMODnet Bathymetry Consortium* (2018). It has a spatial resolution of approximately  $115 \times 115$  meter which is considered suitable for coastal and fjord applications. The bathymetry of the studied area is illustrated in Fig. 2.2.

## 2.2.4 Met-ocean observations

An extensive met-ocean measurement program is carried out by Fugro Oceanor AS on behalf of the Norwegian Public Roads Administration in connection with the Coastal Highway E39 project. This study has used wind, wave and surface current measurements from five Wavescan buoys located in Breisundet/Sulafjorden and Vartdalsfjorden in the fjord system (Fig. 2.2). The buoys D, A and B were deployed in October 2016 (Fig. 2.3), while C in April 2017 and F in November 2017 (Table 2.1). The depth exceeds 200 m at all measurement locations. The measurements include both integrated wave parameters and raw data (heave, pitch, roll), as well as wind and currents (Furevik *et al.*, 2020). The wind sensors are mounted 4.1 m above the sea level, and acoustic measurements of surface current are obtained at 1 m below the sea surface. Quality control of met-ocean observations was performed to assure reliable data in this study. For wind forcing evaluation, the observed and modelled wind speeds are adjusted on the same level height using the logarithmic wind profile (more details in Paper I). To estimate the frequency wave spectrum from the observed surface elevation (heave), the

Buoy (location)	longitude,latitude [WGS84]	Depth[m]	Period
D (Breisundet)	5.93, 62.44	345	10.2016 - ongoing
A (Sulafjorden)	6.05, 62.43	375	10.2016 - ongoing
B (Sulafjorden)	6.08, 62.40	325	10.2016 - ongoing
C (Sulafjorden)	6.05, 62.39	450	04.2017 - ongoing
F (Vartdalsfjorden)	5.90, 62.22	217	11.2017 - ongoing

Table 2.1: Location, depth, and measurement period for wave buoys D, A, B, C and F.

python function `Heave_to_WelchSpec1D` is used (Christakos, 2021). The function, which is based on the SciPy library (Virtanen *et al.*, 2020), applies Welch’s method (Welch, 1967), with a Hanning window in the Fourier transform after detrending.

In theory, a buoy is limited to measure waves with wavelengths ( $\lambda$ ) longer than its diameter  $d_{\text{buoy}}$  (Stewart, 2008). Nevertheless, even if  $\lambda$  is greater than  $d_{\text{buoy}}$ , the buoy’s size still affects the waves (wave–structure interaction). Performing a quality check, we found that a good quality of wave data is achieved for  $\lambda$  larger than 1.5 to 2 times  $d_{\text{buoy}}$  (not shown). Hence, for the wave buoys used in this project ( $d_{\text{buoy}}=2.8$  m), the maximum observed frequency ( $f_{\text{max}}$ ) is ca. 0.5-0.6 Hz (Fig. 2.4), which is lower than the Nyquist frequency (1Hz, i.e., half of the buoy’s sampling frequency). This is usually not a limitation in exposed locations where the frequency of dominant waves (e.g., swell/old wind sea) is much lower than this limit. However, in some cases, it may be problematic in sheltered areas (e.g., Vartdalsfjorden), where the frequency of dominant waves (young wind sea) is close to  $f_{\text{max}}$  limiting detailed investigations on the high-frequency tail.

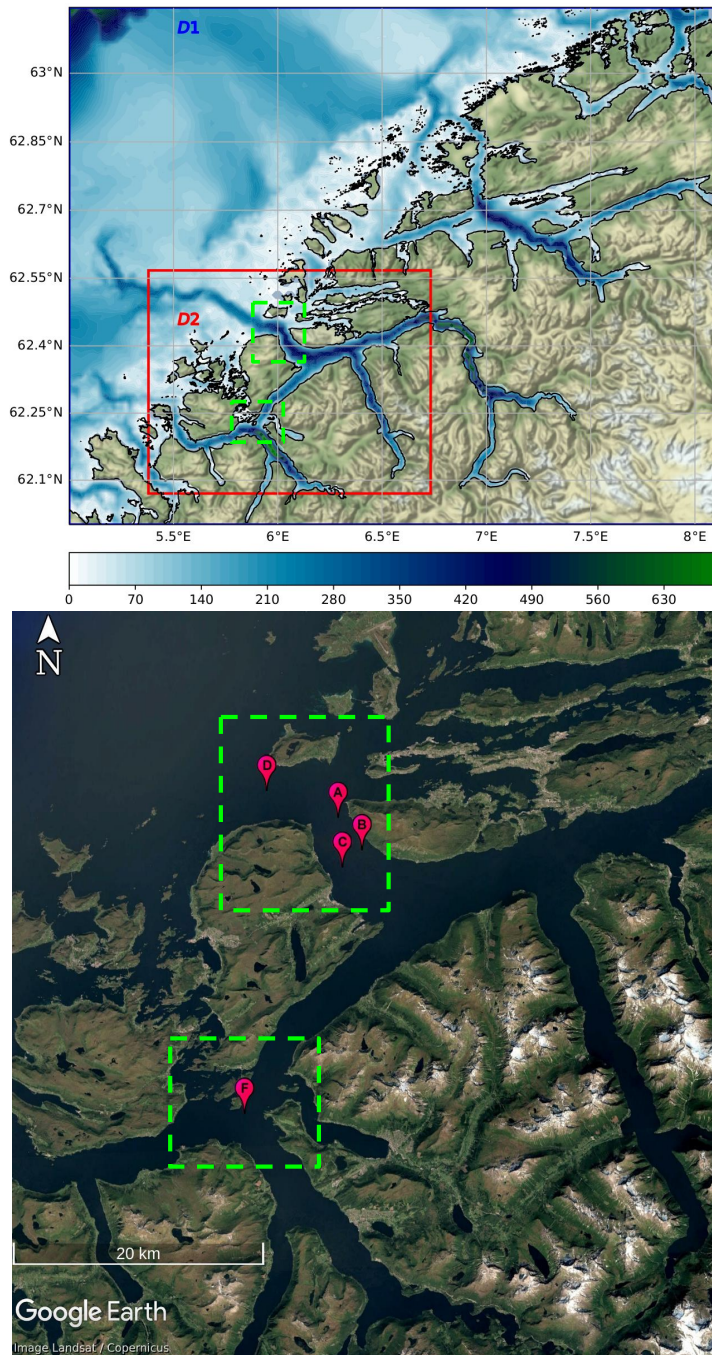
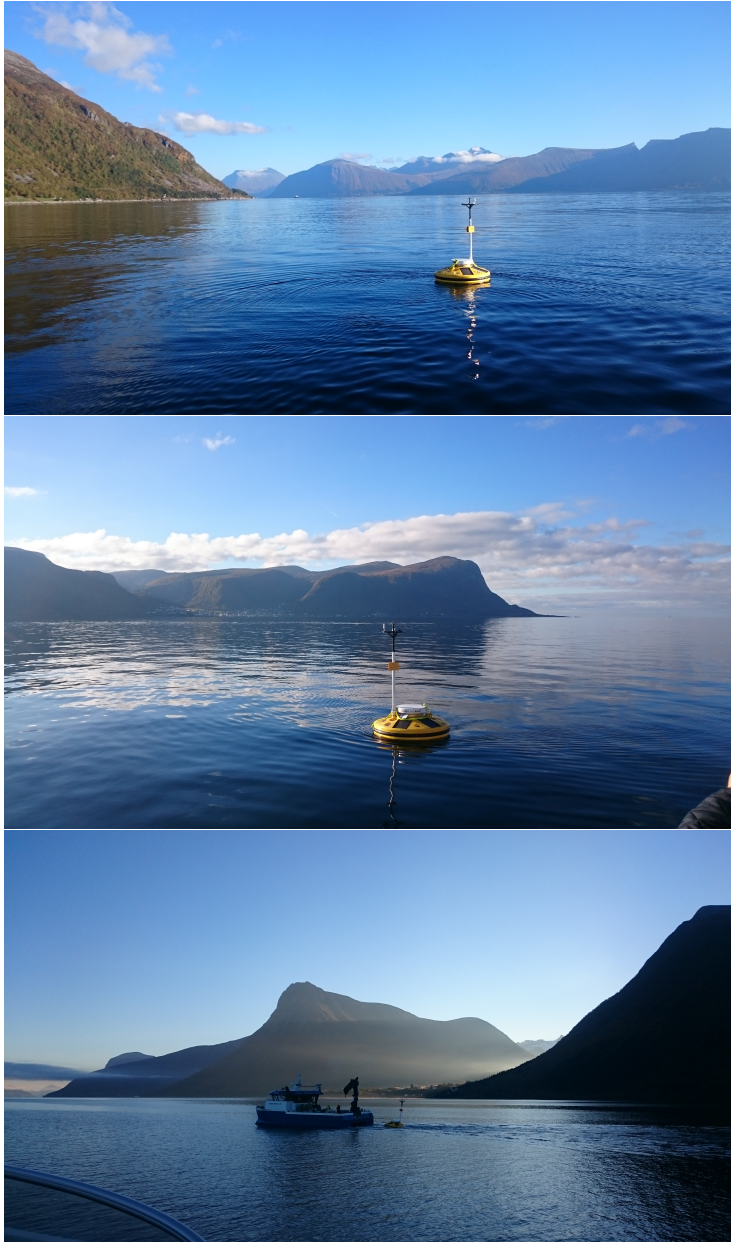


Figure 2.2: Top: outer (D1) and inner (D2, red rectangle) model domains (with depth in meters) for the wave simulations. The green rectangles indicate the measurement areas (north: Breisundet/Sula fjorden, south: Vartdalsfjorden). Bottom: location of buoys in the measurement areas.



*Figure 2.3: Deployment of wave buoys in Sulafjorden, October 2016 (photo credit: B.R. Furevik).*

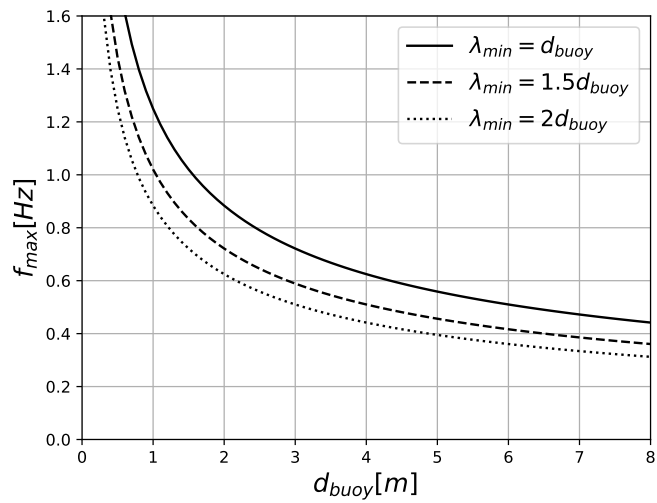


Figure 2.4: Maximum observed frequency ( $f_{\max}$ ) as a function of buoy diameter ( $d_{\text{buoy}}$ ) for different minimum thresholds of wavelength ( $\lambda_{\min}$ ) in deep water.



## **Chapter 3**

### **Summary of the papers**

### **Paper I: The importance of wind forcing in fjord wave modelling**

*Christakos, K., B.R. Furevik, O.J. Aarnes, Ø. Breivik, L. Tuomi, and Ø. Byrkjedal (2020), Ocean Dynamics, 70, 57–75.*

Paper I investigates the role of wind forcing on surface wave conditions in a partly exposed fjord system at the west coast of Norway. In this study, we implement the spectral model SWAN using surface wind fields from four different atmospheric models, including the ERA5 reanalysis (31 km grid spacing), NORA10 hindcast archive (10 km grid spacing), AROME2.5 operational model (2.5 km grid spacing), and WRF0.5 (0.5 km grid spacing). The offshore boundary conditions are provided by the NORA10's wave component. Simulation with no wind forcing is performed to quantify the importance of the open ocean boundary conditions and the local wind in the fjord system. In addition to long-term statistics, two case studies of wave simulations with onshore and offshore winds are investigated. Both wind and wave estimates are compared with in situ observations from five fjord locations.

#### Key findings:

- The high-resolution wind forcing is necessary to obtain a realistic wind field in complex fjord topography.
- The best model performance in terms of wave height is found at the exposed (to open sea) locations using high-resolution wind fields.
- The spatial resolution of wind forcing has a pronounced impact on wave estimates at inner fjord locations.
- Local phenomena such as wind channelling and lee effects significantly affect the wave predictions.
- During normal (average) conditions, simulation with pure wave propagation (no wind forcing) shows reasonable results at the exposed locations.
- During extreme cases, simulation with pure wave propagation cannot predict the wave heights accurately in any of the fjord locations.
- A problematic behaviour of wave simulations at the inner location was observed, despite the relatively good wind estimations provided by the high-resolution atmospheric model.

We hypothesize that this problematic behaviour is related to the effect of the narrow fjord geometry on the deep-water source term formulations, which is therefore investigated in Paper II.

---

## **Paper II: Modelling wave growth in narrow fetch geometries: The white-capping and wind input formulations**

*Christakos, K., J.V. Björkqvist, L. Tuomi, B.R. Furevik, and Ø. Breivik (2021), Ocean Modelling, 157, 101730.*

We investigate the performance of three different spectral model deep-water source term formulations in narrow fetch geometries of the fjords. The formulations are used to model the sea surface waves in a complex nearshore area with narrow fjords located on Norway's west coast. The simulation system is based on the SWAN spectral wave model, which is forced with high-resolution winds from WRF0.5 and two-dimensional wave spectra from NORA10 at the offshore boundaries. The model performances of the new ST6 and two older SWAN wind input and white-capping formulations are evaluated using observed spectra and wave parameters from five buoy locations. Both long-term statistics and two case studies of narrow fetch geometries without swell and with swell–wind sea conditions are used.

### Key findings:

- The fetch geometry has a distinct effect on model simulations' accuracy at inner fjord locations.
- The dependence between fetch geometry and the model accuracy is weak in exposed areas.
- The saturation-based white-capping approach (WESTH) performs most accurately in fjords with mixed swell–wind sea conditions.
- In narrow fetch geometry without swell, all packages overestimate the wave energy, of which ST6 shows the highest sensitivity to fetch geometry and local wind variations.
- At the inner parts of fjords where there is no swell, the Komen approach shows the best performance.
- At inner locations and during strong wind conditions, the results illustrate that the white-capping in ST6 is relatively weak compared to its strong wind input.
- The wind drag formulations that take into consideration the wave effect using iterative methods, provide more precise results than the default formulation in ST6.

At inner locations, applying different source term formulations shows improvements regarding the wave height estimations. However, none of these formulations significantly improves the problematic behaviour in such areas. Several factors can cause this behaviour that can be grouped into (i) direct factors that are linked to the source term formulations and (ii) indirect factors that are related to other effects such as wind-drag formulations, non-linear interactions, and forcing fields. We hypothesize that the effect of surface currents on waves could be an important factor in model accuracy in narrow fjords. Hence, we investigate this argument in the following paper.

**Paper III: The impact of surface currents on the wave climate in narrow fjords**

*Christakos, K., J.V. Björkqvist, Ø. Breivik, L. Tuomi, B.R. Furevik, and J. Albretsen, Ocean Modelling, under review.*

Paper III investigates the effect of the surface currents on surface gravity waves in a complex fjord system partly exposed to the Norwegian Sea. The simulations are based on the SWAN wave model forced with wave spectra from NORA10 at the offshore boundaries, winds from the high-resolution atmospheric model (WRF0.5), and surface currents from the operational 3D ocean model (Norkyst800). Wave simulations with and without ocean forcing are evaluated by comparing integrated wave parameters and modelled spectra to observations from five wave buoys. The comparison covers three winter seasons (2017–2020).

**Key findings:**

- Spectral moments and shape of the average spectra are estimated more accurately at most locations when current forcing is applied.
- Wind sea is simulated more accurately in terms of wave energy when current forcing is included.
- The incorporation of surface currents on wave simulations improves the wave height estimations by more than 10 percentage points at the inner fjord location.
- The impact of surface currents on wave characteristics, such as wave height, spectral bandwidth, directional spreading, and relative peak frequency, is more pronounced at inner locations.

The results indicate that the improvement in model performance (accuracy) is worth the added complexity of using the offline coupled model system for producing operational fjord wave simulations. However, the model performance at inner fjord locations is less accurate compared to outer areas. We expect that other factors, such as the quality of forcing fields, the model physics, and the fjord geometry, can affect the accuracy of wave simulations (see Chapter 4).

---

### Concluding remarks

Papers I-III quantify the role of the different factors affecting the model performance in a complex fjord system, partly exposed to open sea. Apart from the fine grid of the wave model and the high quality of the bathymetry that are essential in all types of fjords, the results of this thesis lead to the following overall conclusions:

- In exposed (outer) locations—as expected—the quality of the boundary wave conditions appears as the most important factor. Given that the most energetic waves come from the boundaries, any potential inaccuracies in these waves will transfer to the coastal and fjord wave estimates. The quality of the wind forcing fields has a secondary role, while becomes crucial during extreme conditions. After the wind forcing, the inclusion of ocean forcing and the accuracy of the deep-water source term packages affect the quality of wave simulations.
- In sheltered (inner) locations, the quality of wind forcing is the most important factor, closely connected to its spatial resolution. Because fjords are long and narrow inlets of water surrounded by steep mountains, the grid size of the atmospheric model needs to be smaller than the fjord width, often less than 2–3 km, to be able to reproduce the orographic features. Especially during extreme wind events within the fjords, the fine grid is essential to capture local wind phenomena such as wind channelling induced by the orography. Following the wind forcing, the ocean forcing and the choice of the deep-water source term packages have an important role in the quality of wave simulations. The incorporation of surface current on wave simulations improves considerably the wave estimates. Significant differences are also observed between the packages where ST6 shows the worst model results, overestimating the observed wave energy.



# Chapter 4

## Perspectives and outlook

This dissertation has provided insight into spectral wave modelling in deep-water fjords and coastal areas, advancing our knowledge on wind-generated waves. More specifically, it has enhanced our understanding of the role of forcing, fetch geometry, deep-water source terms, and open ocean boundary conditions in coastal and fjord wave modelling. The results also point towards several open research questions and possibilities for future studies. Some of the most pressing ones will be presented and discussed in this chapter.

### Choice of grid

The wave simulations in Papers I-III were based on a nested model setup with a regular grid and a dynamical downscaling technique. An alternative is the use of an unstructured grid (e.g., *Abdolali et al.*, 2020; *Lin et al.*, 2019; *Mao et al.*, 2016; *Smith et al.*, 2018, 2020; *Zijlema*, 2010) or a spherical multiple-cell (SMC) grid (*Li*, 2011, 2012; *Li and Saulter*, 2014). In general, the unstructured grid is appropriate in nearshore regions where the bathymetry varies significantly, providing the finest resolution in areas in which it is most essential (*SWAN team*, 2017). However, in the case of fjords (typically characterized by large water depth), using an ordinary unstructured grid is not recommended. The grid becomes very dense (computationally demanding) in sheltered and very narrow regions, e.g., at the very inner part of a fjord, where the waves are very small. Thus, our choice (nested model with a high resolution inner regular grid) is considered more appropriate and efficient for the fjord system's complexity. An alternative could be achieved by creating a "flexible" unstructured grid based on specific characteristics of fjord waves, e.g., applying a finer grid in shallow shelf regions, fjord cross-sections, fjord inlets, or in regions where energetic waves are expected. This approach could be applied in our future fjord studies.

### Wind forcing

Paper I presented the important role of wind forcing in fjord wave modelling. Nevertheless, our assessment of the quality of the different wind fields was based on a limited number of point measurements within the fjord system. Therefore, even though the high-resolution winds (WRF0.5) showed good performance overall, the evaluation was restricted to specific locations and did not allow us to generalize our conclusions for the whole fjord system. The accuracy of wind forcing along the fjord axis plays a vital role in gaining representative model results. More advanced measurement techniques such

as wind lidars can measure the wind field horizontally, along a fjord axis, allowing a more precise evaluation of the modelled wind field. Such wind observations could also potentially be used as forcing for a spectral wave model, creating a high-quality wave hindcast/nowcast.

### Deep-water source terms

The results in Paper II indicated the role of deep-water source term formulations in fjord applications. These formulations might need some modifications (including more physical processes/mechanisms) to improve the model performance in fjords and coastal areas. For instance, none of the applied source term packages considers the straining mechanism, i.e., the long waves' effect on the steepness of the shorter waves. This mechanism can be important in the exposed fjord locations where long waves (swell) coexist with shorter waves (local wind sea). It is possible to account for this mechanism by adding an additional dissipation term based on the Cumulative Steepness Method (*Hurdle and van Vledder, 2004; van Vledder and Hurdle, 2002*). Furthermore, the applied source terms did not use a direction-dependent white-capping dissipation. According to *Ardhuin et al. (2010)*, a direction-dependent saturation in white-capping can provide more accurate wave estimates. As illustrated by *Pettersson (2004)*, a narrow fetch geometry affects the directional distribution of the dominant waves. Hence, performing sensitivity studies using ST4 package (*Ardhuin et al., 2010*) with different values of  $\delta_d$  parameter ( $\delta_d = 1$  for isotropic saturation,  $\delta_d \neq 1$  for an-isotropic saturation) may provide a better understanding of the directional fetch-limited growth in narrow fjords. In this study, the DIA parameterization for four-wave nonlinear interactions  $S_{nl4}$  was used in all the wave simulations. It is widely known that the DIA tends to broaden the wave spectrum (e.g., *Rogers and Wang, 2007; Tamura et al., 2008*). According to *Liu et al. (2019)*, ST6 with DIA shows higher sensitivity to fetch geometry than using alternatives, such as the Generalized Multiple DIA (*Tolman, 2008*) and the Webb-Resio-Tracy (WRT) method (*Tracy and Resio, 1982; Webb, 1978*), which computes the full nonlinear Boltzmann interactions. *Ponce de León and Osborne (2020)* recommend the use of the full Boltzmann interactions to obtain a more realistic spectral shape. Hence, additional studies using the full nonlinear Boltzmann interactions need to be performed to investigate the effect of  $S_{nl4}$ -formulation on the shape of wave spectrum in fjords.

### Shallow-water source terms

During storms or strong swell propagation to the coast, shallow-water dissipation processes such as bottom friction and depth-induced wave breaking occur in shallow/transitional areas adjacent to the fjord system. Detailed investigation of these processes was not included in the present study since no observations were available in these areas. However, the effect of bottom friction on long waves off the fjord system might be equally important to the deep-water source terms in some areas. Moreover, wave damping due to vegetation can influence wave growth in nearshore regions. In this manner, sensitivity studies based on the shallow-water source terms combined with observations need to be performed to advance our knowledge on these processes and their impact on the fjord waves.

### **Ocean forcing**

The importance of the surface currents on fjord waves was highlighted in Paper III. The results showed that the current forcing is essential for accurate wave estimates at inner fjord locations. Nonetheless, there are still open questions, such as if a finer grid of the ocean forcing would improve the wave model performance. The spatial resolution of applied ocean forcing (Norkyst800) is considered reliable for coastal applications, and the model topography can capture the main current features providing good estimates of the current field in upper layers of fjords (*Asplin et al.*, 2020). However, using a higher resolution could improve topographically induced currents in narrow fjords and provide more accurate ocean forcing for wave model integrations.

### **Effect of rain and freshwater discharge**

Rain and freshwater discharges (river runoff) induce changes in stratification. In fjords, the wind-driven current is strongly affected by both the fetch geometry and the stratification. Considering that the fjords are associated with strong stratification (see Introduction in Paper III), the larger part of the wind energy is used to accelerate the surface water and less for mixing (e.g., *Fergestad et al.*, 2019). Besides, the rain affects the generation and dissipation processes of surface waves (*Cavaleri et al.*, 2015; *Laxague and Zappa*, 2020). *Katsafados et al.* (2018) showed that the consideration of rain's impact on ocean waves improves the wave height estimates during a hurricane. Hence, to quantify the overall impact of rain on wave growth in narrow fjords, wave model integrations including these effects need to be carried out.

### **Fully coupled system**

The results in Paper III suggested the use of current forcing in operational coastal wave forecasts. In addition, the use of a fully coupled atmosphere-wave-ocean system (e.g., *Varlas et al.*, 2020) might be desirable to investigate air-sea and wave-current interactions in fjords and coastal areas. A fully coupled system could provide a better representation of the key processes by using more accurate input fields, e.g., (i) use of the wave-induced momentum stress to force the ocean model, instead of a parameterization of wind, and (ii) use of the friction velocity ( $u_*$ ) from the atmospheric model, contrary to the traditionally used wind speed at 10 m height.

### **Need for advanced wave observations**

Observations are vital in wave modelling. Observations have been used for validation, calibration of wave models but also in the new development of model physics, e.g., ST6. In the present study, data from five waves buoys were available. These measurements were essential to provide an assessment of the model performance in the fjord system. However, the use of in situ measurements restricted the investigation in specific areas. In addition, their relative low  $f_{max}$  (see Chapter 2.2.4) limited the investigation of the high frequency spectral tail. More advanced wave measurements such as a stereo camera (*Benetazzo et al.*, 2012, 2016; *Bergamasco et al.*, 2017; *Fedele et al.*, 2013; *Guimarães et al.*, 2020; *Vieira et al.*, 2020) or marine radars (*Dankert and Rosenthal*, 2004; *Huang et al.*, 2017; *Nieto Borge et al.*, 1999, 2006, 2008; *Young et al.*, 1985) have been used to investigate wave dynamics. This type of measurement techniques can observe 3D waves providing important spatio-temporal wave statistics. For

instance, information about the wave spectrum before and after a breaking event can be used to estimate important parameters such as breaking severity (*Babanin, 2011*), and may lead to further developments in source term formulations.

### **Applicability of results to other fjord systems**

This thesis focused on a coastal and fjord system at the west coast of Norway in the Norwegian Sea. Although the geographic and climatic characteristics of the studied fjord system (e.g., exposed outer locations to strong swell and sheltered inner locations with young wind sea) are typical for most of the fjords around the world (e.g., Norway, Iceland, the Faroe Islands, Chile, Greenland, Alaska, New Zealand), we need to expand the simulations to other areas with different fjord characteristics (width, length, offshore and local climate). As shown by *Christakos et al. (2020)*, the offshore wave climate differs along the Norwegian coast. For instance, the wind sea contributes the most to the total wave energy flux in areas in the North Sea and the Barents Sea, whereas in the Norwegian Sea swell dominates the coastal wave climate. Furthermore, wave-ice interactions can play a vital role in fjord wave climate, particularly in Arctic fjords. During the winter season, a layer of ice can partially or completely cover the fjord surface, affecting the fetch and the wave growth. Along these lines, future investigations in fjords should take into account different offshore and local wave climates.

# **Chapter 5**

## **Scientific results**



# Paper I

## **The importance of wind forcing in fjord wave modelling**

Christakos, K., B.R. Furevik, O.J. Aarnes, Ø. Breivik, L. Tuomi, and Ø. Byrkjedal (2020), *Ocean Dynamics*, 70, 57-75.





# The importance of wind forcing in fjord wave modelling

Konstantinos Christakos<sup>1,2</sup> · Birgitte R. Furevik<sup>1,3</sup> · Ole Johan Aarnes<sup>1</sup> · Øyvind Breivik<sup>1,2</sup> · Laura Tuomi<sup>4</sup> · Øyvind Byrkjedal<sup>5</sup>

Received: 21 June 2019 / Accepted: 5 November 2019 / Published online: 3 December 2019  
© The Author(s) 2019

## Abstract

Accurate predictions of surface ocean waves in coastal areas are important for a number of marine activities. In complex coastlines with islands and fjords, the quality of wind forcing significantly affects the results. We investigate the role of wind forcing on wave conditions in a fjord system partly exposed to open sea. For this reason, we implemented the wave model SWAN at the west coast of Norway using four different wind forcing. Wind and wave estimates were compared with observations from five measurement sites. The best results in terms of significant wave height are found at the sites exposed to offshore conditions using a wind input that is biased slightly high compared with the buoy observations. Positively biased wind input, on the other hand, leads to significant overestimation of significant wave height in more sheltered locations. The model also shows a poorer performance for mean wave period in these locations. Statistical results are supported by two case studies which also illustrate the effect of high spatial resolution in wind forcing. Detailed wind forcing is necessary in order to obtain a realistic wind field in complex fjord terrain, but wind channelling and lee effects may have unpredictable effects on the wave simulations. Pure wave propagation (no wind forcing) is not able to reproduce the highest significant wave height in any of the locations.

**Keywords** Fjord · Wave modelling · Wind forcing · SWAN

## 1 Introduction

During the last decades, wave forecasts based on spectral wave models have achieved a high level of reliability in open seas. Wave parameters such as significant wave height, wave period, and direction can be predicted with high accuracy up to a week in advance (e.g., Bidlot et al.

2002; Janssen 2008, 2018). This has been achieved mainly through systematic development of numerical weather prediction models providing reliable wind input to wave models, and by recent improvements in the wind input and dissipation source terms (Babanin 2011) of wave models. Wave observations from satellite altimeters have been used extensively for calibration of wave models (Cavaleri and Sclavo 2006; Martínez-Asensio et al. 2013) providing wave data in over large ocean areas where buoy measurements are unavailable. Nowadays, the most widely used third generation spectral wave models are the Wave Model (WAM) (The Wamdi Group 1988), the Simulating Waves Nearshore model (SWAN) (Booij et al. 1999), and the WaveWatch-III model (The WAVEWATCHIII<sup>®</sup> Development Group 2016). Several studies based on these models have shown quite accurate results for open-ocean conditions (e.g., Reistad et al. 2011; Bertotti et al. 2014; Galanis et al. 2019; Amarouche et al. 2019; Stopa and Cheung 2014; Guedes Soares et al. 2016).

Despite these improvements, the quality of the wave forecasts is still not sufficient in the coastal and semi-enclosed seas (Cavaleri et al. 2018). Their performance has not been extensively evaluated in complex coastal areas and

---

Responsible Editor: Bruno Castelle

✉ Konstantinos Christakos  
konstantinos.christakos@met.no

<sup>1</sup> Norwegian Meteorological Institute, Allegaten 70, 5020, Bergen, Norway

<sup>2</sup> Geophysical Institute, University of Bergen, Allegaten 70, 5020, Bergen, Norway

<sup>3</sup> Danish Meteorological Institute, Lyngbyvej 100, 2100, Copenhagen, Denmark

<sup>4</sup> Finnish Meteorological Institute, Erik Palménin aukio 1, 00560, Helsinki, Finland

<sup>5</sup> Kjeller Vindteknikk AS, Gunnar Randers vei 24, 2027, Kjeller, Norway

their results cannot be used with as high level of reliability as for the open sea. The coastal topography affects the quality of simulated wind fields and consequently the wave fields. In addition, the presence of islands and shallow water areas makes the wave prediction more complicated. Moreover, for validation purposes, coastal observations are limited to point measurements (e.g., wave buoys) since remote sensing instruments such as satellite altimeters in coastal areas are not as reliable as in the open sea. This is mainly because the raw measurements are contaminated by land (Vignudelli et al. 2011).

Accurate wave predictions in coastal areas are essential for a number of coastal activities, e.g., infrastructure, maritime transport, aquaculture, and renewable energy applications. Furthermore, for coastal applications, information on both swell and wind sea is important. For instance, prediction of locally generated wind sea is essential for high-speed passenger ferries whereas information about the propagation of low-frequency swell in coastal areas and fjords is critical for the design of coastal structures or in the planning of marine operations.

When designing coastal structures or planning marine operations, it is important to know the wave conditions both in a statistical sense and in being able to forecast the wave conditions days ahead. In areas where swell have a strong influence and where extreme values of significant wave height and peak period due to storm conditions are of main interest, relatively good results may be obtained by propagation to coast of actual or parameter-based offshore spectra using a wave model or by establishing a statistical relationship between offshore hindcast and local wave measurements (Wang et al. 2018). As constructions become larger, or when marine operations or coastline are complex, more sophisticated methods that include the effect of local wind must be applied.

Global reanalyses (Laloyaux et al. 2018; Hersbach and Dee 2016; Poli et al. 2016) yield wind fields that can be used for wave applications. However, several studies show the importance of resolution in order to achieve accurate wave hindcasts. Lavidas et al. (2017) studied the sensitivity of wind input on a wave model for the Scottish region showing that the use of different reanalysis wind fields (ERA-Interim (Dee et al. 2011) and CFSR-NCEP (Saha et al. 2010) can significantly affect the quality of wave hindcasts. Moeini et al. (2010) assessed the quality of surface winds for wave simulations using SWAN in the Persian Gulf and found that ECMWF winds are underestimated and consequently that the wave model must be calibrated. Signell et al. (2005) studied the quality of four wind fields with different spatial resolution in the Adriatic Sea. They employed the SWAN model and similarly found that ECMWF wind fields are biased low. In addition to more realistic small-scale and spatial structure of wind fields during strong wind

events, the higher resolution models showed better over all performance for both wind speed and wave heights. Ponce de León et al. (2012) assessed four atmospheric models around the Balearic Islands for operational wave forecast. They conclude that spatial variability of wind forcing is a key factor for the small-scale features which coarse resolution models are not able to resolve. Arduin et al. (2007) studied the performance of four atmosphere models and three spectral wave models finding that quality of the wind input degrades approaching coastal areas, especially in cases with orographic effects.

On complex coastlines, as in archipelagos or fjord systems, wave modeling is a discipline of combining good offshore wave forecast with local wave production (Tuomi 2014a). In the transition zone from sheltered areas to swell-dominated outer parts, local wind may play a role in different ways. The ability of wave models to respond accurately to the local wind in combination with swell in such transition zones is the focus of the present study. The main objective of this study is to investigate the role of wind forcing on wave conditions in a semi-enclosed environment such as a fjord system. The study focuses on the effect of coastal wind forcing on wave simulations inside the fjord system which is located on the west coast of Norway.

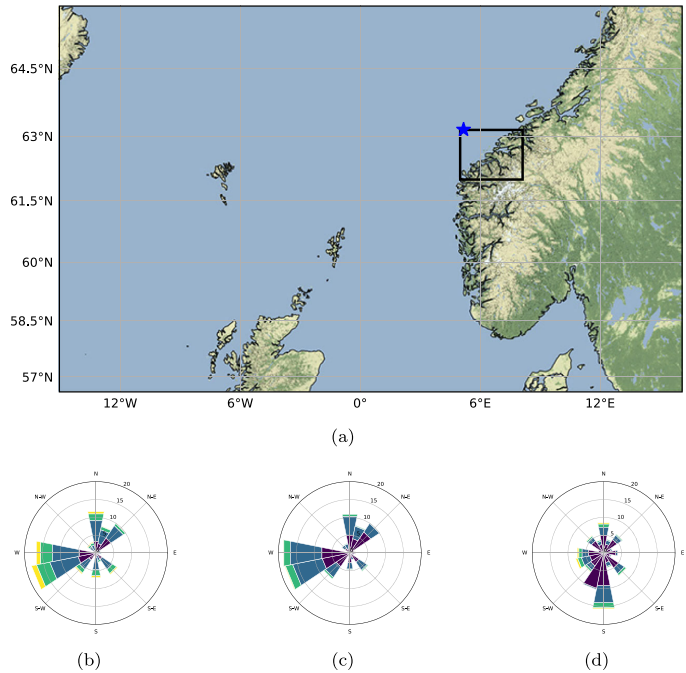
This paper is organised as follows. Section 2 is dedicated to the wave climate of our study area. Section 3 describes the data and methods. The evaluation of models and the results are presented in Section 4. Finally, Section 5 includes the discussion and Section 6 is following with the conclusions.

## 2 Background

### 2.1 Study area

The study is focused on a fjord system with several bifurcations located at the West coast of Norway (Fig. 1a). Figure 2a illustrates a terrain map with the bathymetry provided by the European Marine Observation and Data Network (EMODnet 2016) applied for SWAN wave simulations. It shows the two nested domains, the outer domain (D1), and the inner domain (D2) marked with a red rectangle. D1 spans the region 62 N° to 63.14 N°, and 5 E° to 8.12 E°. D2 shown in Fig. 2b contains the following fjords: Storfjorden (1), Hjørundfjorden (2), Sulafjorden (3), Vartdalsfjorden (4), Voldsfjorden (5), and Rovdefjorden (6) and measurement locations A, B, C, D, and F. Table 1 shows the fjord characteristics such as average length, width and depth range with the corresponding numbers as illustrated in Fig. 2b. The fjord system is more than 190 m deep at its deepest points. The longest fjords are Storfjorden and Hjørundfjorden, exceeding 30-km length. The shortest and widest fjord is Sulafjorden with 10-km

**Fig. 1** The location of the study area (rectangular) in the west coast of Norway (a). The area consists of islands and islets outside the fjord system. The directional roses show the frequency of waves at certain peak directions for total  $H_s$  (b), swell (c), and wind sea (d) components at a point (blue star) based on NORA10 dataset for the period: 09.1957–07.2018. Colors in directional roses: dark blue for  $H_s$  0–1.99 m, light blue for  $H_s$  2–3.99 m, green for  $H_s$  4–5.99 m, and yellow for  $H_s > 6$  m



average length and 4.6-km average width. Its narrowest part is 3.20 km (offshore inlet) and the widest part at 6km (cross section with Vartdalsfjorden). Sulafjorden is the only part of this fjord system that has a direct exposure to open sea conditions.

**2.2 Wave climate: offshore vs. fjord system**

Varlas et al. (2017) investigated the marine renewable resources along the Norwegian coast and found the highest average values of wave energy flux over the Norwegian Sea (close to our study area) where swell waves have the largest contribution to total wave energy. Similarly, Aarnes

et al. (2012) showed that Sulafjorden is situated in an area where wave energy generated in the Northeast Atlantic is let between the Faroes and Shetland, making this area one of the most exposed areas for extreme wave heights along the Norwegian coast. Close to this area, Christakos et al. (2014) studied the atmospheric phenomenon of a coastal low-level jet illustrating the need of a high-resolution model to predict the strong coastal winds and horizontal shear of the jet. The wave climate off the fjord system is characterized by a combination of swell and wind sea conditions (Reistad et al. 2011; Semedo et al. 2015). Figure 1 shows the directional roses for total, swell, and wind sea significant wave height ( $H_s$ ) at an offshore hindcast point in NORA10 (Norwegian

**Fig. 2** a Bathymetry of model outer (D1) and inner (D2) domains used for the wave simulations. The color bar shows the depth in meters b D2 of wave simulations. The numbers indicate the fjords (see Table 1) and the letters the positions of wave buoys (see Table 3)

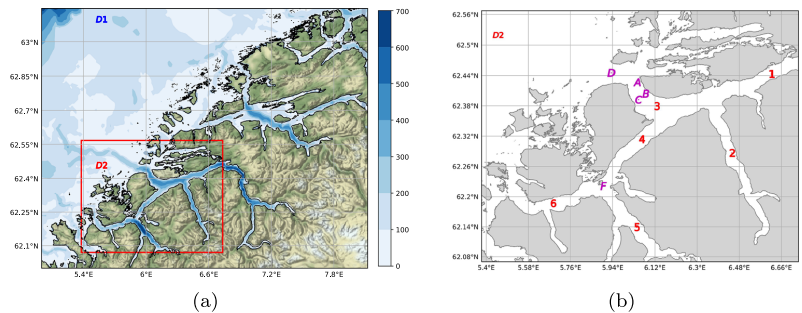


**Table 1** The characteristics of fjord system: average length (L), average width (W), and depth range (D), data derived by The Norwegian Coastal Administration (2019a)

No.	Fjord	L (km)	W (km)	D (m)
1	Storfjorden	35	2.7	250–650
2	Hjørundfjorden	31	2.1	190–440
3	Sulafjorden	10	4.6	230–450
4	Vartdalsfjorden	21	3.0	230–360
5	Voldsfjorden	25	2.5	320–680
6	Rovdefjorden	17	2.6	370–490

hindcast of wind and waves) where its wave component is the WAM model (Reistad et al. 2011). WAM defines the wave components that are still subject to wind forcing as wind sea while the rest part of the spectrum is defined as swell (ECMWF 2018).

Regarding total  $H_s$ , the dominant wave direction is west-southwest with a secondary direction from north-northeast. Separating the total  $H_s$  into swell and wind sea components, we observe the dominance of swell over wind sea component. The incoming swell from southwest and northeast is contributing the most to the wave conditions

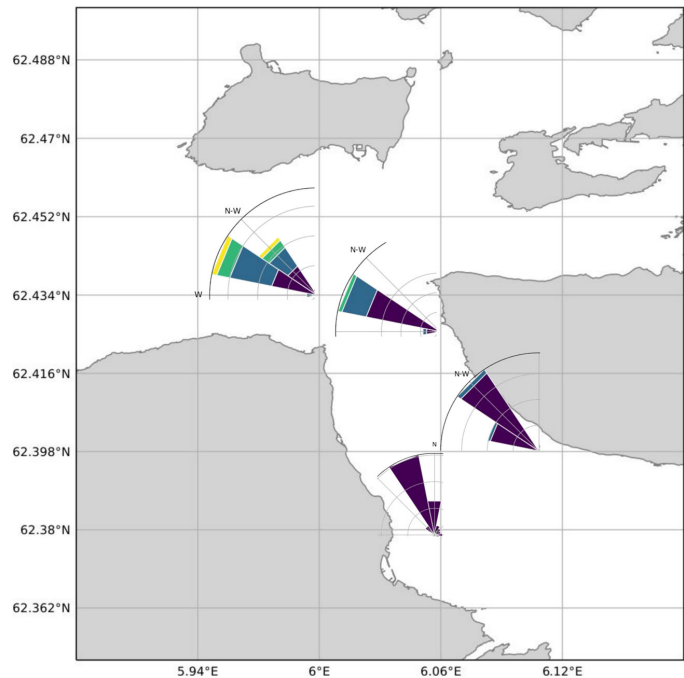
in the area. The directional distribution for wind sea is more scattered with a dominant direction from south and a secondary direction from north. It is noteworthy that the dominant southerly wind sea component is not observed in the total  $H_s$  rose. This feature can be explained by the fact that southerly wind sea is often accompanied by south/southwesterly swell, which dominates the total wave direction. However, the wave climate close to the coast and within the fjords is quite different. Figure 3 presents the directional wave distributions based on observations in Sulafjorden. The distributions are much more narrow compared with offshore conditions. This is mainly due to the presence of islands off the fjord system and the narrow fjord geometry (which funnels and speeds up the air flow) with short fetches that affect the shape of directional distribution.

### 3 Data and methods

#### 3.1 Atmospheric models

Surface winds from four different atmospheric models, including the ERA5 reanalysis (Copernicus Climate Change Service (C3S) 2017), NORA10 hindcast archive (Reistad

**Fig. 3** The directional roses show the frequency of waves for  $H_s$  at location D, A, B, and C. Colors in directional roses: dark blue for  $H_s$  0–0.99 m, light blue for  $H_s$  1–1.99 m, green for  $H_s$  2–2.99 m, and yellow for  $H_s > 3$  m



et al. 2011), AROME2.5 operational model (Müller et al. 2017), and WRF (Skamarock et al. 2008) are used for wave simulations in our study area.

### 3.1.1 WRF0.5

The WRF-ARW (Advanced Research WRF) (Skamarock et al. 2008) state-of-the-art numerical weather prediction model version 3.5.0 was used to downscale the reanalysis ERA-Interim (Dee et al. 2011) to a spatial resolution of 0.5 km for the study area. Four domains were used with two-way nesting. The parent domain is covering a large part of the North Atlantic, including the North Sea and the Norwegian Sea, with a horizontal resolution of 22.5 km. The second domain has a resolution of 4.5 km covering the south part of Norway and part of the Norwegian and the North Sea. The third domain has 1.5-km horizontal resolution and the innermost domain is focused on our region of interest with a resolution of 0.5 km. The model has been run with 51 vertical levels and approximately 8 levels within the lower 200 m of the atmosphere. The basic parameterization schemes applied for this hindcast are the following: Thompson microphysics, Rapid Radiative Transfer Model (RRTM) radiation scheme, and Mellor-Yamada-Janjic (MYJ) which is used for the vertical mixing in the boundary layer. A thermal diffusion scheme is used for the surface and the SST used is from ERA interim and updated daily. No cumulus parameterization is applied to the two inner domains, but the Kain-Fritsch scheme is used for the two outer domains. The surface wind calculated by WRF-ARW at 10 m above terrain for the 19-month period and applied as input to SWAN. The corresponding wave simulation is referred as SWAN-WRF0.5.

### 3.1.2 AROME 2.5 (AR2.5)

The Application of Research to Operations at Mesoscale (AROME) model is the core of the operational weather prediction model employed at MET Norway (Müller et al. 2017). The model is set up for the MetCoOp-domain with 2.5-km grid spacing and 65 levels. The forecasting suite consists of main forecast cycles at 00 and 12 UTC and intermediate cycles at 06 and 18 UTC. The analysis times of the European Centre for Medium-Range Forecasts (ECMWF) Integrated Forecasting System (IFS) forecasts used as boundaries for the main and intermediate cycles are 6 and 3 h earlier, respectively (Müller et al. 2017). The surface wind calculated by AROME at 10 m above terrain in 6-h forecasts from +3 to +8 from each of the cycles is put together for the 19-month period and used as input to SWAN. The corresponding wave simulation is referred as SWAN-AR2.5.

### 3.1.3 NORA10

NORA10, wind and wave hindcast developed by The Norwegian Meteorological Institute, covers the Norwegian Sea, Barents Sea, and the North Sea (Reistad et al. 2011). The atmospheric model is HIRLAM (High Resolution Limited-Area Model) (Undén et al. 2002) with 10-km horizontal resolution on a rotated spherical grid. The surface winds from HIRLAM are forcing the wave model WAM on the same grid, as described in Section 3.4. HIRLAM is set up with 40 vertical layers and is a dynamical downscaling of ERA-40 (Uppala et al. 2005) and ECMWF-IFS after September 2002. Further description of the model set-up is found in Bjørge et al. (2003). Winds from NORA10 are improved compared with ERA-40 and show good agreement against observations particularly in the coastal areas, e.g. Reistad et al. (2011) and Furevik and Haakenstad (2012). The corresponding wave simulation is referred as SWAN-NORA10.

### 3.1.4 ERA5

ERA5 (Hersbach and Dee 2016; Copernicus Climate Change Service (C3S) 2017) is the latest climate reanalysis product by ECMWF. The data set is available in the Climate Data Store on regular latitude-longitude grids at a horizontal resolution of about 31 km and 1-hour time steps. ERA5 data has finer horizontal and temporal resolution than its predecessor ERA-Interim (Dee et al. 2011) (about 80 km and 6-hourly). Several studies have shown the improvement of ERA5 winds relative to ERA interim. Belmonte Rivas and Stoffelen (2019) compared ASCAT wind observations to ERA5 and ERA interim, concluding that ERA5 shows better performance. Olason (2018) performed a comparison of MERRA-2 (Modern-Era Retrospective analysis for Research and Applications, Version 2) (Gelaro et al. 2017) and ERA5 datasets in terms of wind power, also concluding that ERA5 performs better. The corresponding wave simulation is referred as SWAN-ERA5.

### 3.1.5 No wind forcing (NWF)

An additional run with no wind forcing (NWF) is performed to visualize the dependency on the accurate description of incoming swell and the importance of local winds in the fjord system. The corresponding wave simulation is referred as SWAN-NWF.

## 3.2 Error metrics-taylor diagram

In order to illustrate error metrics at different locations, a Taylor diagram (Taylor 2001) is utilized. The error metrics

of the correlation coefficient ( $R$ ), normalized standard deviation (NSTD), and the normalized centered root means square error (CRMSE) are implemented in Fig. 4 for wind speed and significant wave height:

$$R = \frac{\sum_{i=1}^N (y_i - \bar{y})(x_i - \bar{x})}{\sqrt{\sum_{i=1}^N (y_i - \bar{y})^2} \sqrt{\sum_{i=1}^N (x_i - \bar{x})^2}} \tag{1}$$

$$NSTD = \frac{\sqrt{\frac{1}{N} \sum_{i=1}^N (y_i - \bar{y})^2}}{\sqrt{\frac{1}{N} \sum_{i=1}^N (x_i - \bar{x})^2}} \tag{2}$$

$$CRMSE = \frac{\sqrt{\frac{1}{N} \sum_{i=1}^N [(y_i - \bar{y}) - (x_i - \bar{x})]^2}}{\sqrt{\frac{1}{N} \sum_{i=1}^N (x_i - \bar{x})^2}} \tag{3}$$

where  $y_i$  are the model estimate,  $x_i$  are the observations,  $\bar{y}$  and  $\bar{x}$  the mean values, and  $N$  indicates the number of data pairs. The normalized parameters allow comparison along different areas within the fjord system.

### 3.3 The SWAN wave model

The wave model SWAN (Booij et al. 1999) is a state-of-the-art third generation spectral model designed for nearshore applications. SWAN is widely used for both operational and engineering applications. For this study, we implemented the SWAN cycle III version 41.20. SWAN is based on an implicit propagation scheme which is always numerically stable. Therefore, the SWAN model is suitable for simulating wave conditions in coastal and semi-enclosed environments where the grid resolution and thus the time step must be relatively small. The model propagates the action balance equation forward in time for the evolution of action density spectrum ( $N$ ):

$$\frac{\partial N}{\partial t} + \frac{\partial(c_x N)}{\partial x} + \frac{\partial(c_y N)}{\partial y} + \frac{\partial(c_\sigma N)}{\partial \sigma} + \frac{\partial(c_\theta N)}{\partial \theta} = \frac{S}{\sigma} \tag{4}$$

where  $c_x$  and  $c_y$  are the propagation group velocities in geographical ( $x, y$ )-space, respectively. The  $c_\sigma$  and  $c_\theta$  represent the propagation in spectral (frequency- $\sigma$ , direction- $\theta$ ) space. The term  $S(\sigma, \theta; x, y, t)$  is the total source term. It consists of three source terms,

$$S = S_{in} + S_{ds} + S_{nl} \tag{5}$$

Here,  $S_{in}$  is energy input generation due to wind,  $S_{ds}$  is the dissipation induced by whitecapping, bottom friction and depth-induced wave breaking. Finally,  $S_{nl}$  represents non-linear wave-wave interactions.

The model was run in non-stationary mode with spherical coordinates and a time step of 10 min. Thirty-six directions with  $10^\circ$  directional resolution and 32 discrete frequencies from 0.04 to 1 Hz were used as presented in Table 2. The inner domain with 250 m  $\times$  250 m (red rectangular

**Table 2** Model grid

Component	Grid definition
Directional resolution $\Delta\theta$	$10^\circ$
Frequency range	0.04–1 Hz
Spatial resolution ( $\Delta x, \Delta y$ )	
Outer domain	1 km $\times$ 1 km
Inner domain	250 m $\times$ 250 m

in Fig. 2a) grid cells is nested into the outer grid of 1 km  $\times$  1 km (Fig. 2a). The wave simulation period is from 01.10.2016 until 30.04.2018. The combination of the formulation by Yan (1987) for wind growth and non-linear saturation-based whitecapping based on Alves and Banner (2003) implemented in SWAN by van der Westhuysen et al. (2007) was chosen. According to the model modification page (in version 40.51 SWAN team 2019), this combination is more suitable for young waves than the default expression (Komen and Hasselmann 1984), offering a way to resolve the erroneous behavior of SWAN under combined swell-sea conditions (conditions that describe the wave climate in our study area). The bottom friction term is by Hasselmann et al. (1973) and depth-induced wave breaking by Battjes and Janssen (1978).

### 3.4 Boundary spectra

Spectral wave boundary conditions along the grid boundaries of the outer domain (D1) were in all simulations obtained from the NORA10 hindcast with 3-h temporal resolution (for details on the spectral nesting and interpolation procedure, see Breivik et al. 2009). The wave component of NORA10 is a 10-km WAM model forced with HIRLAM winds nested inside a 50-km North Atlantic WAM model forced by ERA-40 winds (Reistad et al. 2011). The wave component is a modified version of the WAM cycle 4 model (Gunther and Janssen 1992) set up on the same rotated spherical grid as HIRLAM. The outer domain of 50-km resolution covers the North Atlantic, allowing realistic swell propagation from the North Atlantic to the Norwegian coast. Twenty-four directional bins and 25 frequencies (0.0420 to 0.4137 Hz) were used for the model set-up. The quality of NORA10 wave hindcast has been evaluated through several studies. According to Aarnes et al. (2012), a low bias of significant wave height between NORA10 and observations located in the North Sea and the Norwegian Sea is observed. Bruserud and Haver (2016) found a good agreement between NORA10 and wave observations in the northern part of North Sea. Based on its good performance in open sea conditions, NORA10 is believed to provide reliable boundary data for the coastal wave model.

**Table 3** Mean and P99.9 of observed  $H_s$  (m) and wind speed -  $U$  ( $m\ s^{-1}$ ) at locations D, A, B, C, and F

Buoy	Latitude, longitude	Period	$\bar{H}_s$	P99.9 : $H_s$	$\bar{U}$	P99.9 : $U$
D	62.45, 5.93	10.2016–04.2018	1.3	5.8	5.8	16.7
A	62.43, 6.04	10.2016–04.2018	0.8	3.4	5.1	16.5
B	62.40, 6.08	10.2016–04.2018	0.4	2.1	3.8	15.3
C	62.39, 6.05	04.2017–04.2018	0.2	0.9	3.9	14.4
F	62.22, 5.90	11.2017–04.2018	0.2	1.0	5.3	15.7

### 3.5 Observations

Wind and wave measurement data from SEAWATCH Wavescan buoys (FUGRO 2012) were available via MET Norway Thredds Service (The Norwegian Meteorological Institute 2019b) to evaluate the performance of numerical simulations. The measurement data contains integrated wave parameters such as significant wave height, peak wave period, mean wave period, mean wave direction, as well as wind speed and wind direction. The wind sensors are placed 4.1 m above the sea level. The wave buoys D, A, B, and C are deployed in Sulafjorden and the buoy F in Vartdalsfjorden as illustrated in Fig. 2b. Table 3 shows the period of data availability for different wave buoys at the time of this study.

## 4 Results

### 4.1 Model validation

The quality of the wave model runs, their boundary, and wind forcing fields are evaluated by comparing wind speed,  $U$ , significant wave height,  $H_s$ , and mean wave period,  $T_{m01}$ , against buoy measurements at locations D, A, B, C, and F. According to Akpnr et al. (2012), inaccurate conclusions regarding the model performance of mean wave

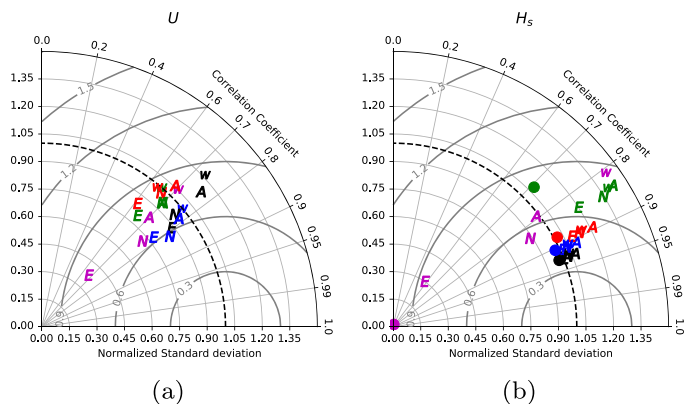
period can occur if the integration range does not match the buoy frequency range. Therefore,  $T_{m01}$  is estimated with the upper integration limit at 0.5 Hz which is the maximum frequency measured by the buoys. We use the logarithmic wind profile (6) to adjust the model wind speed ( $U_{10}$ ) from 10 to 4.1 m (wind sensor height) above the sea level assuming neutral conditions.

$$\frac{U_2}{U_1} = \frac{\ln((z_2 - d)/z_0)}{\ln((z_1 - d)/z_0)} \tag{6}$$

where  $U_1$  and  $U_2$  are the wind speed at the elevations of  $z_1$  and  $z_2$ ,  $d$  is the zero-plane displacement and it is considered zero in the fjord,  $z_0$  is the roughness length which is chosen to be 0.0002 m for open sea conditions according to revised Davenport roughness classification by Wieringa (1992). Moreover, the classification by Troen and Lundtang Petersen (1989) for water areas, i.e., lakes, fjords, and open sea where the roughness length is in order of  $10^{-4}$ , and a study focused on fjord wave conditions by Wang et al. (2018) support this choice.

The Taylor diagram for wind speed is presented in Fig. 4a. The different grid axis are the NSTD in light grey circles, the CRMSE in solid grey circles, and the correlation coefficient in lines. The five different symbols denote the different wind input: ERA5 (E), NORA10 (N), AR2.5 (A), WRF0.5 (W), and NWF (circle,  $H_s$  only). The colors correspond to different buoy locations. ERA5

**Fig. 4** Taylor diagram of error metrics for wind speed -  $U$  (a) and  $H_s$  (b) for different wave simulations at locations A (blue), B (red), C (green), D (black), and F (purple). The simulations with different wind forcing are indicated by letters; SWAN-ERA5 (E), SWAN-NORA10 (N), SWAN-AR2.5 (A) and SWAN-WRF0.5 (W). The full circles represents SWAN-NWF



winds have the lowest correlation coefficients at the inner fjord locations B, C, and F. ERA5 winds also exhibit too low variability (NSTD) compared with the observations, in particular at location F. WRF0.5 has the best performance in terms of variability at locations A, B, C, and F. For the most exposed location, D, all models perform well, but AR2.5 and WRF0.5 have too high variability (model activity).

Figure 4 b presents the Taylor diagram for significant wave height. The locations at the inlet of Sulafjorden (D and A) have the best match to the observations. For these locations the simulations with wind forcing do not deviate much from SWAN-NWF for average conditions. The results also show that the correlation coefficient,  $R$ , is decreasing from exposed to inner locations. More specific, for buoys located in the inlet of Sulafjorden (D and A), the correlation  $R$  is greater than 0.9. For buoys B and C located within Sulafjorden, the correlation coefficients are slightly reduced to 0.90 and 0.85 respectively.

The effect of local winds becomes more dominant in location F, where the absence of incoming swell makes the local wind a crucial parameter for wave growth. The results show that SWAN-NORA10 and SWAN-AR2.5 have a correlation coefficient close to 0.80, the lowest CRMSE and the best NSTD indicating a good match to observed data in this location.

For further investigation of the wave model performance for different wind input, the quantile-quantile ( $Q$ - $Q$ ) plot is used as illustrated in Fig. 5a, d, g, j, and m for locations D, A, B, C, and F respectively. The  $Q$ - $Q$  plots show that in most locations, WRF0.5 and AR2.5 have the tendency to overestimate the high wind speeds while NORA10 and ERA5 underestimate.

For wave buoys D and A located at the entrance of Sulafjorden, SWAN-NORA10, SWAN-ERA5, and SWAN-NWF underestimate  $H_s$  for the highest percentiles (Fig. 5b, e, h, k, and n). On the other hand, wave buoys B and C located in the inner part of Sulafjorden, all simulations with wind forcing overestimate  $H_s$  in the interval 0.5–1.5 m. The SWAN-NWF shows an underestimation for higher  $H_s$ .

Simulations of  $T_{m01}$  using SWAN-WRF0.5, SWAN-AR2.5, SWAN-NORA10, and SWAN-ERA5 over-predict  $T_{m01}$  at locations D, A, B, and C (Fig. 5c, f, i, and l). The over-prediction is stronger for high  $T_{m01}$ . Mean period is predicted fairly well in location F (Fig. 5o). SWAN-NWF clearly overestimates the observed mean wave periods at all locations. This overestimation becomes more pronounced for locations sheltered within the fjord system where the swell conditions are weaker and wind seas are stronger.

The  $H_s$  of SWAN-NWF shows that in Sulafjorden the wave system was well described by pure swell input up to certain  $H_s$  limit, i.e., 4 m at D, 2 m at A, 1 m at B, and 0.5 m at C. For higher values of  $H_s$ , e.g., during strong wind forcing, the local wind-induced waves become important

for the accuracy of wave predictions. Small differences in wind input can generate relative high variations on wave heights at location F. For winds greater than  $10 \text{ m s}^{-1}$ , WRF0.5 slightly overestimates observed wind speed in contrast to AR2.5 and NORA10 that underestimate it. This overestimation by WRF0.5 leads to a relatively high overestimation of  $H_s$  which will be investigated more in next section. The weaker winds produced by AROME and NORA10 give better results for  $H_s$ . ERA5 wind is significantly weaker than observations and this input fails to reproduce the wave conditions.

The use of a nested finer grid improves the quality of results in most of measurement locations (not shown). Especially in location C where sheltering by the island is dominant, wave parameters such as  $H_s$  and  $T_{m01}$  (Fig. 6) were improved using a nested fine grid by 36% and 4%, respectively.

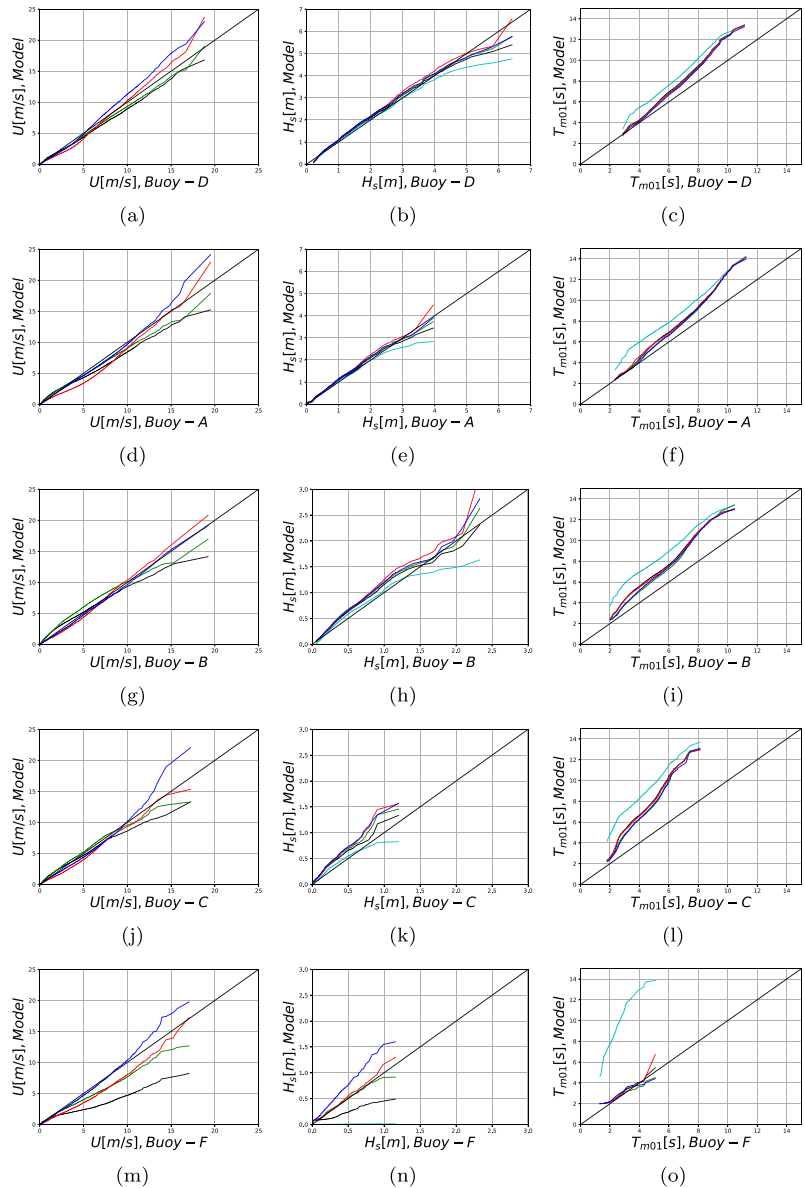
#### 4.1.1 Extreme wave conditions in the fjord system

The validation showed that the overall performance of the wave model is good, but obviously dependent on the quality of the forcing wind fields. However, considering the specific geometry and the narrowness of the fjords, only certain wind and swell conditions generate waves inside the fjords that may influence marine traffic or constructions. The highest mean value of  $H_s$ , 1.3 m, was seen at location D at the entrance of the fjord. The mean value of  $H_s$  was lowest at locations C and F (0.2 m) inside the fjord. Interestingly, the mean wind speed was considerably higher for location F than location C. The mean and 99.9th percentile for all locations are shown in Table 3. The case with the strongest onshore wind in location D (most exposed site) was on December 26, 2016 at 23:00 UTC and the case with the strongest offshore winds in location F (most sheltered site) was on January 15, 2018 at 07:00 UTC. These cases are marked with blue lines in Fig. 7. The onshore winds in the area are usually combined with incoming swell from the open ocean inducing high waves that penetrate into the fjord system. Also strong offshore winds can induce relatively high waves inside the fjords. During this type of events, the accuracy of the forcing wind field becomes even more important, since the wave fields consists mostly of local wind sea. We study these two cases in more detail to evaluate how the different wind forcing and the accuracy of the boundary wave spectra affect the wave simulations in the fjords.

#### 4.1.2 Onshore wind

On December 26, 2016, the extratropical cyclone causing the extreme weather “Urd” made landfall on the west coast of Norway with strong northwesterly mean winds

**Fig. 5** *Q-Q* plots of wind speed,  $H_s$  and  $T_{m01}$  at locations D, A, B, C, and F for different models SWAN-ERA5 (black), SWAN-NORA10 (green), SWAN-AR2.5 (red), SWAN-WRF0.5 (blue), and SWAN-NWF (cyan)

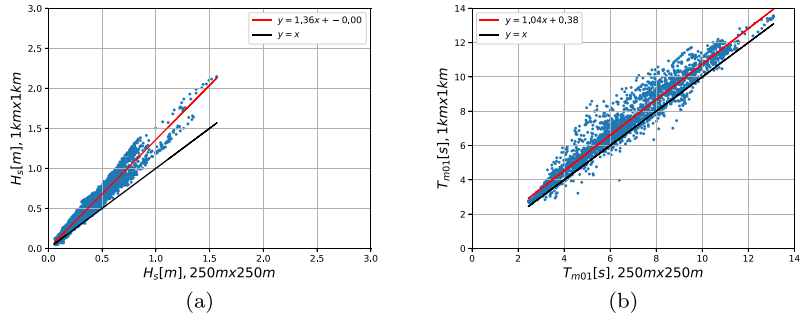


20–40 m s<sup>-1</sup> and gusts up to 53 m s<sup>-1</sup>, according to Olsen and Granerød (2017). The situation caused waves with  $H_s$  in excess of 6 m measured at location D.

Although onshore wind is relatively simple to model considering the absence of complex topography, differences in model wind fields are observed (Fig. 8a). The ERA5 and NORA10 winds have similar values and spatial variability

along the coast while within the fjords the ERA5 shows weaker winds. In contrast to ERA5 and NORA10, the higher resolution models AR2.5 and WRF0.5 are able to capture wind channeling and local jets induced by the fjords. The AR2.5 has the strongest winds along the coast but weaker within the fjords. The WRF0.5 wind field is weaker along the coast but it has larger gradients within the fjord system.

**Fig. 6** Scatter plots between different grid size (250 m × 250 m and 1 km × 1 km) for  $H_s$  and  $T_{m01}$  at location C. The values are derived by SWAN-WRF0.5 simulation



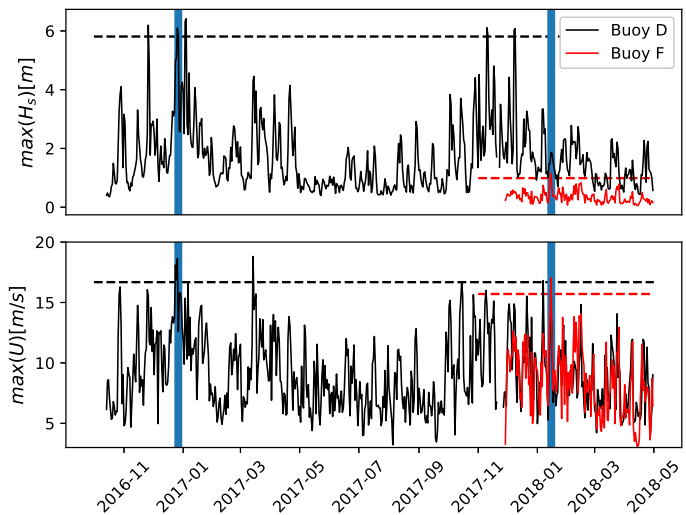
Since waves are an integrated product of the wind field in time and space, the wave fields derived from the different wind datasets reflect smoother wind characteristics as shown in Fig. 8b. In addition, the wave heights within the fjords are limited by the fjord geometry. Regarding  $H_s$  along the coast, the wave model results are quite similar with  $H_s$  exceeding 6 m. The application of high-resolution atmosphere models, i.e., SWAN-AR2.5 and SWAN-WRF0.5, shows deeper penetration of high waves within Sulafjorden compared with SWAN-ERA5 and SWAN-NORA10. This is mainly due to stronger coastal winds and strong local winds within Sulafjorden as illustrated in Fig. 8a.

For the investigation of model performance during the event of onshore wind, we analysed the time series of wind and wave parameters at the 3 available buoy locations, D, A, and B, in Fig. 9. The wind speed exceeding 15 m s<sup>-1</sup> and the westerly wind direction are captured by all models both in the inlet of Sulafjorden, location D and A, and

within the fjord at location B. The high-resolution wind fields of WRF0.5 and AR2.5 overestimate the peak of wind speed. AR2.5 has the strongest wind at the peak and its overestimation is higher at location D and less at A and B. Regarding  $H_s$ , the models perform similarly with good results. However, there is a 3-h delay between the highest model and observed peak of  $H_s$  at location D. Since the time of highest wind speed peak is well predicted by the models, the delay in  $H_s$  peak may be related to a delay in boundary spectrum (updated 3-hourly). At locations A and B, the strong wind of AR2.5 and WRF0.5 drive the wave model to overestimate the  $H_s$  peak. The northwesterly wave peak direction is well predicted at locations D and B while ca. 10 degrees off at location A during the event.  $T_p$  of 12–14 s are simulated with high degree of accuracy by the models in all three locations.

The comparison of one-dimensional wave energy spectra between model and measured spectra for the case of onshore wind at locations D, A, and B (no available

**Fig. 7** Time series of daily max values of  $H_s$  (top) and wind speed (bottom) at location D (black) and F (red). The dashed lines show the corresponding P99.9. The vertical blue lines indicate the selected extreme events that exceeds P99.9 values for both  $H_s$  and wind speed at locations D (first vertical line) and F (second vertical line)



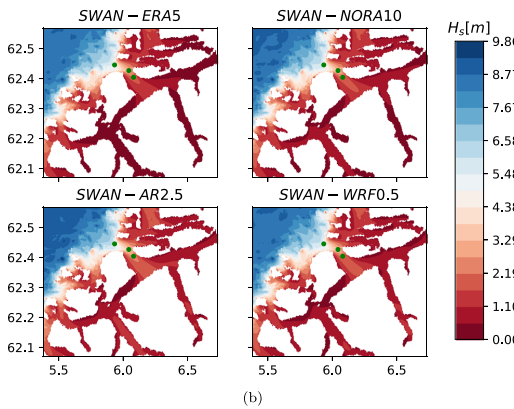
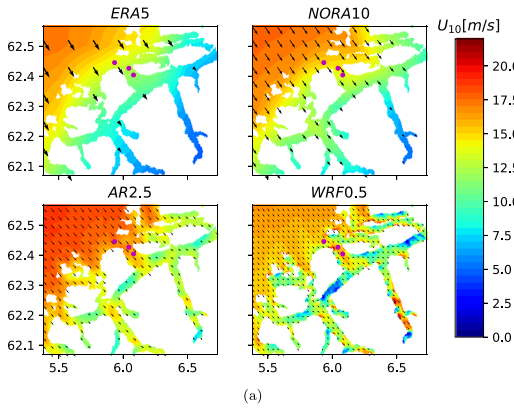


**Fig. 8** Wind (a) and significant wave height (b) snapshots from different models during storm Urd on December 26, 2016 at 23:00 UTC. The location of available measurements during this event are marked with dots. The arrows indicate the wind direction

spectra data at C and F) is presented in Fig. 10. The buoy wave spectra was averaged over the period (18 observed and 3 model spectra): December 26, 2016 at 22:00 to December 27, 2016, 00:00 UTC. The observed spectra shape at D is narrow around a single peak at 0.09 Hz. All model setups have broader spectral shape with a peak between 0.07 Hz (SWAN-NWF) and 0.08 Hz (SWAN-AR2.5) which underestimates the energy level compared with the observed peak. The peak related to SWAN-AR2.5 is closest to the observed in energy level and frequency. At the inlet of Sulafjorden, location A, the density peak is reduced by 1/3 in both observations and model. Similar to location D, the density peak is underestimated by the model setups with SWAN-AR2.5 closest to observations. SWAN-AR2.5 has the strongest wind forcing and its growth of the energy at peak (location D and A) indicates that the

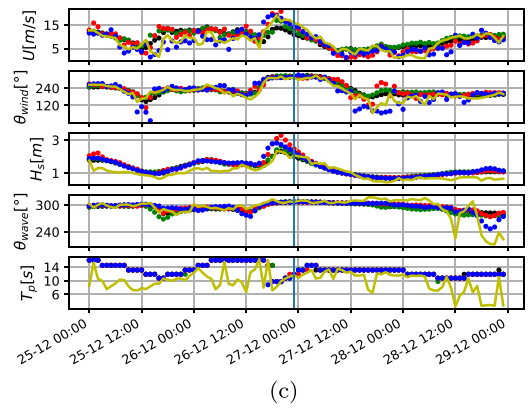
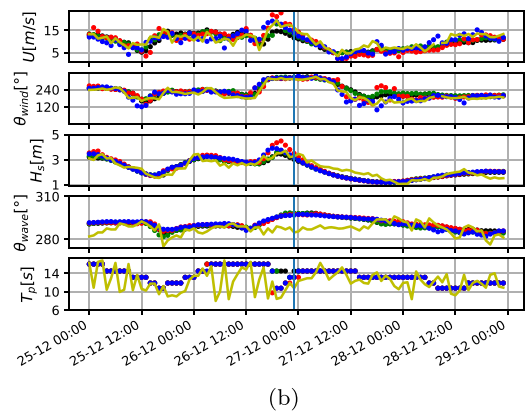
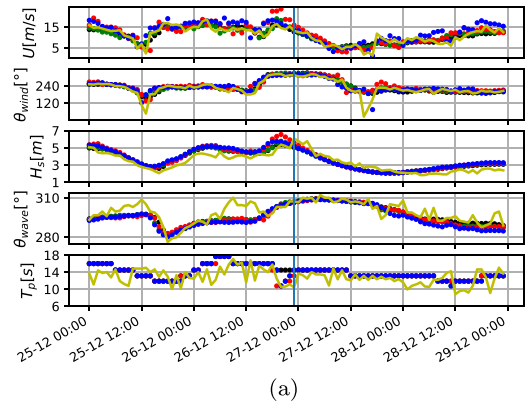


**Fig. 9** Time series comparison of observed (yellow) and modeled (SWAN-ERA5: black, SWAN-NORA10: green, SWAN-AR2.5: red and SWAN-WRF0.5: blue) wind and wave parameters at location D (a) and A (b) and B (c) during the onshore wind conditions (December 26, 2016). The blue vertical line indicates the time of snapshot in Fig. 8

long waves are still under influence of winds. However, the spectra tail is overestimated by SWAN-AR2.5. The absence of wind forcing in NWF simulations naturally results to an underestimation of both the density peak and spectra tail at locations D and A. In these locations, the density peak is quite similar to the SWAN-ERA5 and SWAN-NORA10, emphasizing the role of incoming swell at these locations. Within Sulafjorden at location B, we observe the development of a double-peaked spectra of locally generated wind sea in combination with the swell in Sulafjorden. The energy level of long waves is reduced by 3.5 times compared with location A. The spectral peak is now well represented in AR2.5 but is still underestimated by all other model setups. This is related to the higher winds in the open sea areas, which are still able to elevate the wave energy before it enters the fjord system. The peak of wind sea at around 0.25 Hz is overestimated in energy by the models SWAN-WRF0.5. SWAN-AR2.5, SWAN-NORA10, and SWAN-ERA5 and located at lower frequency of 0.2 Hz. In addition, a small difference between the observed and model peak frequency can be explained either by a small fail in boundary spectra or/and the wave propagation through an area of islands and islets outside the fjord system.

#### 4.1.3 Offshore wind

On January 15, 2018, there was an event of strong southeasterly wind exceeding  $15 \text{ m s}^{-1}$  within the fjord system, generating a strong wind sea misaligned with an incoming swell from the open sea. Figure 11 a presents a snapshot of the wind fields from the four atmospheric models during this event. In this case, the wind field is influenced by the complex orography and significant differences are visible. NORA10 and ERA5 winds both have low spatial variability but NORA10 shows a stronger wind field both offshore and in the fjords. AR2.5 and WRF0.5, due to their high resolution which is comparable with the fjord geometry, show areas of intensification and lee effects related to the topography. WRF0.5 has the highest winds both on the coast and within the fjords with

stronger jets leading to strong horizontal gradients and high spatial variability.

Figure 11 b shows a snapshot of  $H_s$  as derived using different wind forcing at the same event. The wave field again reflects the characteristics of different wind fields in a smoother way. Although the model setups show similar results along the coast, significant differences are observed within the fjords. SWAN-ERA5 results show the lowest  $H_s < 0.55 \text{ m}$  within the fjords with no spatial variability reflecting the applied low wind forcing. SWAN-NORA10 shows a slightly higher spatial variability within the fjords with  $H_s < 1.1 \text{ m}$ . SWAN-AR2.5 and SWAN-WRF0.5 wave fields reflect the presence of jets within the fjords showing higher spatial variability and local maximum at fjord cross-sections generated by the strong jets. Both SWAN-AR2.5 and SWAN-WRF0.5 result in a local maximum of  $H_s$  exceeding  $1.1 \text{ m}$  at the cross-section of Storfjorden (1) and Hjørundfjorden (2). For the investigation of model performance during the event of offshore winds, we analysed the time series of wind and wave parameters at the 5 buoy locations, D, A, B, and C in Fig. 12 and F in Fig. 13.

For the exposed locations D and A, wind speed is overestimated by WRF0.5, AR2.5, and NORA10 and it is underestimated by ERA5. The wind direction is from southeast and it is well predicted by all models. All models overestimate  $H_s$ , with the highest overestimation by WRF0.5. At location D, the observed mean wave direction is from west indicating the direction of incoming swell which is well predicted by the models. However, at location A, the observed mean wave direction turns from  $270$  to  $220^\circ$ . These deviations are captured better with SWAN-WRF0.5 and SWAN-AR2.5. The models show good performance to simulate the peak periods of long waves with  $T_p$  ca.  $14 \text{ s}$  during this event at D and A.

For locations within Sulafjorden at B and C, the model results vary more than at locations D and A. At location B, WRF0.5 and NORA10 show the best performance with slightly overestimation of the wind speed while at location C, AR2.5 and NORA10 perform better. In both locations,

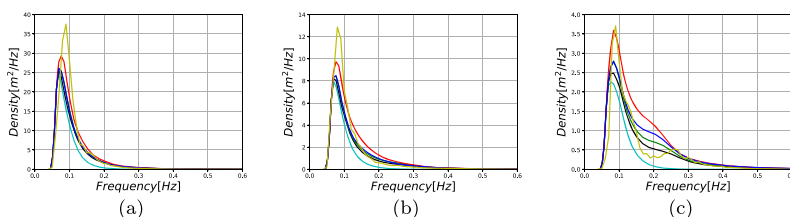
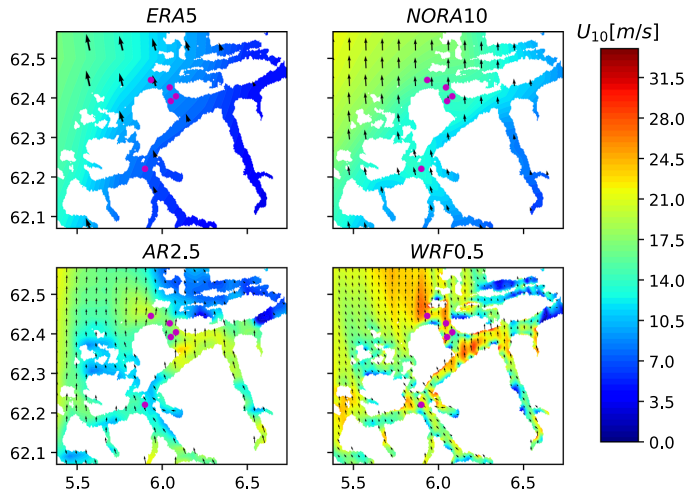


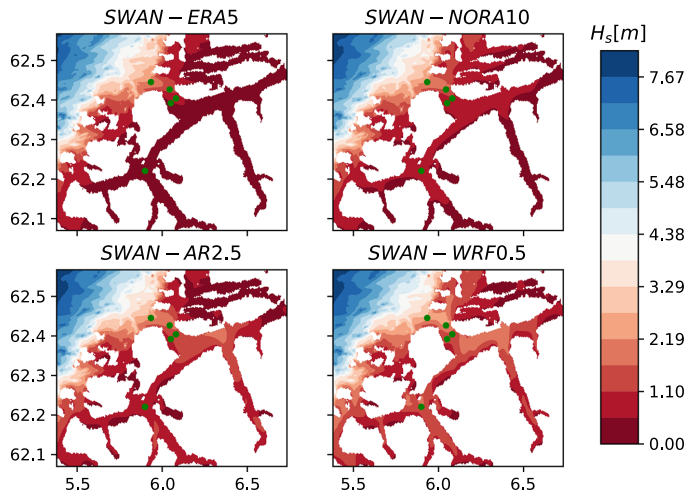
**Fig. 10** Comparison of one-dimensional wave energy density, averaged during period: December 26, 2016 at 22:00 to December 27, 2016 00:00 UTC, between model(SWAN-ERA5: black, SWAN-NORA10: green, SWAN-AR2.5: red, SWAN-WRF0.5: blue and SWAN-NWF:

cyan) and measured spectra (yellow) for case of onshore wind at location D (a), A (b), and B (c). The energy density (y-axis) is adjusted to different location

**Fig. 11** Wind (a) and significant wave height (b) snapshots from different models during an offshore wind event on January 15, 2018, at 07:00 UTC. The location of available measurements during this event are marked with dots. The arrows indicate the wind direction



(a)



(b)

ERA5 underestimates the wind speed. The southeasterly wind direction is simulated well for all models. Following the overestimation of wind speed, SWAN-WRF0.5, SWAN-AR2.5, and SWAN-NORA10 predict higher values for  $H_s$  and SWAN-ERA5 gives good results in  $H_s$  in spite of the low wind speed. In contrast to SWAN-WRF0.5, SWAN-AR2.5 and SWAN-NORA10 predict wave direction with good accuracy. SWAN-ERA5 is not able to capture the deviation in wave direction from 260 to 180° in location B. The observed  $T_p$  is lower than 6 s in both locations showing that the wind sea is dominant in these locations. The results

indicate that only the higher resolution wind fields provide realistic  $T_p$  and wave direction within Sulafjorden.

For location F in Vartdalsfjorden, the observed wind speed of  $16 \text{ m s}^{-1}$  is the highest during this event. WRF0.5 slightly overestimates the observed wind by  $2\text{--}3 \text{ m s}^{-1}$ . AR2.5 and NORA10 winds range  $10\text{--}15 \text{ m s}^{-1}$ . ERA5 winds are weaker ( $< 10 \text{ m s}^{-1}$ ). The strong wind speed with a southeasterly wind direction along Voldsfjorden (5) illustrates a phenomenon of wind channeling due to orography. Both wind and wave directions are predicted well by all models. However, the modeled  $H_s$  and  $T_p$  deviate

**Fig. 12** Time series comparison of observed (yellow) and modeled (SWAN-ERA5: black, SWAN-NORA10: green, SWAN-AR2.5: red and SWAN-WRF0.5: blue) wind and wave parameters at location D (top-left), A (top-right), B (bottom-right) and C (bottom-left) during the offshore wind conditions (January 15, 2018). The blue vertical line indicates the time of snapshot in Fig. 11

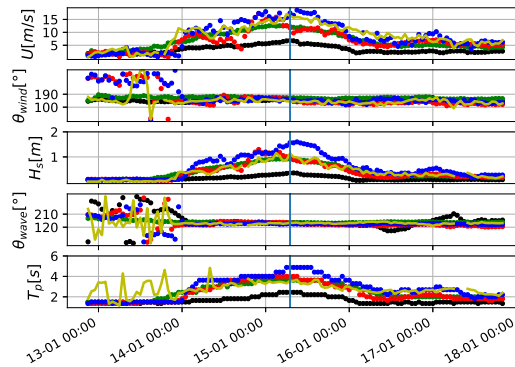
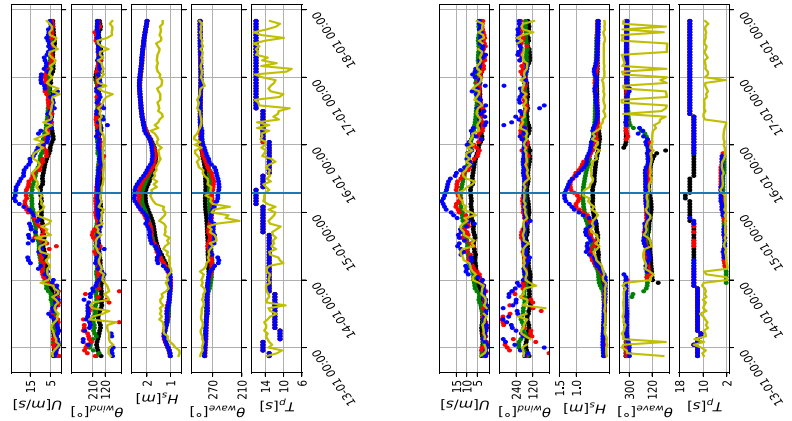
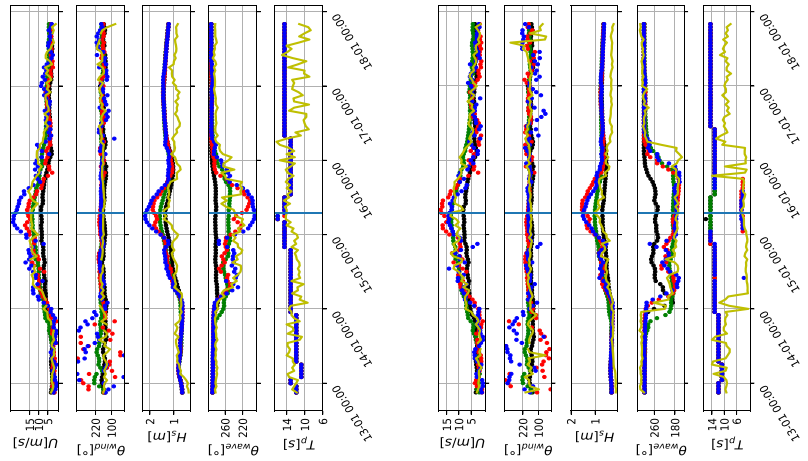


**Fig. 13** Time series comparison of observed (yellow) and modeled (SWAN-ERA5: black, SWAN-NORA10: green, SWAN-AR2.5: red and SWAN-WRF0.5: blue) wind and wave parameters at location F during the offshore wind conditions (January 15, 2018). The blue vertical line indicates the time of snapshot in Fig. 11

from the observations. The overestimation of wind forcing by WRF0.5 leads to over-estimation of  $H_s$  by 0.6 m and  $T_p$  by 1 s while ERA5 leads to underestimation. On the other hand, the wind forcing of AR2.5 and NORA10 gives the best results compared with observations of both  $H_s$  and  $T_p$ . Due to weak ERA5 wind forcing, the corresponding  $H_s$  and  $T_p$  are underestimated. The results indicate a strong dependency of wave parameters on local wind conditions.

### 4.2 Effect of wind forcing during extremes

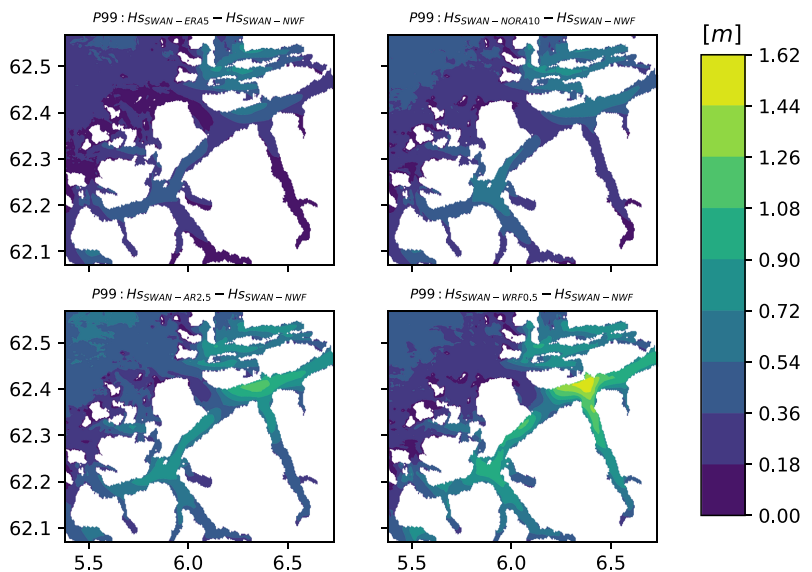
To investigate the effect of different wind forcing within the fjord system, we estimated the  $H_s$  difference between wave simulations with and without wind forcing. This allows us to detect areas where the wave estimates are affected significantly by the resolution of wind forcing. Figure 14 illustrates the difference between the 99th percentile (P99) of  $H_s$  forced by ERA5, NORA10, AR2.5, and WRF0.5 with the P99 of  $H_s$  with no wind forcing for the 19-month period (October 1, 2016–April 30, 2018). The high-resolution wind fields of WRF0.5 and AR2.5 show high differences up to 1.60 m and 1 m in the intersection of Storfjorden (1), Hjørundfjorden (2), and Vartdalsfjorden (4). A second area with large  $H_s$  differences is the intersection of Vartdalsfjorden (4), Voldsfjorden (5), and Rovdefjorden (6) (in location F) with differences of 1 m and 0.7 m, respectively. These areas are also seen in NORA10 but less distinctly so. On the other hand, SWAN-ERA5, due to its coarse resolution of wind field, is not able to capture these differences. In addition to these high  $H_s$  difference areas

within the fjord system, we observe high differences along the coast up to 1 m for SWAN-NORA10, SWAN-AR2.5, and SWAN-WRF0.5 and up to 0.7 for SWAN-ERA5. In contrast to areas with large differences in  $H_s$ , Sulafjorden show low difference for all models indicating the dominant role of swell over wind sea in this fjord.

## 5 Discussion

The wave climate on the Norwegian coast with islands, islets and fjords is a challenge to model correctly in both the inner and outer parts. In such areas, in addition to the uncertainties due to the physics and choices in the setup in wave models, the quality of the boundary conditions, i.e. spectra on the open boundaries and wind input significantly affect the results. The quality of wind fields in complex terrain is related to the grid size of the atmosphere model. Within the fjord system, the finest grid of WRF0.5 shows the best performance in terms of variability while the coarse ERA5 winds are too weak. As the spatial resolution increases, terrain features of fjords such as high mountains and steep slopes become better resolved. Since the average fjord narrowness (width) is 2.9 km, only atmosphere models with smaller grid size (e.g., WRF0.5 and AR2.5) are capable of reproducing the topographic features. Especially during extreme wind events within the fjords, the fine grid of WRF0.5 and AR2.5 can capture local wind phenomena such as wind channeling induced by the orography illustrating a more realistic structure (Figs. 8a and 11a). However, the

**Fig. 14** The P99 of  $H_s$  difference between SWAN-ERA5, SWAN-NORA10, SWAN-AR2.5, SWAN-WRF0.5 and SWAN-NWF



high-resolution models have been shown to overestimate the wind speeds especially during high wind and storm events which is also observed in other studies (Signell et al. 2005).

Regarding the overall performance of the wave model SWAN, we found that it was able to simulate well the wave conditions in and close to the entrance of the fjords, where the swell is dominant (D and A). Further inside the fjord system, e.g., within Sulafjorden (B and C), the wind sea becomes more dominant and the accuracy of the wind input more significant (Fig. 4b). Even if B and C are in quite close distance (ca. 2 km), C is more sheltered from offshore wave conditions making it more sensitive to different wind forcing. It is noteworthy that the poorest model performance is observed in the locations least exposed to the open sea where swell is weak or absent (C and F). In location F, the effect of swell is absent (in both model and observed data) and the wind forcing alone controls the wave climate. Due to its location in the intersection of three long and narrow fjords (Vartalsfjorden (4), Voldsfjorden (5), and Rovdefjorden (6)), the fjord geometries (width: 2.5–3 km, length: 17–25 km) and the relative high mountains which surround them (height: up to 1000 m) complicate the wind and consequently the wave prediction. The results show poor overall error metrics and large deviations between the different model setups. The ERA5 wind is too weak to provide good wave results. Comparing observations to  $H_s$  derived by a coarse grid (1 km  $\times$  1 km) and a fine grid (250 m  $\times$  250 m), we observe that the use of a nested finer grid improves the quality of results (see Fig. 6). For instance,  $H_s$  of the fine grid is more accurate at location D by 4%, A by 15%, C by 36% and B by 1% (shown only for C). In contrast, at location F, the coarse grid gives slightly better results (not shown). Thus, a higher spatial resolution (< 250 m) may improve the results at location C but not in F where the problem seems to be related to different factors (discussed below). No improvement in wave estimates ( $H_s$  and  $T_{m01}$ ) are found by increasing the directional resolution from 10 to 5 degrees (not shown).

Even if overall wave statistics are good, during extreme conditions the quality of wind forcing becomes a crucial factor since the coarse wind fields are much weaker at all locations. At the outer locations, D and A, strong coastal wind affects significantly the wave conditions. Our results indicate that the highest  $H_s$  cannot be reached without wind forcing. More specific, during the onshore wind case, AR2.5 has the highest spectral peak indicating that its higher coastal wind enhances (Fig. 8a) the energy level of incoming long waves which lead to a deeper penetration of offshore waves within Sulafjorden (Fig. 8b) but impairs the spectral shape. However, the higher resolution forcing did not lead to a better wave model performance in all situations. In location F,  $H_s$  is overestimated by up to 0.5 m with WRF0.5 wind forcing even if WRF0.5 provides the best

wind at the location with only a slight overestimation (2–3 m s<sup>-1</sup>) of the high wind speed. Here, NORA10 and AR2.5 show weaker wind, but still providing more accurate wave heights. Due to relative short availability of measurement data (ca. 6 month) at location F, it is difficult to make firm conclusions. We expect that the overestimation by SWAN-WRF0.5 is related to the calibration of deep water source terms and the accuracy of wind forcing along the fjord. Due to large depth of this region, only the source terms of wind input, whitecapping dissipation and non-linear wave-wave interactions (quadruplet) are of significant importance. In case of strongly forced waves (inverse wave age greater than 0.1), van der Westhuysen et al. (2007) indicated that the wind input formulation becomes non-linear i.e. the rate of wind-induced growth has a quadratic dependency on the inverse wave age. During these conditions, small differences in wind forcing can have significant impact on wave conditions. Therefore, a re-calibration of wind input or/and whitecapping dissipation may improve the model estimates at location F. Mao et al. (2016) showed that a re-calibration of whitecapping formulation leads to improvements in model performance. Nevertheless, this may have negative effect on the other locations. Another important factor is the accuracy of wind forcing, even if WRF0.5 shows an overall good performance, our evaluation is based on point measurement not allowing accurate conclusion about the wind quality along the fjord. Considering that the offshore winds are more challenging to predict due to the complexity of topography in the region, the accuracy of wind along the fjords plays a significant role on the wave growth. Similar coastal wave studies by Tuomi et al. (2014b) have shown that the higher resolution wind forcing does not necessarily lead to better wave model performance.

Compared with  $H_s$ , wave period is a more challenging parameter to model. Simulations of  $T_{m01}$  with wind forcing perform similarly while the simulations of NWF clearly fails at all locations. Nevertheless, if the boundary spectra are estimated with too low/high energy level by the offshore wave hindcast (NORA10), the coastal wave model may not be able to correct this inaccuracy. For high mean wave periods, Reistad et al. (2011) found that NORA10 overestimates the observed data indicating that certain swell conditions may not be well predicted. These potential inaccuracies in our boundary spectra are consequently transferred in the coastal wave predictions. This becomes clear in locations D and A where SWAN overestimates the observed wave periods for  $T_{m01} > 4$  s (Fig. 5). The inaccurate model results at location C are also observed in mean wave period. The modelled  $T_{m01}$  for C is similar to B, over-predicting the observed values; however, the highest observed periods are reduced by 2 s, i.e., from 10 to 8 s, indicating that the model is not able to capture accurately the reduction of  $T_{m01}$  for long waves within Sulafjorden.

The model fails to capture the sheltering effects at location C due to the sheltering of the island to the southwest. Based on our simulations, the  $T_{m01}$  was improved by the use of a nested fine grid of 250 m. Therefore, an increase of spatial resolution ( $< 250$  m) rather than directional resolution may resolve better these sheltering effects improving  $T_{m01}$  estimates.

Most of available buoy measurements (4 out of 5) are located in the inlet and within Sulafjorden allowing us to validate the modelled wind and wave estimates in a fjord with exposure to open sea conditions. However, there is a need for more measurements within the fjord system where large differences between the models are observed. For instance, the highest  $H_s$  differences (Fig. 14) are observed in the intersection of Storfjorden (1), Hjørundfjorden (2) and Vartdalsfjorden (4) where there are no available observations and therefore it is not possible to extract any information about the model performance.

Finally, the choice of wind input should be decided by the area of interest. Along the coastline and in exposed locations to open sea, the coarse wind fields can give reasonable wave estimates since the quality of boundary wave spectra is most important. Inside the fjord system, the fjord geometry is the key factor for the selection of the spatial resolution of wind forcing. However, in narrow fjords where a high resolution wind field is needed, possible overestimation of high winds can lead to significant overestimation of waves such as in location F. Therefore, methods such as tuning of source terms should be considered for future model implementations.

## 6 Conclusions

In this study, SWAN is set up for a fjord system on the west coast of Norway. Simulations with four different wind forcing (with spatial resolution; 0.5 km, 2.5 km, 10 km, and 31 km) and one with no wind were applied to assess the wave model quality. Both modeled wind and wave are compared with observations from five measurement sites. The performance of the wave model is better for the exposed locations where swell conditions are dominant. The poorest model performance is observed in the locations least exposed to the open sea where swell is weak or absent (locations C and F). The fine grid of WRF0.5 captures local wind phenomena such as wind channeling, but leads to overestimation of the waves within the fjords (location F). This is believed to be due to a tuning of SWAN to coastal conditions. Our results show that the wave estimates at location C may be improved by increasing the spatial resolution ( $< 250$  m). During extreme situations, the local wind-induced waves become crucial for the accuracy of wave estimates and especially for the most

exposed locations, where the high resolution wind forcing fields (WRF0.5 and AR2.5) give better results. Pure wave propagation without local wind forcing fails to reproduce realistic mean wave periods and the highest significant wave height in any of the locations.

**Acknowledgments** We would like to thank the anonymous reviewers for their suggestions and comments that improved the manuscript. We are grateful to Lasse Lønseth (Fugro OCEANOR AS) who provided the wave spectral data. Wind and wave measurements were available via MET Norway Thredds Service at Norwegian Meteorological Institute. Finally, we would like to thank EMODnet Bathymetry Consortium (2018) for the bathymetry data and the SWAN team at Delft University of Technology, The Netherlands for developing the SWAN wave model.

**Funding information** This study was supported by the Norwegian Public Roads Administration under the Coastal Highway Route E39 project.

**Open Access** This article is distributed under the terms of the Creative Commons Attribution 4.0 International License (<http://creativecommons.org/licenses/by/4.0/>), which permits unrestricted use, distribution, and reproduction in any medium, provided you give appropriate credit to the original author(s) and the source, provide a link to the Creative Commons license, and indicate if changes were made.

## References

- Aarnes OJ, Breivik Ø, Reistad M (2012) Wave extremes in the North-east, Atlantic. *J Clim* 25(5):1529–1543. <https://doi.org/10.1175/JCLI-D-11-00132.1>
- Akpınar A, van Vledder GP, hsan Kömürçü M, Özger M (2012) Evaluation of the numerical wave model (swan) for wave simulation in the black sea. *Cont Shelf Res* 50–51:80–99. <https://doi.org/10.1016/j.csr.2012.09.012>, <http://www.sciencedirect.com/science/article/pii/S0278434312002671>
- Alves JHGM, Banner ML (2003) Performance of a saturation-based dissipation-rate source term in modeling the fetch-limited evolution of wind waves. *J Phys Oceanogr* 33(6):1274–1298
- Amarouche K, Akpınar A, Bachari NEI, Çakmak R, Houma F (2019) Evaluation of a high-resolution wave hindcast model SWAN for the west Mediterranean basin. *Appl Ocean Res* 84:225–241. <https://doi.org/10.1016/j.apor.2019.01.014>
- Arduin F, Bertotti L, Bidlot J, Cavaleri L, Filipetto V, Lefevre JM, Wittmann P (2007) Comparison of wind and wave measurements and models in the western Mediterranean sea. *Ocean Eng* 34:526–541. <https://doi.org/10.1016/j.oceaneng.2006.02.008>
- Babanin A (2011) Breaking and dissipation of ocean surface waves. *Breaking and Dissipation of Ocean Surface Waves*. doi:10.1017/CBO9780511736162
- Battjes J, Janssen J (1978) Energy loss and set-up due to breaking random waves. *Proceedings of 16th Conference on Coastal Engineering, ASCE*, pp 569–588
- Belmonte Rivas M, Stoffelen A (2019) Characterizing ERA-interim and ERA5 surface wind biases using ASCAT. *Ocean Sci* 15(3):831–852. <https://doi.org/10.5194/os-15-831-2019>, <https://www.ocean-sci.net/15/831/2019/>
- Bertotti L, Cavaleri L, Soret A, Tolosana-Delgado R (2014) Performance of global and regional nested meteorological models. *Cont Shelf Res* 87:17–27. <https://doi.org/10.1016/j.csr.2013.12.013>

- <http://www.sciencedirect.com/science/article/pii/S02784341400053>, oceanography at coastal scales
- Bidlot JR, Holmes DJ, Wittmann PA, Lalbeharry R, Chen HS (2002) Intercomparison of the performance of operational ocean wave forecasting systems with buoy data. *Weather Forecast* 17(2):287–310. [https://doi.org/10.1175/1520-0434\(2002\)017<0287:IOPTO>2.0.CO;2](https://doi.org/10.1175/1520-0434(2002)017<0287:IOPTO>2.0.CO;2)
- Bjorge D, Haugen JE, Homleid M, Vignes O, Ødegaard V (2003) Updating the HIRLAM numerical weather prediction system at met.no 2000–2002. Tech. Rep. 145, Norwegian Meteorological Institute
- Booij N, Ris RC, Holthuijsen LH (1999) A third-generation wave model for coastal regions: 1. model description and validation. *J Geophys Res: Oceans* 104(C4):7649–7666. <https://doi.org/10.1029/98JC02622>
- Breivik Ø, Gusdal Y, Furevik BR, Aarnes OJ, Reistad M (2009) Nearshore wave forecasting and hindcasting by dynamical and statistical downscaling. *J Mar Syst* 78(2):S235–S243. <https://doi.org/10/cbvwqd>
- Bruserud K, Haver S (2016) Comparison of wave and current measurements to NORA10 and NoNoCur hindcast data in the northern North Sea. *Ocean Dyn* 66(6):823–838. <https://doi.org/10.1007/s10236-016-0953-z>
- Cavaleri L, Sclavo M (2006) The calibration of wind and wave model data in the Mediterranean Sea. *Coast Eng* 53(7):613–627. <https://doi.org/10.1016/j.coastaleng.2005.12.006>, <http://www.sciencedirect.com/science/article/pii/S0378383906000020>
- Cavaleri L, Abdalla S, Benetazzo A, Bertotti L, Bidlot JR, Breivik Ø, Carniel S, Jensen R, Portilla-Yandun J, Rogers W, Roland A, Sanchez-Arcilla A, Smith J, Staneva J, Toledo Y, van Vledder G, van der Westhuysen A (2018) Wave modelling in coastal and inner seas. *Progress in Oceanography*. <https://doi.org/10.1016/j.pocean.2018.03.010>
- Christakos K, Varlas G, Reuder J, Katsafados P, Papadopoulos A (2014) Analysis of a low-level coastal jet off the western coast of Norway. *Energy Procedia* 53:162–172. <https://doi.org/10.1016/j.egypro.2014.07.225>
- Copernicus Climate Change Service (C3S) (2017) ERA5: Fifth generation of ECMWF atmospheric reanalyses of the global climate. Copernicus Climate Change Service Climate Data Store (CDS), date of access: 20-01-2018. <https://cds.climate.copernicus.eu/cdsapp>
- Dee DP, Uppala SM, Simmons AJ, Berrisford P, Poli P, Kobayashi S, Andrae U, Balmaseda MA, Balsamo G, Bauer P, Bechtold P, Beljaars ACM, van de Berg L, Bidlot J, Bormann N, Delsol C, Dragani R, Fuentes M, Geer AJ, Haimberger L, Healy SB, Hersbach H, Hólm EV, Isaksen L, Kållberg P, Köhler M, Matricardi M, McNally AP, Monge-Sanz BM, Morcrette JJ, Park BK, Peubey C, de Rosnay P, Tavolato C, Thépaut JN, Vitart F (2011) The ERA-interim reanalysis: configuration and performance of the data assimilation system. *Q J R Meteorol Soc* 137(656):553–597. <https://doi.org/10.1002/qj.828>
- Taylor EK (2001) Summarizing multiple aspects of model performance in a single diagram. *J Geophys Res* 106:7183–7192. <https://doi.org/10.1029/2000JD900719>
- ECMWF (2018) Part VII : ECMWF Wave Model, ECMWF, chap 10, p 70. No. 7 in IFS Documentation, <https://www.ecmwf.int/node/18717>
- EMODnet (2016) Emodnet digital bathymetry (dtm). Marine Information Service. <https://doi.org/10.12770/c7b53704-999d-4721-b1a3-04ec60c87238>
- FUGRO (2012) Seawatch wavescan buoy. Brochure, <https://www.fugro.com/docs/default-source/about-fugro-doc/ROVs/seawatch-wavescan-buoy-flyer.eps>
- Furevik BR, Haakenstad H (2012) Near-surface marine wind profiles from rawinsonde and NORA10 hindcast. *Journal of Geophysical Research: Atmospheres* 117(D23). <https://doi.org/10.1029/2012JD018523>
- Galanis G, Kallos G, Chu P, Kuo YH (2019) Evaluation of the new ECMWF WAM model. European Space Agency, Proc of “SeaSar 2010”, Frascati, Italy, 25–29 January 2010
- Gelaro R, McCarty W, Suárez MJ, Todling R, Molod A, Takacs L, Randles CA, Darmenov A, Bosilovich MG, Reichle R, Wargan K, Coy L, Cullather R, Draper C, Akella S, Buchard V, Conaty A, da Silva AM, Gu W, Kim GK, Koster R, Lucchesi R, Merkova D, Nielsen JE, Partyka G, Pawson S, Putman W, Rienecker M, Schubert SD, Sienkiewicz M, Zhao B (2017) The modern-era retrospective analysis for research and applications, version 2 (MERRA-2). *J Clim* 30(14):5419–5454. <https://doi.org/10.1175/JCLI-D-16-0758.1>
- Guedes Soares C, Salvacao N, Gonçalves M, Rusu L (2016) Validation of an operational wave forecasting system for the North Atlantic area. Taylor & Francis Group, London, pp 1037–1043
- Gunther SH, Janssen PAEM (1992) The WAM model cycle 4. Technical report. Deutsches KlimaRechenZentrum, Hamburg, Germany
- Hasselmann K, P Barnett T, Bouws E, Carlson H, E Cartwright D, Enke K, A Ewing J, Gienapp H, E Hasselmann D, Kruseman P, Meerburg A, Muller P, Olbers D, Richter K, Sell W, Walden H (1973) Measurements of wind-wave growth and swell decay during the Joint North Sea Wave Project (JONSWAP). *Deut Hydrogr Z* 8:1–95
- Hersbach H, Dee D (2016) ERA5 reanalysis is in production. ECMWF Newsletter 147:7
- Janssen PA (2008) Progress in ocean wave forecasting. *J Comput Phys* 227(7):3572–3594. <https://doi.org/10.1016/j.jcp.2007.04.029>, <http://www.sciencedirect.com/science/article/pii/S0021999107001659>, predicting weather, climate and extreme events
- Janssen PA, Bidlot JR (2018) Progress in operational wave forecasting. *Procedia IUTAM* 26:14–29. <https://doi.org/10.1016/j.piutam.2018.03.003>, <http://www.sciencedirect.com/science/article/pii/S2210983818300038>, iUTAM Symposium on Wind Waves
- Komen G, Hasselmann K (1984) On the existence of a fully developed wind-sea spectrum. *J Phys Oceanogr - J Phys Oceanogr* 14:1271–1285. [https://doi.org/10.1175/1520-0485\(1984\)014<1271:OTEOAF>2.0.CO;2](https://doi.org/10.1175/1520-0485(1984)014<1271:OTEOAF>2.0.CO;2)
- Lalouaux P, de Boisseson E, Balmaseda M, Bidlot JR, Broennimann S, Buizza R, Dalhgren P, Dee D, Haimberger L, Hersbach H, Kosaka Y, Martin M, Poli P, Rayner N, Rustemeier E, Schepers D (2018) CERA-20C: A Coupled Reanalysis of the Twentieth Century. *J Adv Model Earth Syst* 10(5):1172–1195. <https://doi.org/10.1029/2018MS001273>
- Lavidas G, Venugopal V, Friedrich D (2017) Sensitivity of a numerical wave model on wind re-analysis datasets. *Dyn Atmos Oceans* 77:1–16. <https://doi.org/10.1016/j.dynatmoce.2016.10.007>, <http://www.sciencedirect.com/science/article/pii/S0377026516301154>
- Mao M, van der Westhuysen AJ, Xia M, Schwab DJ, Chawla A (2016) Modeling wind waves from deep to shallow waters in lake michigan using unstructured swan. *J Geophys Res: Oceans* 121(6):3836–3865. <https://doi.org/10.1002/2015JC011340>
- Martínez-Asensio A, Marcos M, Jordà G, Gomis Bosch D (2013) Calibration of a new wind-wave hindcast in the western Mediterranean. *Journal of Marine Systems*. <https://doi.org/10.1016/j.jmarsys.2013.04.006>
- Moeini M, Etemad-Shahidi A, Chegini V (2010) Wave modeling and extreme value analysis off the northern coast of the persian gulf.

- Appl Ocean Res 32(2):209–218. <https://doi.org/10.1016/j.apor.2009.10.005>
- Müller M, Homleid M, Ivarsson KI, Køltzow MAØ, Lindskog M, Midtbø KH, Andrae U, Aspeli T, Berggren L, Bjørge D, Dahlgren P, Kristiansen J, Randriamampianina R, Ridal M, Vignes O (2017) AROME-MetCoOp: a nordic convective-scale operational weather prediction model. *Weather Forecast* 32(2):609–627. <https://doi.org/10.1175/WAF-D-16-0099.1>
- Olauson J (2018) ERA5: The new champion of wind power modelling? *Renewable Energy* 126. <https://doi.org/10.1016/j.renene.2018.03.056>
- Olsen AM, Granerød M (2017) Ekstremværapport, hendelse: Urd 26 desember 2016. Technical report, Norwegian Meteorological Institute
- Poli P, Hersbach H, Dee D, Berrisford P, Simmons A, Vitart F, Lalouaux P, Tan D, Peubey C, Thepaut JN, Trémolet Y, Hólm E, Bonavita M, Isaksen L, Fisher M (2016) ERA-20C: An Atmospheric Reanalysis of the Twentieth Century. *J Clim* 29(11):4083–4097. <https://doi.org/10.1175/JCLI-D-15-0556.1>
- Ponce de León S, Orfila A, Gómez-Pujol L, Renault L, Vizoso G, Tintoré J (2012) Assessment of wind models around the balearic islands for operational wave forecast. *Appl Ocean Res* 34:1–9. <https://doi.org/10.1016/j.apor.2011.09.001>, <http://www.sciencedirect.com/science/article/pii/S0141118711000770>
- Reistad M, Breivik Ø, Haakenstad H, Aarnes OJ, Furevik BR, Bidlot JR (2011) A high-resolution hindcast of wind and waves for the North Sea, the Norwegian Sea, and the Barents Sea. *Journal of Geophysical Research: Oceans* 116(C5). <https://doi.org/10.1029/2010JC006402>
- Saha S, Moorthi S, Pan HL, Wu X, Wang J, Nadiga S, Tripp P, Kistler R, Woollen 846 J, Behringer D, Liu H, Stokes D, Grumbine R, Gayno G, Wang J, Hou YT, 847 Chuang HY, Juang HMH, Sela J, Iredell M, Treadon R, Kleist D, Delst PV, 848 Keysler D, Derber J, Ek M, Meng J, Wei H, Yang R, Lord S, Van den Dool H, KumarV, Wang W, Long C, Chelliah M, Xue Y, Huang B, Schemm JK, Ebisuzaki W, Lin R, Xie P, Chen M, Zhou S, Higgins W, Zou CZ, Liu Q, Chen Y, Han Y, Cucurull L, Reynolds RW, Rutledge G, Goldberg M (2010) NCEP Cli852 mate Forecast System Reanalysis (CFSR) selected hourly time-series products 853 January 1979 to. <https://doi.org/10.5065/D6513W89>
- Semedo A, Vettor R, Breivik Ø, Sterl A, Reistad M, Soares CG, Lima DCA (2015) The wind sea and swell waves climate in the Nordic Seas. *Ocean Dyn* 65(2):223–240. <https://doi.org/10.1007/s10236-014-0788-4>
- Signell RP, Carniel S, Cavaleri L, Chiggiato J, Doyle JD, Pullen J, Selavo M (2005) Assessment of wind quality for oceanographic modelling in semi-enclosed basins. *J Mar Syst* 53(1):217–233. <https://doi.org/10.1016/j.jmarsys.2004.03.006>
- Skamarock WC, Klemp JB, Dudhia J, Gill DO, Barker M, Duda KG, Huang XY, Wang W, Powers JG (2008) A description of the Advanced Research WRF Version 3. Technical report, National Center for Atmospheric Research
- Stopa JE, Cheung KF (2014) Intercomparison of wind and wave data from the ECMWF Reanalysis Interim and the NCEP climate forecast system reanalysis. *Ocean Modell* 75:65–83. <https://doi.org/10.1016/j.ocemod.2013.12.006>, <http://www.sciencedirect.com/science/article/pii/S1463500313002205>
- SWAN team (2019) Modifications. <http://swanmodel.sourceforge.net/modifications/modifications.htm>
- The Norwegian Coastal Administration (2019a) Map service: Kystinfo. <https://kart.kystverket.no/>
- The Norwegian Meteorological Institute (2019b) Observational data at SVV-E39 project. <http://thredds.met.no/thredds/catalog/obs/buoy-svv-e39/catalog.html>
- The Wamdi Group (1988) The WAM model - a third generation ocean wave prediction model. *J Phys Oceanogr* 18(12):1775–1810. [https://doi.org/10.1175/1520-0485\(1988\)018<1775:TWMGTGO>2.0.CO;2](https://doi.org/10.1175/1520-0485(1988)018<1775:TWMGTGO>2.0.CO;2)
- The WAVEWATCHIII® Development Group (2016) User manual and system documentation of WAVEWATCH III® version 5.16. Tech. Note 329, NOAA/NWS/NCEP/MMAB, 326 pp. + Appendices
- Troen I, Lundtang Petersen E (1989) European Wind Atlas. Risø National Laboratory
- Tuomi L (2014a) On modelling surface waves and vertical mixing in the baltic sea. PhD thesis, University of Helsinki, Faculty of Science, Department of Physics, Finnish Meteorological Institute, <http://hdl.handle.net/10138/42773>
- Tuomi L, Pettersson H, Fortelius C, Tikka K, Björkqvist JV, Kahma KK (2014b) Wave modelling in archipelagos, vol 83. <https://doi.org/10.1016/j.coastaleng.2013.10.011>, <http://www.sciencedirect.com/science/article/pii/S0378383913001671>
- Undén P, Rontu L, Järvinen H, Lynch P, Calvo-Sanchez J, Cats G, Cuxart J, Eerola K, Fortelius C, García-Moya J (2002) HIRLAM-5 Scientific documentation. Technical report, Sveriges meteorologiska och hydrologiska institut
- Uppala S, Kallberg P, Simmons A, Andrae U, Da Costa Bechtold V, Fiorino M, K Gibson J, Haseler J, Hernandez-Carrascal A, Kelly G, Li X, Onogi K, Saarinen S, Sokka N, Allan R, Andersson E, Arpe K, Balsameda M, Beljaars A, Woollen J (2005) The Era-40 re-analysis. *Q J R Meteorol Soc* 131:2961–3012. <https://doi.org/10.1256/qj.04.176>
- Varlas G, Christakos K, Cheliotis I, Papadopoulos A, Steeneveld GJ (2017) Spatiotemporal variability of marine renewable energy resources in Norway. *Energy Procedia* 125:180–189. <https://doi.org/10.1016/j.egypro.2017.08.171>
- Vignudelli S, Kostianoy A, Cipollini P, Benveniste J (2011) Coastal Altimetry. Springer, vol 1. <https://doi.org/10.1007/978-3-642-12796-0>
- Wang J, Li L, Jakobsen JB, Haver SK (2018) Metocean conditions in a Norwegian fjord. *Journal of Offshore Mechanics and Arctic Engineering*. <https://doi.org/10.1115/1.4041534>
- van der Westhuysen AJ, Zijlema M, Battjes JA (2007) Nonlinear saturation-based whitecapping dissipation in SWAN for deep and shallow water. *Coast Eng* 54(2):151–170. <https://doi.org/10.1016/j.coastaleng.2006.08.006>, <http://www.sciencedirect.com/science/article/pii/S037838390600127X>
- Wieringa J (1992) Updating the davenport roughness classification. *J Wind Eng Ind Aerodyn* 41(1):357–368. [https://doi.org/10.1016/0167-6105\(92\)90434-C](https://doi.org/10.1016/0167-6105(92)90434-C), <http://www.sciencedirect.com/science/article/pii/016761059290434C>
- Yan L (1987) An improved wind input source term for third generation ocean wave modelling. Rep No 87-8, Royal Dutch Meteor Inst



# Paper II

## **Modelling wave growth in narrow fetch geometries: The white-capping and wind input formulations**

Christakos, K., J.V. Björkqvist, L. Tuomi, B.R. Furevik, and Ø. Breivik (2021), *Ocean Modelling*, 157, 101730.





# Modelling wave growth in narrow fetch geometries: The white-capping and wind input formulations

Konstantinos Christakos<sup>a,b,c,\*</sup>, Jan-Victor Björkqvist<sup>c</sup>, Laura Tuomi<sup>c</sup>, Birgitte R. Furevik<sup>a</sup>, Øyvind Breivik<sup>a,b</sup>

<sup>a</sup> Norwegian Meteorological Institute, Allégaten 70, 5007 Bergen, Norway

<sup>b</sup> Geophysical Institute, University of Bergen, Allégaten 70, 5007 Bergen, Norway

<sup>c</sup> Finnish Meteorological Institute, Erik Palménin aukio 1, 00560 Helsinki, Finland

## ARTICLE INFO

### Keywords:

Waves  
White-capping  
Wind  
Swell  
Fjord  
ST6  
SWAN

## ABSTRACT

This paper investigates the performance of three different wave model source term packages in narrow fetch geometries. The packages are used to model the sea state in a complex coastal system with narrow fjords on the west coast of Norway. The modelling system is based on the Simulating WAVes Nearshore (SWAN) wave model that is forced with winds from a nested atmospheric model and wave spectra from a regional wave model at the boundaries. The performances of the recent ST6, and two older SWAN white-capping and wind input packages, are evaluated by comparing modelled spectra and integrated wave parameters against five wave buoys. The comparison covers long-term statistics and two case studies of narrow fetch geometries (i) without swell and (ii) with swell-wind sea conditions. SWAN's original saturation-based approach performs best in the fjord system. In narrow fetch geometry without swell, all packages overestimate the wave energy. ST6 shows the highest sensitivity to fetch geometry and local wind changes. The results indicate that the ST6 white-capping is too weak to balance its strong wind input.

## 1. Introduction

The development of infrastructure in coastal areas demands accurate information of environmental conditions, such as winds and waves. Knowledge of the local wave climate is essential for a number of marine activities, e.g., aquaculture, and maritime and energy applications. However, the need for long-term wave statistics with high spatial and temporal resolution cannot be fulfilled with measurements alone. Thus, numerical simulations are essential to fill these gaps. The accuracy of wave model predictions has been significantly improved in recent years (e.g. Cavaleri et al., 2018, 2020). Several hindcast and reanalysis datasets have shown good quality in offshore conditions (e.g. for the North Atlantic (Reistad et al., 2011; Haakenstad et al., 2020) and the North Sea (Lavidas and Polinder, 2019)). These advances are mainly due to improved source term formulations and more accurate wind fields from atmospheric models (Cavaleri et al., 2018).

The wave field estimates in coastal and semi-enclosed areas are less accurate than offshore because of islands, shallow waters, tides, tidal currents, and complex orography that affects the quality of the wind forcing. As discussed in several studies (e.g. Cavaleri and Bertotti, 2004; Ardhuin et al., 2007; Pallares et al., 2014), the orography affects the quality of local wind field estimates and in turn also the wave field

estimates. In complex coastal areas, such as in fjord systems, a high resolution atmospheric model can capture orographically steered wind that determines local wave growth (Christakos et al., 2020a). The quality of the lateral boundary wave conditions has a major impact on wave predictions in exposed shores. Christakos et al. (2020a) performed wave model simulations with and without wind forcing in a fjord system exposed to the open ocean. The simulations (excluding the extreme cases) showed quite similar results in the outermost fjord locations, illustrating the dominant role of boundary wave conditions over the locally generated wind sea. For coastal applications, there is also a need for a high-resolution bathymetry. Inaccuracies in bathymetric data can affect processes such as dissipation due to bottom friction and depth-induced wave breaking, both of which are often a central part of the performance of nearshore wave models.

Roland et al. (2014) suggested a list of factors that affect the quality of modelled significant wave height. They found that the second most important factor – right after the accuracy of forcing fields – is the source term formulations. The source terms are empirical approximations of the processes that contribute to wind-wave growth, decay and spectral evolution. In the case of wind-generated waves in deep water the source terms are wind input, wave dissipation and resonant nonlinear wave-wave interaction.

\* Corresponding author at: Norwegian Meteorological Institute, Allégaten 70, 5007 Bergen, Norway.  
E-mail address: [konstantinos.christakos@met.no](mailto:konstantinos.christakos@met.no) (K. Christakos).

What we will refer to as the Komen approach to parameterize white-capping dissipation is widely applied and well established in wave modelling. It is based on the pressure-pulse model of Hasselmann (1974), which was parameterized for wave models by Komen et al. (1984). It is the default method in SWAN (Booij et al., 1999), WAM (The Wamdi Group, 1988) and MIKE21-SW (DHI, 2017), and it is an option in WAVEWATCH III (The WAVEWATCH III® Development Group, 2016) and TOMAWAC (Benoit et al., 1997; TOMAWAC, 2020). In this approach the white-capping dissipation is a function of the mean wavenumber and steepness. In mixed wind sea-swell conditions the Komen approach dissipates more swell energy than in cases with no wind, while also overestimating the wind-sea height in the presence of swell because of its dependency on the mean wavenumber and steepness (see van der Westhuysen et al., 2007, and references therein).

An alternative, saturation-based approach, was introduced by Alves and Banner (2003) and developed further by van der Westhuysen et al. (2007). This approach removes the dependency on mean spectral steepness by instead employing the local spectral saturation. van der Westhuysen et al. (2007) showed that modelling wave dissipation using a local saturation gave better results in mixed wind sea-swell conditions than Komen's approach. This saturation-based approach has also been incorporated in spectral wave models such as SWAN and TOMAWAC.

In recent years, new developments in white-capping and wind input formulations (known as ST4 Arduin et al., 2010 and ST6 Babanin et al., 2010) have been implemented, mainly in WAVEWATCH III, but also in SWAN (for ST6). Compared to older approaches, these formulations are more sophisticated and include newer features, such as negative wind input and swell dissipation. They also have a high number of tuning options, thus allowing more advanced calibration.

The performance of ST6 for open sea conditions has been reported in several works. van Vledder et al. (2016) studied the wave conditions during a severe storm in the southern North Sea. They concluded that the ST6 package gave the best model performance in terms of the spectral shape and several integrated wave parameters, including the significant wave height and the spectral period  $T_{m-1.0}$ . Rogers et al. (2012), Zieger et al. (2015), Stopa et al. (2015), Liu et al. (2019) and Lavidas and Polinder (2019) have tested the ST6 source terms across a large number of idealized and real-world applications. However, the new parameterization has not been extensively tested in coastal areas. Amarouche et al. (2019) evaluated ST6 and a combination of white-capping formula by Janssen (1991) and exponential wind growth by Komen et al. (1984) in the western Mediterranean Sea. They advised the use of a calibrated version of the latter combination due to its better performance and shorter simulation period. However, in Norwegian fjord areas, Stefanakos et al. (2020) found that the wind input and white-capping of Janssen (1991) systematically overestimates the wave heights.

Our overall objective is to find appropriate source term formulations in SWAN for white-capping and wind input under narrow-fetch conditions in semi-sheltered seas. The location of our investigation is a fjord system (Fig. 1) on the west coast of Norway, which serves as an excellent example of narrow-fetch geometry in the presence of strong wind forcing. The wave climate on the west coast of Norway is characterized by strong swell from the North Atlantic Ocean (Semedo et al., 2014; Christakos et al., 2020b) and frequent passages of extratropical systems. In addition, coastal phenomena – such as low level jets (Christakos et al., 2014) and wind channelling (Christakos et al., 2020a) induced by topography – also affect the local wind sea, creating a mixed sea state of wind sea and swell. The narrow fetch in itself also affects the growth of the waves (Pettersson, 2004). We base our assessment of the source terms on both long-term statistics and two cases of narrow fetch geometries with: (i) no swell and (ii) mixed wind sea-swell. Three different formulations for white-capping and wind input are evaluated against in situ measurements. Special attention is given to analysis of the different source terms related to the fetch geometry. This is, to our knowledge, the first paper that studies the effect of the narrow fetch geometry on the performance of source term packages in different sea states.

The paper is organized as follows: Section 2 describes the modelling system, followed by Section 3, which describes the data and the methods employed. In Section 4 we present the overall model performance and selected case studies. Section 5 discusses our results. In Section 6, we end by summarizing and concluding our findings.

## 2. Description of the modelling system

The study area (Fig. 1) is described in Christakos et al. (2020a). In Sulafjorden buoys A, B, C, and D (Breidsundet) are deployed, and buoy F in the fjord cross-section of Vartdalsfjorden, Voldsfjorden, and Rovdefjorden, as shown in Fig. 1. Sulafjorden is approximately 10 km long with an average width of 4.6 km. Because of its exposure to the Norwegian Sea, the wave climate in Sulafjorden is usually characterized by mixed wind sea and swell conditions, while the inner parts of the fjord system, such as location F, are unaffected by swell. The fjords are 200–700 m deep, much deeper than the shelf area which is less than 100 m over most areas. In storm conditions, wave dissipation due to bottom friction and depth-induced wave breaking occurs off the coast in shallow/transitional waters, before reaching the fjord system.

### 2.1. The wave model: SWAN

The wave model SWAN is a third generation spectral model mainly developed for nearshore applications. The SWAN wave model is also capable of reproducing fjord wave conditions (Christakos et al., 2020a; Herman et al., 2019). In this study the SWAN cycle III version 41.20 is used. As a spectral model, it estimates the evolution of wave action density  $N = E/\sigma$  by applying the action balance equation,

$$\frac{\partial N}{\partial t} + \frac{\partial(c_x N)}{\partial x} + \frac{\partial(c_y N)}{\partial y} + \frac{\partial(c_\sigma N)}{\partial \sigma} + \frac{\partial(c_\theta N)}{\partial \theta} = \frac{S}{\sigma}. \quad (1)$$

Here,  $E$  is the wave spectral energy,  $\sigma$  the intrinsic circular frequency (in absence of a surface current,  $\sigma = \omega = 2\pi f[\text{rad s}^{-1}]$ , where  $f$  is the linear frequency [Hz]), and  $c_x$  and  $c_y$  are the group velocity vector components in geographical  $(x, y)$ -space. The  $c_\sigma$  and  $c_\theta$  represent the propagation in frequency-direction  $(\sigma, \theta)$  space. The term  $S$  represents the total source term, consisting of in all six source terms in SWAN,

$$S = S_{\text{in}} + S_{\text{ds}} + S_{\text{nl4}} + S_{\text{nl3}} + S_{\text{fric}} + S_{\text{brk}}. \quad (2)$$

Here,  $S_{\text{in}}$  is the energy input by wind,  $S_{\text{ds}}$  is the dissipation induced by white-capping,  $S_{\text{nl4}}$  is the nonlinear wave energy transfer between quadruplets,  $S_{\text{nl3}}$  is the triad nonlinear interaction,  $S_{\text{fric}}$  is the bottom friction, and  $S_{\text{brk}}$  is the depth-induced wave breaking (e.g. Holthuijsen, 2007). Since our study is focused on relatively deep water areas, the term for triads is switched off. The wind input term contains a linear and an exponential growth term. A sensitivity study (not shown) found that the linear term had only a minor effect on wave growth and is therefore neglected. For our fjord applications, we therefore focused on  $S_{\text{in}}$ ,  $S_{\text{ds}}$ , and  $S_{\text{nl4}}$ .

#### 2.1.1. The KOMEN package

In SWAN, the current default white-capping dissipation is the pressure pulse model of Hasselmann (1974), formulated by Komen et al. (1984) and defined as (e.g. SWAN team, 2017),

$$S_{\text{ds,KOMEN}}(\sigma, \theta) = -C_{\text{ds,KOMEN}} \left( (1 - \delta) + \delta \frac{k}{k} \right) \left( \frac{\bar{S}}{\bar{S}_{\text{PM}}} \right)^p \bar{\sigma} \frac{k}{k} E(\sigma, \theta). \quad (3)$$

Here  $C_{\text{ds,KOMEN}} (=0.24 \times 10^{-4})$ ,  $\delta (=1)$ , and  $p (=4)$  are tuning parameters,  $k$  is the wavenumber, and  $\bar{S} = \bar{k} \sqrt{E_{\text{tot}}}$  is the mean spectral steepness.  $E_{\text{tot}}$  is the total energy of the wave spectrum, i.e., the integral over all frequencies and directions. The  $\bar{k}$  and  $\bar{\sigma}$  are the mean wavenumber and the mean circular frequency. The  $\bar{S}_{\text{PM}}$  corresponds to the mean spectral steepness of a Pierson–Moskowitz spectrum. A study by Rogers et al. (2003) showed that  $\delta = 1$  (the default value in SWAN

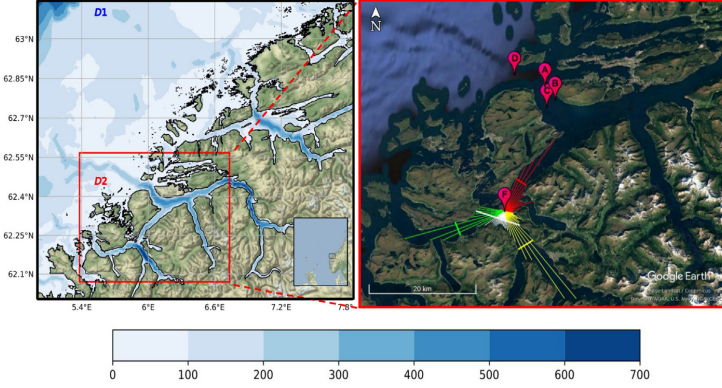


Fig. 1. Left: The model domains on the west coast of Norway: the outer (D1) with a grid resolution of  $1000 \text{ m} \times 1000 \text{ m}$  and the inner domain (D2, red rectangular) with a  $250 \text{ m} \times 250 \text{ m}$  resolution. The colour represents the water depth in metres. Right: Inner domain with location of buoys D, A, B, C, and F. Illustration of fetches (distances between shore and buoy) with 5 degree resolution and the corresponding widths (same colour with fetch) at location F.

41.20) improves the wave energy estimates over  $\delta = 0.5$  proposed by Komen et al. (1994).

The wind input term is estimated according to Komen et al. (1984), which in turn is based on experimental results by Snyder et al. (1981),

$$S_{\text{in,SNYDER}}(\sigma, \theta) = \max \left[ 0, 0.25 \frac{\rho_a}{\rho_w} \left( 28 \frac{u_*}{c} \cos(\theta - \theta_w) - 1 \right) \right] \sigma E(\sigma, \theta). \quad (4)$$

Here,  $u_* = \sqrt{\tau/\rho_a}$  (where  $\tau$  is the wind stress) is the friction velocity. The estimation of  $u_*$  is made according to Zijlema et al. (2012).  $c$  is the phase speed of the wave component, and  $\rho_a$  and  $\rho_w$  are the air and water densities, respectively. The direction of the spectral wave component is  $\theta$ , and  $\theta_w$  is the direction of the wind. This white-capping/wind input package will hereafter be denoted KOMEN. Eq. (4) is based on field observations of weakly forced waves, where  $U_5$  (the wind speed at 5 m height) had values up to  $8 \text{ m s}^{-1}$  (Snyder et al., 1981). For wind speed ranges of  $2\text{--}12 \text{ m s}^{-1}$ , Hasselmann and Bösenberg (1991) came up with similar results to Snyder et al. (1981). Thus, we consider Eq. (4) appropriate for weak to moderate wind conditions, but its validity is not proven for strong wind events.

### 2.1.2. The WESTH package

As an alternative to the Komen approach, van der Westhuysen et al. (2007) modified the saturation-based method of Alves and Banner (2003) and implemented it in SWAN. In contrast to the approach taken by Komen et al. (1984), this method expresses white-capping without the  $\bar{S}$  and  $\bar{k}$  dependencies, which are problematic in mixed wind sea and swell conditions. This method is based on experimental results showing that white-capping is associated with the nonlinear hydrodynamics within wave groups. The formulation reads:

$$S_{\text{break,WESTH}}(\sigma, \theta) = -C_{\text{ds,WESTH}} \left( \frac{B(k)}{B_r} \right)^{p'/2} \left[ \tanh(kd) \right]^{\frac{2-p_0}{4}} \sqrt{gk} E(\sigma, \theta). \quad (5)$$

Here,  $C_{\text{ds,WESTH}}$  ( $=0.50 \times 10^{-4}$ ) is the white-capping parameter,  $d$  is the water depth,  $g$  is the acceleration due to gravity, and  $B(k) = E(\sigma)k^3 c_g$  ( $c_g$  is the wave group velocity) is the azimuthally integrated spectral saturation. The latter is well correlated with the breaking probability (Banner et al., 2002). When  $B(k)$  is below the threshold saturation level ( $B_r = 1.75 \times 10^{-3}$ ) there is no breaking, but a background dissipation of wave component is present with  $p' = 0$ . When  $B(k)$  exceeds  $B_r$ , there is wave breaking and  $p'$  equals a calibration exponent  $p_0$ . To give a smooth transition between these two conditions,  $p'$  is expressed as function of  $B(k)$  (Alves and Banner, 2003).

The dissipation is separated into a breaking and a non-breaking part (SWAN team, 2017):

$$S_{\text{ds,WESTH}}(\sigma, \theta) = f_{\text{br}}(\sigma) S_{\text{break,WESTH}} + (1 - f_{\text{br}}(\sigma)) S_{\text{ds,non-break}}. \quad (6)$$

The  $S_{\text{ds,non-break}}$  term is expressed by Eq. (3). Similar to the parameter  $p'$ ,  $f_{\text{br}}$  is a smooth transition function (SWAN team, 2017).

The wind input applied in the saturation-based parameterization is according to Yan (1987), which combines the expressions by Komen et al. (1984) and Plant (1982),

$$S_{\text{in,YAN}}(\sigma, \theta) = \left\{ \left[ C_1 \left( \frac{u_*}{c} \right)^2 + C_2 \left( \frac{u_*}{c} \right) + C_3 \right] \cos(\theta - \theta_w) + C_4 \right\} \sigma E(\sigma, \theta). \quad (7)$$

where  $C_1 = 4 \times 10^{-2}$ ,  $C_2 = 5.52 \times 10^{-3}$ ,  $C_3 = 5.2 \times 10^{-5}$ ,  $C_4 = -3.02 \times 10^{-4}$  are coefficients (given by SWAN team (2017)). For strong wind conditions, i.e., young wind sea ( $u_*/c > 0.1$ ), the wave growth rate has a quadratic relation to the inverse wave age ( $u_*/c$ ). For weaker winds, i.e., older sea ( $u_*/c < 0.1$ ), the relation becomes linear. Similar to KOMEN, the estimation of  $u_*$  is according to Zijlema et al. (2012). This package is activated in the SWAN model with the command GEN3 WESTH and is hereafter denoted WESTH.

### 2.1.3. The ST6 package

ST6 is a recent formulation included in SWAN version 41.20. The package is also implemented in WAVEWATCH III, as documented by Zieger et al. (2015). The ST6 implementation in SWAN has only minor differences to that of WAVEWATCH III (Rogers et al., 2012; SWAN team, 2017). ST6 is an observation-based scheme that contains wave-turbulence interaction (swell decay), positive and negative wind input, and two-phase white-capping dissipation.

The wind input formulation is given as

$$S_{\text{in,ST6}}(\sigma, \theta) = \frac{\rho_a}{\rho_w} \sigma G \sqrt{B_n} W E(\sigma, \theta), \quad (8)$$

where

$$G = 2.8 - [1 + \tanh(10\sqrt{B_n}W - 11)]. \quad (9)$$

Here,  $B_n = A(\sigma)E(\sigma)k^3 c_g$  is the spectral saturation (a measure of steepness), and  $A$  is the narrowness of the directional distribution. The narrowness is defined as  $A^{-1} = \int_0^{2\pi} \frac{E(\sigma, \theta)}{E_{\text{max}}(\sigma)} d\theta$ , where  $E_{\text{max}}(\sigma)$  is the maximum density over all directions, but  $A$  is set to unity for dissipation calculations in SWAN.

In addition to the positive wind input, ST6 also allows a negative wind input component that reduces wave growth in the part of the spectrum that experiences adverse wind stress. This is formulated as

$$W(\sigma, \theta) = W_1(\sigma, \theta) - a_0 W_2(\sigma, \theta), \quad (10)$$

where  $W$  is expressed as the sum of the positive wind input

$$W_1(\sigma, \theta) = \max^2 \left\{ 0, s_{ws} \frac{u_w}{c} \cos(\theta - \theta_w) - 1 \right\} \quad (11)$$

and the adverse (negative) wind input,

$$W_2(\sigma, \theta) = \min^2 \left\{ 0, s_{ws} \frac{u_w}{c} \cos(\theta - \theta_w) - 1 \right\}. \quad (12)$$

Here  $a_0$  is a tuning parameter and  $s_{ws}$  is a scaling parameter, which is set to 32 in SWAN 41.20.

There are three available formulations in ST6 for the estimation of  $u_w = \sqrt{C_D} U_{10}$  (where  $C_D$  is the drag coefficient) in the wave model. Following the SWAN notation, the formulations are: HWANG (default) (Rogers et al., 2012), FAN (Fan et al., 2012), and ECMWF (Guenther et al., 1992). In the HWANG formulation, the drag coefficient is only a function of wind speed. On the other hand, FAN and ECMWF use an iterative procedure for estimating  $u_w$  based on the actual seas state. In FAN formula,  $u_w$  is a function of both wave age and wind speed whereas in ECMWF it is a function of air flow and wave-induced stress.

The white-capping term  $S_{ds,ST6}$  is the sum of two dissipation components  $T_1$  and  $T_2$  (e.g. Rogers et al., 2012). The component  $T_1$  is the inherent breaking related to instabilities of waves and  $T_2$  is a cumulative term that describes the dissipation of shorter waves triggered by longer breaking waves,

$$S_{ds,ST6}(\sigma, \theta) = \left[ T_1(\sigma) + T_2(\sigma) \right] E(\sigma, \theta). \quad (13)$$

Here,

$$T_1(\sigma) = a_1 A(\sigma) \frac{\sigma}{2\pi} \left[ \frac{E(\sigma) - E_T(\sigma)}{E_T(\sigma)} \right]^{p_1} \quad (14)$$

and

$$T_2(\sigma) = a_2 \int_{\sigma_1}^{\sigma} \frac{A(\sigma')}{2\pi} \left[ \frac{E(\sigma') - E_T(\sigma')}{E_T(\sigma')} \right]^{p_2} d\sigma', \quad (15)$$

The threshold spectral density is  $E_T = \frac{B_{nl}}{A(\sigma) \epsilon_g k^3}$ , where  $B_{nl}$ ,  $a_1$  and  $a_2$  are constants.  $p_1 (=4)$  and  $p_2 (=4)$  are power coefficients and  $\sigma_1$  is the first prognostic frequency. A key feature of the ST6 formulation is that there is no breaking unless the spectral energy density at that particular frequency ( $\sigma$ ) exceeds the threshold  $E_T(\sigma)$ .

#### 2.1.4. Wave-wave interactions, bottom friction, and depth-limited breaking

The four-wave interactions (quadruplet) are modelled by the discrete interaction approximation (DIA) by Hasselmann et al. (1985). Nonlinear triad interaction is turned off since their effect is minor in our (deep-water) area of interest. The bottom friction is represented by the JONSWAP bottom friction (Hasselmann et al., 1973) (where  $C_{fric} = 0.067 \text{ m}^2 \text{ s}^{-3}$  is the bottom friction coefficient according to Bouws and Komen (1983)). Finally, the depth-limited wave breaking is represented by the formulation of Battjes and Janssen (1978) with default settings of  $\alpha = 1$  and  $\gamma = 0.73$ .

### 3. Data and methods

The model was run in non-stationary mode with spherical coordinates and a time step of 10 min (with 4 iterations of the implicit scheme). The spectrum is resolved by 36 directional bins ( $10^\circ$  directional resolution) and 32 logarithmically spaced frequencies from 0.04 to 1 Hz. The inner domain (D2) with a grid resolution of  $250 \text{ m} \times 250 \text{ m}$  (red rectangle in the left panel of Fig. 1) is nested into the outer grid

(D1) of  $1 \text{ km} \times 1 \text{ km}$ . The simulation period is from October 1, 2016 until April 30, 2018.

#### 3.1. Wind forcing

Because of the complex fjord topography, a high resolution wind forcing is essential to faithfully reproduce local wind conditions. Such local features may have a considerable effect on the wave growth in a fjord, as discussed by Christakos et al. (2020a) and Herman et al. (2019). In our study, the Advanced Research WRF (Skamarock et al., 2008) state-of-the-art numerical weather prediction model version 3.5.0 is applied to downscale the reanalysis ERA-Interim (Dee et al., 2011) to a grid resolution of 0.5 km for the fjord system (Christakos et al., 2020a). This downscaled wind product is hereafter called WRF0.5. Christakos et al. (2020a) showed that WRF0.5 slightly overestimated high wind speeds in the innermost locations of our study area, but nevertheless performed better than other available wind products (the ERA5 reanalysis (Hersbach et al., 2020), the hindcast NORA10 (Reistad et al., 2011), and the operational numerical weather prediction model AROME2.5). Wind input to the wave model is linearly interpolated to the SWAN grid from the 10 m height wind of WRF0.5.

#### 3.2. Boundary wave conditions

The wave conditions at the grid boundaries of the outer model domain are obtained from the NORA10 hindcast with 3-hourly temporal resolution (information on the spectral nesting and interpolation in Breivik et al. (2009)). The wave component of NORA10 is a 10 km WAM model forced with winds from the High Resolution Limited Area Model (HIRLAM) nested inside a 50 km North Atlantic WAM model forced by ERA-40 winds (Reistad et al., 2011). The wave component is a modified version of the WAM cycle 4 model (Guenther et al., 1992) set up on a rotated latitude-longitude grid similar to the rotated spherical grid used for HIRLAM. The outer domain covers the North Atlantic with a 50 km grid resolution, thus allowing realistic swell propagation from the North Atlantic to the Norwegian coast. Twenty-four directional bins and twenty-five frequencies (0.0420 to 0.4137 Hz) are used for the NORA10 model setup.

No offshore measurements are available to verify the spectral boundary conditions from NORA10, but several studies have investigated the quality of the NORA10 wave hindcast. According to Aarnes et al. (2012), a low bias of significant wave height between NORA10 and observations located in the North Sea and the Norwegian Sea is observed. Bruserud et al. (2016) found good agreement between NORA10 and wave observations in the northern part of North Sea.

#### 3.3. Measurements

Measurements from SEAWATCH Wavescan buoys (FUGRO, 2012) available via MET Norway's Thredds Service (Furevik et al., 2020) are used to evaluate the performance of the different source term packages. The measurement data contains integrated wave parameters, such as significant wave height, peak wave period, mean wave period, mean wave direction, as well as wind speed and wind direction. In addition, wave spectra are provided for specific storm cases by Fugro OCEANOR AS, Norway. The buoy wind sensors are placed at 4.1 m above the sea level. Buoys D at 345 m water depth, A at 375 m, B at 325 m, C at 450 m, and F at 217 m are deployed in the fjord system, as illustrated in Fig. 1. We used available measurement data from the following periods: October 14, 2016–April 30, 2018 (location D), October 13, 2016–April 30, 2018 (locations A & B), April 27, 2017–April 30, 2018 (location C), and November 29, 2017–April 30, 2018 (location F).

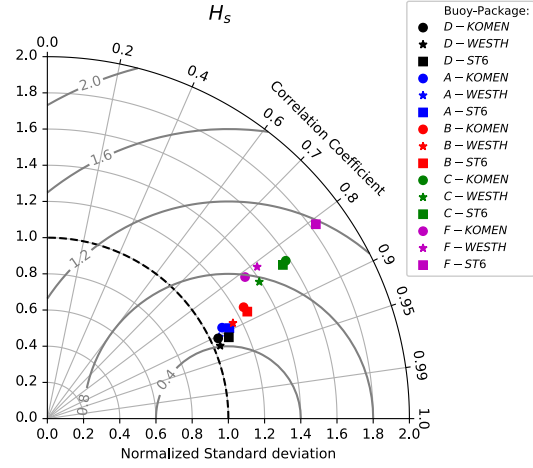


Fig. 2. Taylor diagram for validation of  $H_s$  from different source term packages at locations D, A, B, C, and F. The error metrics: the correlation coefficient (lines), the normalized standard deviation (grey contours), and the centred root mean square error (dark grey contours). Information about the quality of wind forcing (WRF0.5) in Fig. 4 (a) in Christakos et al. (2020a).

### 3.4. Wave and fetch parameters

We analyse the spectral wave parameters of significant wave height  $H_s$ , the mean period  $T_{m01}$ , the peak period  $T_p$ , and mean wave direction  $\theta$ . The model  $T_{m01}$  is calculated by integrating up to maximum observed frequency. We use the logarithmic wind profile to adjust the observed wind speed from 4.1 m to 10 m ( $U_{10}$ ) with a roughness length of 0.0002 m (e.g. Wang et al., 2018; Christakos et al., 2020a).

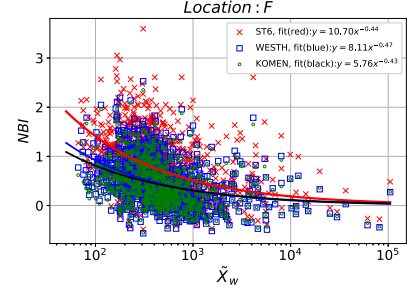


Fig. 4. NBI as a function of dimensionless width at location F.

To investigate how the complex fetch geometry of the fjord system affects the performance of the source term packages, the dimensionless (effective) fetch ( $\tilde{X}$ ) is calculated using the following equations:

$$\tilde{X} = \frac{gX_{eff}}{U_{10}^2} \quad (16)$$

where  $X_{10}$  is the model 10-m wind speed at the buoy location, and  $X_{eff}$  is the effective fetch (estimated in a 30-degree sector with 5 degree increments):

$$X_{eff} = \frac{\sum_{i=0}^6 X_i \cos^2 \phi_i}{\sum_{i=0}^6 \cos \phi_i} \quad (17)$$

Here  $X_i$  is the fetch (in a straight line to the coast) and  $\phi_i$  is the angle from the wind direction in sectors  $i = 0, 1, \dots, 6$ . The dimensionless width is defined as

$$\tilde{X}_w = \frac{gX_w}{U_{10}^2} \quad (18)$$

Here,  $X_w$  is the width (distance across the fetch). The  $\tilde{X}_w$  is quantified because the narrowness of a basin restricts the growth of the wave

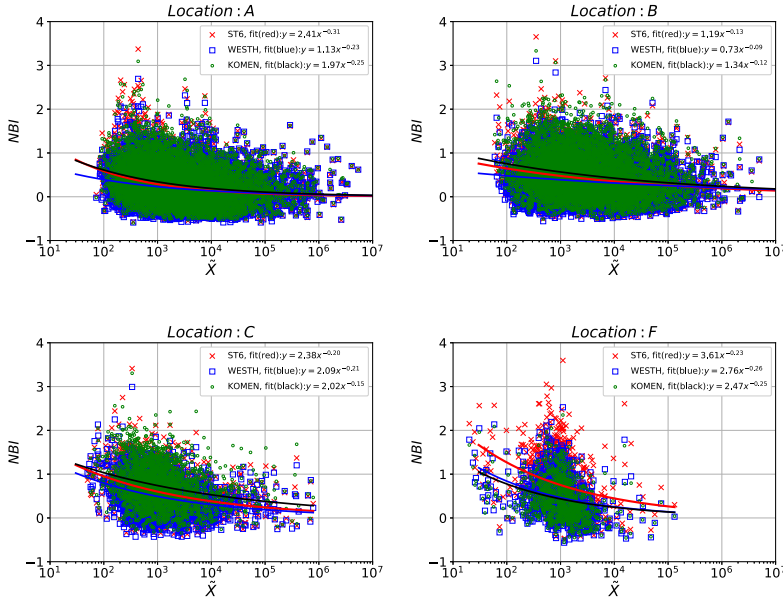


Fig. 3. NBI and dimensionless fetch at locations A, B, C, and F.

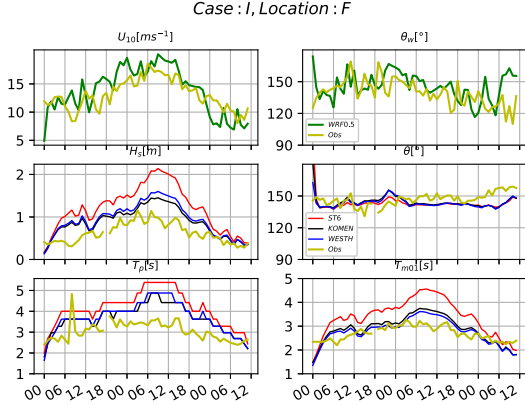


Fig. 5. Time series of wind speed ( $U_{10}$ ), wind direction, significant wave height, mean wave direction, and peak and mean period at location F (case I). Period: January 14, 2018, at 00 UTC to January 16, 2018, at 12 UTC. Obs: Observations.

height even if the fetch is long (Petterson, 2004). The right-hand panel of Fig. 1 shows estimated  $X_l$  and  $X_w$  at location F. Similar estimation is performed for locations D, A, B, and C (not shown) where unlimited fetches are excluded in our study.

Finally, the normalized bias of  $H_s$  is defined as

$$NBI = \frac{H_{s,mod} - H_{s,obs}}{H_{s,obs}} \quad (19)$$

where  $H_{s,mod}$  and  $H_{s,obs}$  are the modelled and observed significant wave height. The use of NBI allows comparisons between areas with different wave climate, e.g., exposed versus sheltered fjord locations. For the estimation of NBI, only  $H_{s,mod}$  and  $H_{s,obs}$  values greater than 0.2 m are considered.

#### 4. Overall model performance and fetch geometry

Taylor diagram of error metrics (Taylor, 2001) for  $H_s$  is illustrated in Fig. 2. The applied error metrics (same definitions as in Christakos et al., 2020a) are the correlation coefficient ( $R$ ), normalized standard deviation (NSTD) and normalized centred root mean square error (CRMSE). The different source term packages show similar performance at the most exposed locations (D and A) with good scores for error metrics, with NSTD close to 1 and  $R$  approximately 0.9. Further into the fjords the model performance degrades ( $0.8 < R < 0.9$  and  $NSTD > 1.1$ ) with the worst performance at locations C and F. WESTH yields the best results in terms of  $H_s$  for most of the measurement locations (D, A, B, and C), while ST6 performs worst in location F.

We plot the NBI as a function of dimensionless fetch to investigate potential over/under-estimation related to the fetch geometry (Fig. 3). In all the measurement locations, the highest overestimation of  $H_s$  is observed at short-medium  $\bar{X}$  and decreases as  $\bar{X}$  increases as a power function. For large  $\bar{X}$ , the different source term packages show near identical results for most of the domain.

In exposed locations (A and B), the performance of the different packages has a weak dependency on  $\bar{X}$  since these areas are affected mainly by strong swell. Only for low  $\bar{X}$ , which are linked to high wind speeds, we observe some dependency. If judged by the fits to the data, all three packages perform similarly for long fetches. For short dimensionless fetches the WESTH package has the lowest NBI, while ST6 and KOMEN coincide. In the slightly more sheltered location C the fits of the WESTH and ST6 packages still agree for the longest fetches, slightly outperforming the KOMEN package. Nonetheless, for short fetches the behaviour at C is similar to that at A and B.

In the most sheltered location (F), NBI depends more strongly on  $\bar{X}$  and we observe the highest NBI difference between the source packages. The wave climate in this location is characterized by no swell and strong local wind sea which is affected, as expected, by the wind structure and the complex fetch geometry. We identify three  $\bar{X}$  ranges: (i) short ( $\bar{X} < 10^2$ ), (ii) medium ( $10^2 \leq \bar{X} \leq 10^4$ ), and (iii) large ( $\bar{X} > 10^4$ ). The short range represents mainly very short fetches ( $X < 5$  km). The medium range (5 km  $\leq X \leq 21$  km with moderate to

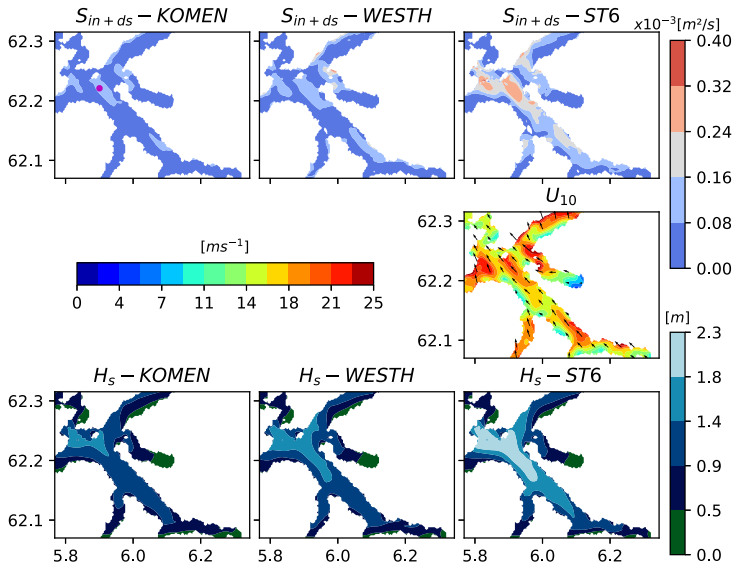


Fig. 6. Snapshot of spatial variation of  $S_{10} + S_{ds}$  (upper),  $U_{10}$  (middle), and  $H_s$  (lower) over the fjord cross-section at location F (marked with dot in the upper left panel) at January 15, 2018, at 09 UTC (case I).

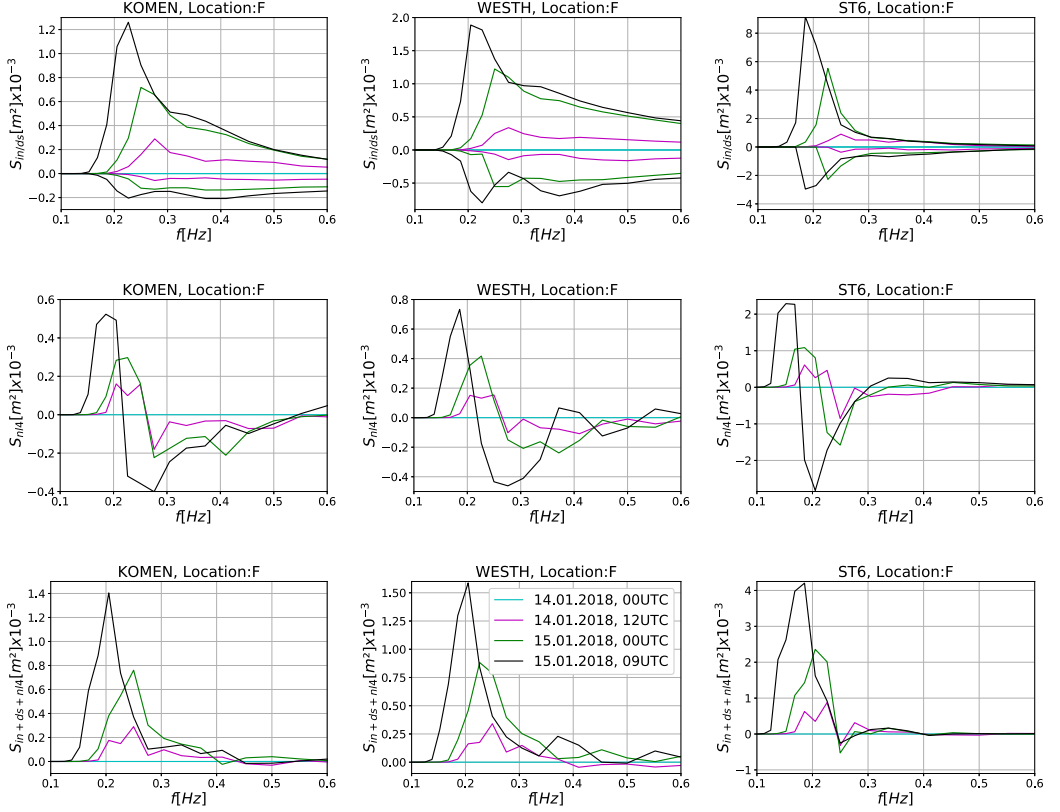


Fig. 7. Evolution of  $S_m$  (positive values in upper panel),  $S_{ds}$  (negative values in upper panel),  $S_{m+ds}$  (middle panel), and their sum  $S_{m+ds+n/d}$  (lower panel) as a function of frequency from January 14, 2018, at 00 UTC (calm conditions) to January 15, 2018, at 09 UTC (peak of wind speed) at location F (case I) for the three source term packages.

strong winds) contains the values with the highest overestimation by the different source term packages. For all parameterizations, the NBI tends to zero for the largest range (low wind conditions). Although all packages overestimate  $H_s$  at F, ST6 shows the highest overestimation in both short and medium ranges by up to approx. 50% compared to KOMEN. This suggests that ST6 feeds too much energy to the dominant frequency within these ranges.

A clear relation between NBI and  $\bar{X}_w$  is also evident in Fig. 4. The  $\bar{X}_w$  is an indication of how the width restricts the growth within the fjord. Similar to  $\bar{X}$ , the NBI is high for short-medium  $\bar{X}_w$  while it tends to zero for large  $\bar{X}_w$ . This indicates a degrading model performance when the fetch geometry becomes more narrow, which is especially evident for ST6. The majority of the high NBI (at F) cases are linked to southeast wave direction (yellow fetches/width in Fig. 1) which is characterized by strong wind channelling (Christakos et al., 2020a). All in all, at F the dimensionless width is a better explanation for the model performance than the dimensionless (effective) fetch, even though the effective fetch contains some information about the narrowness of the fetch geometry.

In the following we investigate two cases: (I) narrow fetch geometry without swell, and (II) narrow fetch geometry with mixed wind seaswell. Case I focuses on the most problematic area (location F) where the highest differences between the packages are observed and a clear link between fjord geometry and NBI exists. Location F, which is located at the junction between three narrow fjords, can be considered a natural laboratory for very narrow fetch conditions. The case II presents

a case of mixed sea state (locations D, A and B) under strong wind forcing at semi-closed and narrow fetch geometry.

#### 4.1. Case I: Narrow fetch geometry with no swell

On January 15, 2018, offshore winds greater than  $15 \text{ m s}^{-1}$  from southeast generated a strong local wind sea in location F (Fig. 5). During most of the time the dimensionless fetch is between  $10^2$  and  $10^3$  and the dimensionless width varies roughly from 70 and 350 at location F where high NBI is observed (Figs. 3 and 4). Although the complex orography caused wind channelling in the fjord, the high resolution WRF model has been shown to reproduce such local effects well (Christakos et al., 2020a).

The observed  $H_s$  in location F reached 1 m with  $\theta$  about  $130\text{--}150^\circ$  (Fig. 5). The  $T_p$  and  $T_{m01}$  ranged from 2.5 to 4 s and 2.5 to 3 s, respectively. Modelled and observed wind directions were in good agreement, varying from  $120\text{--}160^\circ$ . A slight overestimation of the modelled wind speed at buoy location F, of about  $2\text{--}3 \text{ m s}^{-1}$ , was observed. However, considering the complex fjord orography, the quality of the wind forcing can be characterized as good. Regarding  $H_s$ , we see large differences between the different source term packages. ST6 exhibits the highest values of  $H_s$  with up to 1 m difference compared to observations. The default package KOMEN shows the best performance with differences of at most 0.3 m compared to the observations. Similar results are observed for  $T_p$  and  $T_{m01}$ ; ST6 shows the largest over-estimation compared to the observed values.

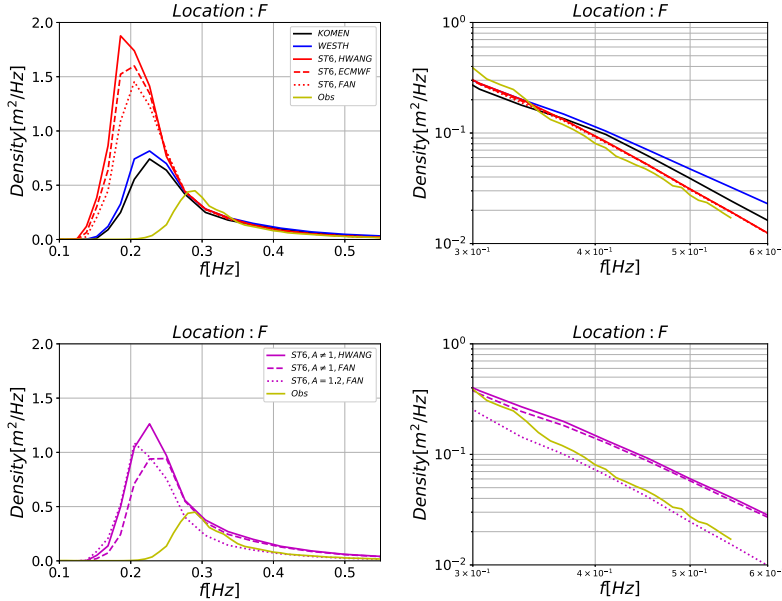


Fig. 8. Top: averaged frequency spectra for KOMEN, WESTH and ST6 ( $A = 1$  in  $S_{ds}$  and HWANG, FAN, and ECMWF drag formulations) simulations in the linear (left) and the logarithmic (right) scale for period January 14, 2018, at 18 UTC to January 15, 2018, at 18 UTC (case I) at F. Bottom: averaged frequency spectra for ST6 simulations using (i) actual  $A$  ( $A \neq 1$ ) in  $S_{ds}$  with HWANG/FAN and, (ii) a constant  $A = 1.2$  in  $S_{ds}$  with FAN in the linear (left) and the logarithmic (right) scale for the same period as the top panel.

The spatial variation of  $S_{in+ds}$ ,  $U_{10}$ , and  $H_s$  is presented in Fig. 6. The spatial variation of  $S_{in+ds}$  reflects the  $U_{10}$  variation (channelling) within the fjord. As expected, similarities in spatial variation between  $S_{in+ds}$ ,  $H_s$ , and  $T_p$  (not shown) are observed. Up to 40% of the fjord area has  $H_s > 1.5$  m and  $T_p > 4.5$  s in the ST6 simulations. The respective area for KOMEN and WESTH is much smaller and concentrated around buoy F.

To further analyse the model performance, the source terms  $S_{in}$ ,  $S_{ds}$ ,  $S_{nl4}$ , and their sum,  $S_{in+ds+nl4}$  are plotted as a function of  $f$  for four selected times from January 14, 2018, at 00 UTC (calm conditions) to January 15, 2018, at 09 UTC (peak of wind speed) (Fig. 7). ST6 shows much higher  $S_{in}$  peak levels than the other packages. More specifically, for the dominant waves the absolute values of  $S_{in}$  and  $S_{ds}$  are roughly an order of magnitude higher in ST6 than in KOMEN on January 15, 2018, at 09 UTC. Source terms of KOMEN and WESTH show similar performance with the latter giving slightly higher values. As expected,  $S_{nl4}$  reflects the magnitude of  $S_{in}$  and  $S_{ds}$ . Consequently, the sum  $S_{in+ds+nl4}$  in ST6 shows the highest values, about 3 times as high as in KOMEN. WESTH and KOMEN shows similar values, with the former being slightly higher.

The energy of the dominant waves is about 3–4 times as high in ST6 as the observed values (Fig. 8, top panel). KOMEN and WESTH overestimate the energy of the dominant waves by about 50%. In addition ST6 underestimates the peak frequency by about 0.1 Hz while KOMEN and WESTH underestimate it by about 0.05 Hz. The best performance is found with KOMEN both in terms of peak energy density and the location of the peak frequency. For the high-frequency tail ( $f > 0.3$  Hz), ST6 matches the observations, while KOMEN and WESTH show too high energy densities.

The high energy overestimation of the dominant waves in ST6 for such narrow fetch geometries merits further analysis. For this reason, we investigate the sensitivity of ST6 on: (i) wind drag formulations, and (ii) the narrowness  $A$ .

- (i) The wind drag formulations are used to scale the input wind forcing ( $U_{10}$ ) to  $u_*$ , which is applied to  $S_{in}$ . Applying ECMWF and FAN

wind drag formulas, the density level at the peak has reduced by 15% and 23%, respectively, while there is no negative impact on the good performance of the spectral tail (Fig. 8, top panel).

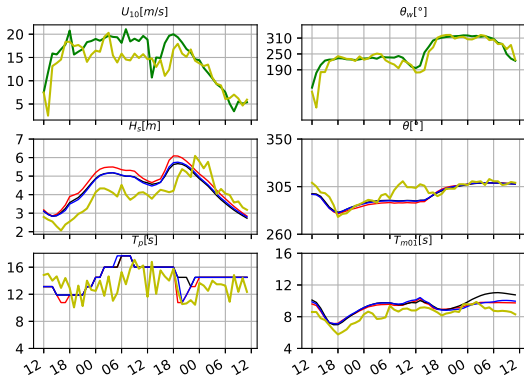
- (ii) As mentioned in Section 2.1.3, the narrowness  $A$  in  $S_{ds,ST6}$  is omitted by setting it to unity (default). Using the actual  $A$  ( $A \neq 1$ ) with the wind drag formulations by HWANG/FAN, we observe a reduction of the density level peak by about 33/50% (Fig. 8, bottom panel), thus almost matching the performance of the other packages. However, the use of the actual  $A$  yields an overestimation in the spectral tail. The use of FAN with a constant narrowness  $A = 1.2$  in  $S_{ds,ST6}$  shows similar results to when using  $A \neq 1$  for the dominant waves, with only a small negative bias for the spectral tail.

#### 4.2. Case II: Narrow fetch geometry with mixed wind sea-swell

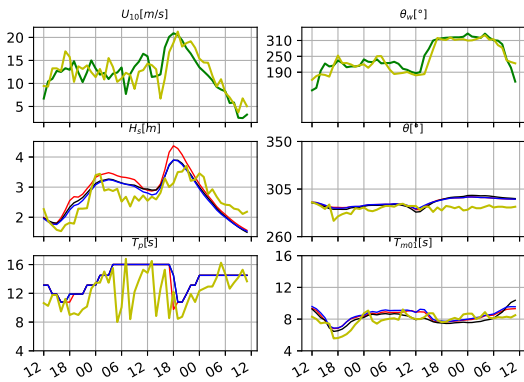
On December 26, 2016, a severe winter storm, known as Urd, passed the Norwegian Sea and reached the west coast of Norway. Significant wave heights up to 6 m were recorded in location D. Fig. 9 shows the time variation of the model and observed wind speed and wind direction for the storm Urd at location D, A, and B. The wind speed exceeded  $15 \text{ m s}^{-1}$  at location D, and reached  $20 \text{ m s}^{-1}$  at locations A and B. The model wind speed and direction agrees with observations at locations A and B, but the wind speed is slightly overestimated at D.  $H_s$  reached 3.6 m at A and 2.2 m at B. The peak wave period  $T_p$  and the mean wave period  $T_{m01}$  varied from 8 to 16 s and 4 to 10 s, respectively. The mean wave direction ( $\theta$ ) was westerly and northwesterly.

Differences between the source term packages are observed mainly in  $H_s$ , which is over-predicted by all packages, but WESTH and KOMEN perform best. They show similar performance for  $\theta$ , being in good accord with observed values. The packages behave nearly identically for  $T_p$ , following the observations. The high variation in the observations is likely caused by statistical variability, which is not expected to be reproduced by the model. In sheltered locations, swell energy is

Case II, Location : D



Case II, Location : A



Case II, Location : B

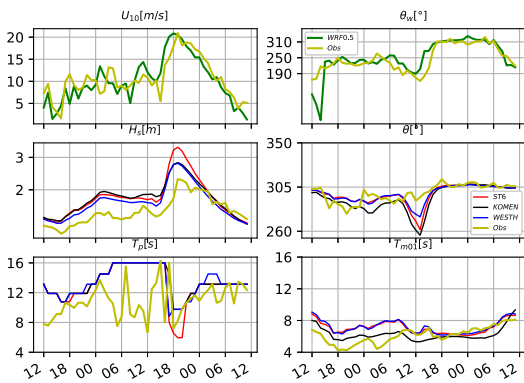


Fig. 9. Time series of wind speed ( $U_{10}$ ), wind direction, significant wave height, mean wave direction, and peak and mean period at locations D, A, and B (case II). Period: December 25, 2016, at 12 UTC to December 27, 2016, at 12 UTC.

less dominant compared to wind sea, thus the peak period is shifting between values of 8 s (old wind sea) and 16 s (swell). The model shows good performance for  $T_{m01}$  with some deviations observed between the

source term packages. At location B, WESTH and ST6 agree on the mean period  $T_{m01}$ , showing slightly higher values than those of KOMEN.

There are strong similarities in the spatial variation of  $S_{in+ds}$  magnitude (Fig. 10—top). KOMEN and WESTH show similar  $S_{in+ds}$  values while the values of ST6 are considerably higher, especially in Sulafjorden where strong wind channelling is observed (Fig. 10—middle). The  $S_{fric}$  and  $S_{brk}$  are significant only in the small shallow areas around islands off the fjord system (not shown).

ST6 shows the highest  $H_s$  values, offshore up to 10.7 m. It also shows the deepest penetration of high waves into the Sulafjorden, followed by WESTH and then KOMEN (Fig. 10—bottom). The lowest wave heights both offshore and within the fjord system are shown by KOMEN. Differences are mainly seen within the fjord system where ST6 shows higher  $H_s$  because of larger  $S_{in+ds}$  values compared to KOMEN and WESTH.

The spatial variation of  $T_p$  shows insignificant differences between the packages along the coast, since it is mainly affected by the boundary conditions (not shown). Along the coast  $T_p$  is 17.5 s, while being below 5 s within the fjord system. All the packages predict similarly the reduction of  $T_p$  outside Sulafjorden that are due to changes in the bathymetry. Differences in  $T_p$  are mainly observed in Sulafjorden where ST6 shows a deeper penetration of longer waves within the fjord.

To compare the ability of the packages to model the observed shape of spectra, Fig. 11 presents the average frequency spectra in the linear and the logarithmic scale. In location D, most exposed to the open sea, the different packages show quite similar spectral shapes and magnitudes. Some differences are detected in the inlet of Sulafjorden (location A) for frequencies  $f > 0.1$  Hz, and the differences are even more pronounced within Sulafjorden (location B). For the high frequency tail ( $f > 0.3$  Hz) the different source term packages perform quite similarly at location D. Deviations between the packages are detected at locations A and B where ST6 and WESTH show the best performance when evaluated against observations.

5. Discussion

The saturation-based white-capping approach (WESTH) provides the best model performance in terms of  $H_s$  in locations where mixed wind sea-swell conditions are observed. This is in accordance with findings of van der Westhuysen et al. (2007) who showed that the saturation-based formulation outperformed the pressure pulse approach of Komen in such mixed conditions. The results show a strong wind input in ST6, which is particularly problematic in case I with the extremely narrow fetch geometry.

In narrow fetch geometry with no swell, ST6 captures the energy of the high frequency tail well but overestimates strongly the energy of the dominant waves, yielding too high  $H_s$ . In these areas, the fetch geometry plays a crucial role in wave dynamics. Within the medium fetch range (fetches between 5 and 21 km under moderate to strong wind conditions) all the applied packages perform quite poorly (location F). This overestimation is especially strong for ST6 because of a strong  $S_{in+}$  which is unbalanced due to a weak  $S_{dk}$ .

The highest NBI is found within the medium range about  $\bar{X} = 10^3$  at narrow fetch geometry (location F), e.g. fetches at 20 km with a wind speed of about  $14 \text{ m s}^{-1}$ . For much larger scales, these dimensionless fetch values can be equivalent to a fetch of 100 km, with wind speeds at  $30 \text{ m s}^{-1}$ . Large values of NBI are also detected at approx.  $\bar{X}_w = 300$  in location F. For fjord areas, this represents widths of about 3 km, with a wind speed of about  $10 \text{ m s}^{-1}$ . If we scale it again to larger regions, it is approximately equivalent to a width of 20 km with wind speeds of  $25 \text{ m s}^{-1}$ . Therefore, the inaccuracies detected in this study might be relevant also for significantly larger water bodies during high winds.

Several factors can cause the high energy observed in narrow fetches by ST6. They can be grouped into two categories, (i) direct factors which are related to the formulation of wind input and white-capping, and (ii) indirect factors that are connected to effects triggered by e.g. non-linear interactions, wind drag, and forcing.

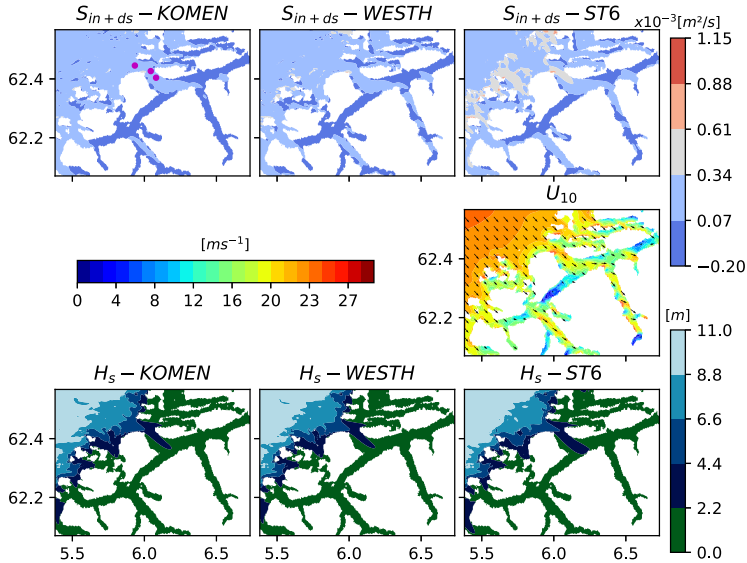


Fig. 10. Snapshot of spatial variation of  $S_{in} + S_{ds}$  (upper),  $U_{10}$  (middle), and  $H_s$  (lower) over the fjord system at December 26, 2016, at 18 UTC (case II). The buoy locations are marked with dots (upper left panel): D (westernmost buoy), A, and B (easternmost buoy).

### 5.1. (i) Direct factors

Rogers et al. (2012) found a problematic energy growth in ST6 at the young wave age stage due to (i) the quadratic relationship between  $S_{in}$  and inverse wave age, and (ii) the dependency of  $S_{in}$  on the spectral saturation  $B_n$  (Eq. (8)). In KOMEN,  $S_{in}$  has a linear dependency on the inverse wave age for all wind conditions. In WESTH, the relationship is linear for low winds and quadratic for stronger winds. The linear relationship in KOMEN potentially explains the relatively low  $S_{in}$  values.

The source term formulations of WESTH and ST6 use an isotropic spectral saturation. According to Ardhuin et al. (2010), using a direction-dependent saturation can allow for a control of directional spread and improve the overall results. According to Pettersson (2004) a narrow fetch geometry influences the directional distribution of the dominant waves. Hence, an isotropic white-capping might therefore not be fully appropriate for fjord wave modelling. Accounting for the directional spread in  $S_{ds,ST6}$  by using the actual narrowness  $A$  shows an improvement for the dominant waves but, as discussed by Rogers et al. (2012), it leads to lower dissipation in the high frequencies. In narrow fetch geometries, selecting a constant (not unity) narrowness (e.g.  $A = 1.2$  in case I) can improve the performance for both the larger (dominant) and shorter waves.

Babanin et al. (2010) suggested that dependence between  $T_{1,2}$  and the exceedance level ( $E - E_T$ ) should be linear. However, Rogers et al. (2003) found that a nonlinear relationship, obtained by setting  $p_1 = p_2 = 4$  (the default in SWAN), is essential to balance the strong  $S_{in}$ . In our case, these default values seem to provide still too weak  $S_{ds}$  and a further increase of nonlinearity by setting  $p_1 = p_2 = 6$  improves considerably the wave height estimates (not shown). However, this increases the dissipation in high frequencies with a negative impact on spectral tail.

Even if the model performance in exposed locations is generally good for ST6, there are inaccuracies regarding the density peak level, which describes the energy of the dominant waves. Rogers et al. (2012) presents a third dissipation term ( $T_3$  in their study, see also the Cumulative Steepness Method (CSM) by van Vledder and Hurdle (2002)

and Hurdle and van Vledder (2004)) which provides a formulation for the straining mechanism. In contrast to  $T_2$ , this term accounts for the change of the short wave steepness by the underlying longer waves. The effect can be considered important in the exposed fjord locations where short waves (local wind sea) coexist with non-breaking larger waves (swell or old wind sea). Its implementation in  $S_{ds}$  may provide a better balance to strong  $S_{in}$  under mixed swell-wind sea conditions. We expect that this term should have a minor effect on sheltered locations (with weak or no swell). However, more observational studies and numerical simulations are required to investigate this effect.

The wind input in the applied packages assume a stable air-sea boundary layer since changes in the air and sea temperatures or densities are not considered in their formulation ( $\rho_a/\rho_w$  is constant in SWAN). This assumption might not be appropriate in our study area. Norwegian fjord climate is associated with (i) rapid changes in weather conditions, e.g., sharp changes in air density by atmospheric front passages and (ii) proximity to land with fresh water discharges that influence the density ratio and consequently the wind input.

### 5.2. (ii) Indirect factors

Christakos et al. (2020a) found that WRF0.5 has an overall good performance in the fjord system. However, the evaluation is based on the 5 measurement locations and did not draw firm conclusions about the wind quality over the whole fjord system. Considering the complexity of the orography possible inaccuracies in wind forcing along the fjords are transferred to  $S_{in}$ , affecting the wave growth.

The energy growth in ST6 is much stronger than in the other packages. In contrast to older wind input formulations which add the bulk around the spectral peak, the  $S_{in}$  in ST6 adds more energy to higher frequencies (Rogers et al., 2012). This possibly affects the DIA which in turn will redistribute energy to lower frequencies more vigorously, growing the wave field faster compared to other formulations. Therefore, the resulting high density level at location F could be to some extent due to DIA. Liu et al. (2019) discussed that their ST6 results using DIA show higher sensitivity to fetch geometry compared to the Generalized Multiple DIA (Tolman, 2008, GMD) and

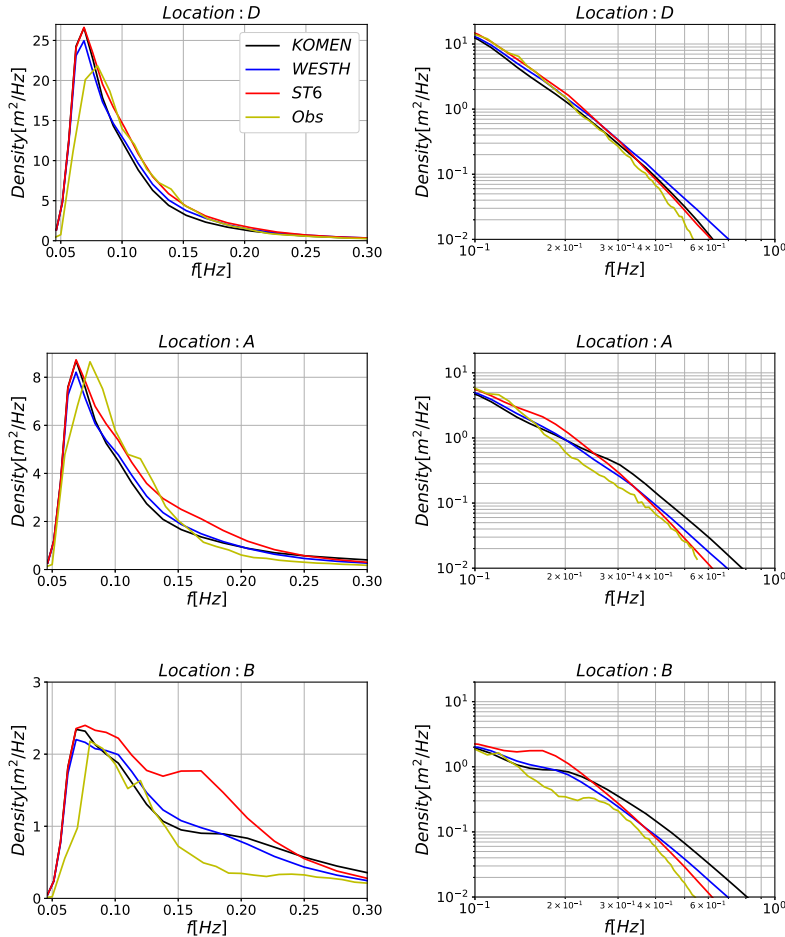


Fig. 11. Averaged frequency spectra in the linear (left) and the logarithmic (right) scale using different source term packages for period December 26, 2016, at 14 UTC to December 27, 2016, at 06 UTC (case II) at locations D, A, and B.

the Webb–Resio–Tracy method (Webb, 1978; Tracy and Resio, 1982, WRT).

The use of different wind drag formulations in narrow fetch conditions revealed their importance. The wind drag formulations that take into account the wave impact on  $u_*$  estimation using iterative methods, i.e., FAN and ECMWF, provide more accurate results than the default formulation in ST6. In narrow fetches even small changes in the vertical wind profile induced by waves can affect the spectral shape. Hence, accounting for the wave–atmosphere coupling can provide a more physical representation of  $u_*$  and, consequently, more accurate  $S_{in}$ .

There are other types of forcing which are not considered in the present study but might affect the fjord wave modelling. The rain, river run-off, surface currents and tides may play an important role in the fjord wave evolution. Rain affects the wind input and dissipation of surface waves (more details in Cavaleri et al. (2015)). During heavy rainfall or melting of snow or ice, river run-off creates freshwater plumes that can also influence the wave growth and direction. Surface currents and tides can affect the waves through several processes, such as a change of the relative wind speed, the

Doppler shift, the concertina effect (e.g. Ardhuin, 2019), wave refraction, and energy bunching/stretching. Future studies using a coupled ocean–wave–atmosphere system is needed to quantify and evaluate the importance of these effects in a fjord system.

## 6. Summary and conclusions

Accurate modelling of wave conditions in complex coastal areas is a challenging issue. In addition to the uncertainties due to the quality of the boundary wave conditions and the wind forcing, the choice of physics is found to be very important. We have investigated the performance of three different source term packages available in SWAN. The packages were evaluated by comparing their results against buoy measurements at five different locations, using both long-term statistics and detailed case studies.

All applied packages perform well for the most exposed locations (D and A). For the more sheltered locations, the packages show pronounced differences. The WESTH package provides the best overall performance in terms of  $H_s$  in most measurement locations with mixed swell-wind sea conditions (D, A, B, and C). The KOMEN package performs the best in terms of  $H_s$  in the location with no exposure

to the open sea (F). ST6 package shows a strong positive  $H_s$  bias in sheltered areas (no swell). For high frequencies the different source term packages perform quite similarly at the outermost location, while significant deviations between the packages are detected at locations A and B, where ST6 and WESTH are the most accurate.

In exposed areas a weak dependency between fetch geometry and model accuracy is found, as expected, because of the dominant role of swell. In narrow fjord areas with no swell, the fetch geometry has a distinct effect on model performance. In such areas, the narrow fetch combined with wind channelling induced by the steep mountains surrounding the fjord significantly affects the model results. These conditions give rise to large differences in the performance of the applied source packages. The effect that the fetch geometry has on the accuracy of  $H_s$  is best explained by the dimensionless width of the basin ( $\bar{X}_w$ ), as opposed to the dimensionless (effective) fetch. Values of  $\bar{X}_w$  that were found problematic for the wave model are possible even in larger scales during sufficiently strong wind.

In the fjord system, the deep-water source terms  $S_{in}$  and  $S_{ds}$  contribute the most to the total energy. The ST6 white-capping is too weak to balance the strong  $S_{in}$ , resulting in overestimation of density spectra and thus of  $H_s$ . Both cases show that ST6 is more sensitive to narrow fetch geometry and variations in the local wind speed than the other packages.

#### CRediT authorship contribution statement

**Konstantinos Christakos:** Conceptualization, Methodology, Software, Formal analysis, Investigation, Data curation, Writing - original draft, Writing - review & editing, Visualization. **Jan-Victor Björkqvist:** Conceptualization, Methodology, Investigation, Writing - review & editing. **Laura Tuomi:** Methodology, Supervision, Writing - review & editing. **Birgitte R. Furevik:** Methodology, Supervision, Writing - review & editing, Project administration. **Øyvind Breivik:** Methodology, Supervision, Writing - review & editing.

#### Declaration of competing interest

The authors declare that they have no known competing financial interests or personal relationships that could have appeared to influence the work reported in this paper.

#### Acknowledgements

We would like to thank the four reviewers for their thoughtful and insightful comments that helped in improving the study. Furthermore, we are thankful to Erick W. Rogers (Oceanography Division, Naval Research Laboratory, Stennis Space Center, Mississippi, USA) who provided the SWAN code (revision 358 of swancom2.ftn) for the estimation of narrowness in the white-capping of ST6. We are grateful to Lasse Lønseth (Fugro OCEANOR AS, Norway) and Øyvind Byrkjedal (Kjeller Vindteknikk AS, Norway) who provided the wave spectral data and the wind forcing data, respectively. The study was funded by the Norwegian Public Roads Administration under the Coastal Highway Route E39 project. The bathymetry data is derived by EMODnet Bathymetry Consortium (2018).

#### References

Aarnes, O.J., Breivik, Ø., Reistad, M., 2012. Wave extremes in the Northeast Atlantic. *J. Clim.* 25 (5), 1529–1543. <http://dx.doi.org/10.1175/JCLI-D-11-00132.1>.  
 Alves, J.H.G.M., Banner, M.L., 2003. Performance of a saturation-based dissipation-rate source term in modeling the Fetch-Limited Evolution of Wind Waves. *J. Phys. Oceanogr.* 33 (6), 1274–1298.  
 Amarouche, K., Akpinar, A., Bachari, N.E.I., Çakmak, R., Houma, F., 2019. Evaluation of a high-resolution wave hindcast model SWAN for the west mediterranean basin. *Appl. Ocean Res.* 84, 225–241.

Arduini, F., 2019. Ocean waves in geosciences.  
 Arduini, F., Bertotti, L., Bidlot, J., Cavaleri, L., Filippetto, V., Lefevre, J.-M., Wittmann, P., 2007. Comparison of wind and wave measurements and models in the Western Mediterranean Sea. *Ocean Eng.* 34, 526–541.  
 Arduini, F., Rogers, E., Babanin, A.V., Filippot, J.F., Magne, R., Roland, A., van der Westhuysen, A., Queffeuou, P., Lefevre, J.M., Aouf, L., Collard, F., 2010. Semi-empirical dissipation source functions for ocean waves. Part I: Definition, calibration, and validation. *J. Phys. Oceanogr.* 40 (9), 1917–1941.  
 Babanin, A.V., Tsagareli, K.N., Young, I.R., Walker, D.J., 2010. Numerical investigation of spectral evolution of wind waves. Part II: Dissipation term and evolution tests. *J. Phys. Oceanogr.* 40 (4), 667–683.  
 Banner, M.L., Gemmrich, J.R., Farmer, D.M., 2002. Multiscale measurements of ocean Wave Breaking probability. *J. Phys. Oceanogr.* 32, 3364–3375.  
 Battjes, J.A., Janssen, J.P., 1978. Energy loss and set-up due to breaking of random waves. In: *Proceedings of the Coastal Engineering Conference*, pp. 569–587.  
 Benoit, M., Marcos, F., Becq, F., 1997. Development of a third generation Shallow-Water Wave model with unstructured Spatial meshing. In: *Coastal Engineering 1996*, pp. 465–478, URL <https://ascelibrary.org/doi/abs/10.1061/9780784402429.037>.  
 Booij, N., Ris, R.C., Holthuijsen, L.H., 1999. A third-generation wave model for coastal regions: 1. Model description and validation. *J. Geophys. Res.: Oceans* 104 (C4), 7649–7666.  
 Bouws, E., Komen, G.J., 1983. On the balance between growth and dissipation in an extreme depth-limited wind-sea in the southern north sea. *J. Phys. Oceanogr.* 13 (9), 1653–1658. [http://dx.doi.org/10.1175/1520-0485\(1983\)013<1653:OTBBGA>2.0.CO;2](http://dx.doi.org/10.1175/1520-0485(1983)013<1653:OTBBGA>2.0.CO;2).  
 Breivik, Ø., Gusdal, Y., Furevik, B.R., Aarnes, O.J., Reistad, M., 2009. Nearshore wave forecasting and hindcasting by dynamical and statistical downscaling. *J. Mar. Syst.* 78 (2), S235–S243.  
 Bruserud, K., Haver, S., 2016. Comparison of wave and current measurements to NORA10 and NoNoCur hindcast data in the northern North Sea. *Ocean Dyn.* 66 (6), 823–838. <http://dx.doi.org/10.1007/s10236-016-0953-z>.  
 Cavaleri, L., Abdalla, S., Benetazzo, A., Bertotti, L., Bidlot, J.-R., Breivik, Ø., Carniel, S., Jensen, R.E., Portilla-Yandun, J., Rogers, W.E., Roland, A., Sanchez-Arcilla, A., Smith, J.M., Staneva, J., Toledo, Y., van Vledder, G., van der Westhuysen, A.J., 2018. Wave modelling in coastal and inner seas. *Prog. Oceanogr.*  
 Cavaleri, L., Barbariol, F., Benetazzo, A., 2020. Wind-wave modeling: Where we are, where to go. *J. Mar. Sci. Eng.* 8 (4), URL <https://www.mdpi.com/2077-1312/8/4/260>.  
 Cavaleri, L., Bertotti, L., 2004. Accuracy of the modelled wind and wave fields in enclosed seas. *Tellus A* 56 (2), 167–175. <http://dx.doi.org/10.3402/tellusa.v56i2.14398>.  
 Cavaleri, L., Bertotti, L., Bidlot, J.R., 2015. Waving in the rain. *J. Geophys. Res. C* 120 (5), 3248–3260.  
 Christakos, K., Furevik, B.R., Aarnes, O.J., Breivik, Ø., Tuomi, L., Byrkjedal, Ø., 2020a. The importance of wind forcing in fjord wave modelling. *Ocean Dyn.* 70 (1), 57–75. <http://dx.doi.org/10.1007/s10236-019-01323-w>.  
 Christakos, K., Varlas, G., Cheliotis, I., Spyrou, C., Aarnes, O.J., Furevik, B.R., 2020b. Characterization of wind-sea- and swell-induced wave energy along the Norwegian Coast. *Atmosphere* 11 (2), URL <https://www.mdpi.com/2073-4433/11/2/166>.  
 Christakos, K., Varlas, G., Reuder, J., Katsafados, P., Papadopoulos, A., 2014. Analysis of a low-level coastal jet off the western coast of Norway. *Energy Procedia* 53, 162–172.  
 Dee, D., Rosnay, P. d., Uppala, Simmons, Berrisford, Poli, P., Kobayashi, S., Andrae, U., Balmaseda, M., Balsamo, G., Bauer, Bechtold, Beljaars, de Berg, v., Bidlot, J., Bormann, N., Delsol, Dragani, R., Fuentes, M., Vitart, F., 2011. The ERA-interim reanalysis: Configuration and performance of the data assimilation system. *Q. J. R. Meteorol. Soc.* 137, 553–597.  
 DHI, 2017. MIKE 21 Spectral Wave Module, Scientific Documentation. Tech. Rep., Danish Hydraulic Institute.  
 EMODnet Bathymetry Consortium, 2018. EMODnet Digital Bathymetry (DTM 2018). In: Web. <http://dx.doi.org/10.12770/18f0d48-b203-4a65-94a9-5fd8b0ec35f6>.  
 Fan, Y., Lin, S.J., Held, I.M., Yu, Z., Tolman, H.L., 2012. Global ocean surface wave simulation using a coupled atmosphere-wave model. *J. Clim.* 25 (18), 6233–6252.  
 FUGRO, 2012. SEAWATCH wavescan Buoy. URL <https://www.fugro.com/docs/default-source/about-fugro-doc/ROVs/seawatch-wavescan-buoy-flyer.pdf>.  
 Furevik, B.R., Lønseth, L., Borg, A.L., Neshaug, V., Gausen, M., 2020. Oceanographic Observations for the Coastal Highway E39 project in Mid-Norway. The Norwegian Meteorological Institute, URL <https://thredds.met.no/thredds/catalog/obs/mast-svv-e39/catalog.html>.  
 Gunther, H., Hasselmann, S., Janssen, P., 1992. The WAM Model Cycle 4. Tech. Rep., Deutsches KlimaRechenZentrum, Hamburg, Germany.  
 Haakenstad, H., Breivik, Ø., Reistad, M., Aarnes, O.J., 2020. NORA10EI: A revised regional atmosphere-wave hindcast for the North Sea, the Norwegian Sea and the Barents Sea. *Int. J. Climatol.* <http://dx.doi.org/10.1002/joc.6458>.  
 Hasselmann, K., 1974. On the spectral dissipation of ocean waves due to white capping. *Bound.-Lay. Meteorol.* 6 (1), 107–127. <http://dx.doi.org/10.1007/BF00232479>.

- Hasselmann, K., Barnett, T.P., Bouws, E., Carlson, H., E. Cartwright, D., Enke, K., A Ewing, J., Giannop, H., E. Hasselmann, D., Kruseman, P., Meerburg, A., Muller, P., Olbers, D., Richter, K., Sell, W., Walden, H., 1973. Measurements of wind-wave growth and swell decay during the Joint North Sea Wave Project (JONSWAP). *Deut. Hydrogr. Z.* 8, 1–95.
- Hasselmann, D., Bösenberg, J., 1991. Field measurements of wave-induced pressure over wind-sea and swell. *J. Fluid Mech.* 230, 391–428.
- Hasselmann, S., Hasselmann, K., Allender, J., Barnett, T., 1985. Computations and parameterizations of the nonlinear energy transfer in a Gravity-Wave spectrum. Part II: Parameterizations of the nonlinear energy transfer for application in wave models. *J. Phys. Oceanogr.* 15 (11), 1378–1391. [http://dx.doi.org/10.1175/1520-0485\(1985\)015<1378:CAPOTN>2.0.CO;2](http://dx.doi.org/10.1175/1520-0485(1985)015<1378:CAPOTN>2.0.CO;2)
- Herman, A., Wojtysiak, K., Moskalik, M., 2019. Wind wave variability in Hornsund fjord, west Spitsbergen. *Estuar. Coast. Shelf Sci.*
- Hersbach, H., Bell, B., Berrisford, P., Hirahara, S., Horányi, A., Muñoz-Sabater, J., Nicolas, J., Peubey, C., Radu, R., Schepers, D., Simmons, A., Soci, C., Abdalla, S., Abellan, X., Balsamo, G., Bechtold, P., Biavati, G., Bidlot, J., Bonavita, M., De Chiara, G., Dahlgren, P., Dee, D., Diamantakis, M., Dragani, R., Flemming, J., Forbes, R., Fuentes, M., Geer, A., Haimberger, L., Healy, S., Hogan, R.J., Hólm, E., Janisková, M., Keeley, S., Laloyaux, P., Lopez, P., Lupu, C., Radnoti, G., de Rosnay, P., Rozum, I., Vamborg, F., Villaume, S., Thépaut, J.N., 2020. The ERA5 global reanalysis. *Q. J. R. Meteorol. Soc.* 146 (730), 1999–2049.
- Holthuijsen, L., 2007. *Waves in Oceanic and Coastal Waters*. Cambridge University Press.
- Hurdle, D.P., van Vledder, G.P., 2004. Improved spectral wave modelling of whitecapping dissipation in swell sea systems. In: *Proceedings of the International Conference on Offshore Mechanics and Arctic Engineering - OMAE*, Vol. 2. pp. 539–544.
- Janssen, P.A., 1991. Quasi-linear theory of wind-wave generation applied to wave forecasting. *J. Phys. Oceanogr.* 21 (11), 1631–1642. [http://dx.doi.org/10.1175/1520-0485\(1991\)021<1631:QLTOWW>2.0.CO;2](http://dx.doi.org/10.1175/1520-0485(1991)021<1631:QLTOWW>2.0.CO;2)
- Komen, G.J., Cavaleri, L., Donelan, M., Hasselmann, K., Hasselmann, S., Janssen, P.A.E.M., 1994. *Dynamics and Modelling of Ocean Waves*. Cambridge University Press, Cambridge.
- Komen, G.J., Hasselmann, S., Hasselmann, K., 1984. On the existence of a fully Developed Wind-Sea spectrum. *J. Phys. Oceanogr.* 14 (8), 1271–1285. [http://dx.doi.org/10.1175/1520-0485\(1984\)014<1271:OTEQAF>2.0.CO;2](http://dx.doi.org/10.1175/1520-0485(1984)014<1271:OTEQAF>2.0.CO;2)
- Lavidas, G., Polinder, H., 2019. North sea wave database (NSWD) and the need for reliable resource data: A 38 year database for metocean and wave energy assessments. *Atmosphere* 10 (9), URL <https://www.mdpi.com/2073-4433/10/9/551>.
- Liu, Q., Rogers, W.E., Babanin, A.V., Young, I.R., Romero, L., Zieger, S., Qiao, F., Guan, C., 2019. Observation-based source terms in the third-generation wave model WAVEWATCH III: Updates and verification. *J. Phys. Oceanogr.* 49 (2), 489–517. <http://dx.doi.org/10.1175/JPO-D-18-0137.1>
- Pallares, E., Sánchez-Arcilla, A., Espino, M., 2014. Wave energy balance in wave models (SWAN) for semi-enclosed domains—Application to the Catalan coast. *Cont. Shelf Res.* 87, 41–53, URL <http://www.sciencedirect.com/science/article/pii/S0278434314001022>.
- Pettersson, H., 2004. Wave growth in a narrow bay. *Finn. Inst. Mar. Res. -Contrib.* 9, 1–33.
- Plant, W.J., 1982. A relationship between wind stress and wave slope. *J. Geophys. Res.*: Oceans 87 (C3), 1961–1967. <http://dx.doi.org/10.1029/JC087iC03p01961>.
- Reistad, M., Breivik, Ø., Haakenstad, H., Aarnes, O.J., Furevik, B.R., Bidlot, J.-R., 2011. A high-resolution hindcast of wind and waves for the North Sea, the Norwegian Sea, and the Barents Sea. *J. Geophys. Res.*: Oceans 116 (C5).
- Rogers, W.E., Babanin, A.V., Wang, D.W., 2012. Observation-consistent input and whitecapping dissipation in a model for wind-generated surface waves: Description and simple calculations. *J. Atmos. Ocean. Technol.* 29 (9), 1329–1346. <http://dx.doi.org/10.1175/JTECH-D-11-00092.1>
- Rogers, W.E., Hwang, P.A., Wang, D.W., 2003. Investigation of wave growth and decay in the SWAN model: Three regional-scale applications. *J. Phys. Oceanogr.* 33 (2), 366–389. [http://dx.doi.org/10.1175/1520-0485\(2003\)033<0366:JOWGAD>2.0.CO;2](http://dx.doi.org/10.1175/1520-0485(2003)033<0366:JOWGAD>2.0.CO;2)
- Roland, A., Arduin, F., 2014. On the developments of spectral wave models: numerics and parameterizations for the coastal ocean. *Ocean Dyn.* 64 (6), 833–846. <http://dx.doi.org/10.1007/s10236-014-0711-z>
- Semedo, A., Vettor, R., Breivik, Ø., Sterl, A., Reistad, M., Lima, D., 2014. The wind sea and swell waves climate in the Nordic seas. *Ocean Dyn.* 65.
- Skamarock, W.C., Klemp, J.B., Dudhia, J., Gill, D.O., Barker, M., Duda, K.G., Huang, X.Y., Wang, W., Powers, J.G., 2008. *A Description of the Advanced Research WRF Version 3*. Tech. Rep., National Center for Atmospheric Research, pp. 1–113.
- Snyder, R.L., Dobson, F.W., Elliott, J.A., Long, R.B., 1981. Array measurements of atmospheric pressure fluctuations above surface gravity waves. *J. Fluid Mech.* 102, 1–59.
- Stefananos, C., Furevik, B.R., Knutsen, Ø., Christakos, K., 2020. Nearshore wave modelling in a norwegian fjord. *J. Offshore Mech. Arct. Eng.*
- Stopa, J.E., Arduin, F., Babanin, A., Zieger, S., 2015. Comparison and validation of physical wave parameterizations in spectral wave models. *Ocean Model.* 103, 2–17.
- SWAN team, 2017. *Scientific and technical documentation SWAN cycle III version 41.20*.
- Taylor, K.E., 2001. Summarizing multiple aspects of model performance in a single diagram. *J. Geophys. Res.* 106, 7183–7192.
- The Wamdi Group, 1988. *The WAM Model - A third generation ocean wave prediction model*. *J. Phys. Oceanogr.* 18 (12), 1775–1810.
- The WAVEWATCH III® Development Group, 2016. *User Manual and System Documentation of WAVEWATCH III® Version 5.16*. Tech. Rep. 329, NOAA/NWS/NCEP/MMAB.
- Tolman, H.L., 2008. Optimum Discrete Interaction Approximations for wind waves. Part 3: Generalized multiple DIAs. *Environmental Modeling Center Marine Modeling and Analysis Branch*. Tech. Rep., U.S. Department of Commerce, National Oceanic and Atmospheric Administration, National Weather Service, National Centers for Environmental Prediction.
- TOMAWAC, 2020. *User manual*. URL [http://wiki.opentemac.org/doku.php?id=user\\_manual\\_tomawac](http://wiki.opentemac.org/doku.php?id=user_manual_tomawac).
- Tracy, B.A., Resio, D.T., 1982. *Theory and Calculation of The Nonlinear Energy Transfer between Sea Waves in deep Water Wave Information Studies of U.S. Coastlines*. Tech. Rep., Hydraulics Laboratory U.S. Army Engineer Waterways Experiment Station.
- van Vledder, G.P., Hurdle, D.P., 2002. Performance of formulations for whitecapping in wave prediction models. In: *Proceedings of the International Conference on Offshore Mechanics and Arctic Engineering - OMAE*, Vol. 2. pp. 155–163.
- van Vledder, G.P., Sander, S.T., McConochie, J.D., 2016. Source term balance in a severe storm in the Southern North Sea. *Ocean Dyn.* 66 (12), 1681–1697.
- Wang, J., Li, L., Jakobsen, J.B., Haver, S.K., 2018. Metocean conditions in a Norwegian Fjord. *J. Offshore Mech. Arct. Eng.*
- Webb, D.J., 1978. Non-linear transfers between sea waves. *Deep Sea Res.* 25, 279–298.
- van der Westhuysen, A.J., Zijlema, M., Battjes, J.A., 2007. Nonlinear saturation-based whitecapping dissipation in SWAN for deep and shallow water. *Coast. Eng.* 54 (2), 151–170, URL <http://www.sciencedirect.com/science/article/pii/S037838390600127X>.
- Yan, L., 1987. *An Improved Wind Input Source Term for Third Generation Ocean Wave Modelling*. Rep. No. 87-8, Royal Dutch Meteor. Inst..
- Zieger, S., Babanin, A.V., Rogers, W.E., Young, I.R., 2015. Observation-based source terms in the third-generation wave model WAVEWATCH. *Ocean Model.* 96, 2–25, URL <http://www.sciencedirect.com/science/article/pii/S1463500315001237>.
- Zijlema, M., van Vledder, G.P., Holthuijsen, L.H., 2012. Bottom friction and wind drag for wave models. *Coast. Eng.* 65, 19–26.



# Paper III

## **The impact of surface currents on the wave climate in narrow fjords**

Christakos, K., J.V. Björkqvist, Ø. Breivik, L. Tuomi, B.R. Furevik, and J. Albretsen  
*Ocean Modelling, under review.*



# Bibliography

- Aalberg, A. (2017), Analysis and Design Bjørnefjorden Floating Cable-Stayed Bridge subjected to Large Ship Collisions and Extreme Environmental Loads (Master thesis), *NTNU, Trondheim, Norway*. 1
- Aarnes, O. J., Ø. Breivik, and M. Reistad (2012), Wave Extremes in the Northeast Atlantic, *Journal of Climate*, 25(5), 1529–1543, doi:10.1175/JCLI-D-11-00132.1. 1.1.1
- Aarnes, O. J., M. Reistad, Ø. Breivik, E. Bitner-Gregersen, L. Ingolf Eide, O. Gramstad, A. K. Magnusson, B. Natvig, and E. Vanem (2017), Projected changes in significant wave height toward the end of the 21st century: Northeast Atlantic, *Journal of Geophysical Research: Oceans*, 122(4), 3394–3403, doi:10.1002/2016JC012521. 1.1.1
- Abdolali, A., A. Roland, A. van der Westhuysen, J. Meixner, A. Chawla, T. J. Hesser, J. M. Smith, and M. D. Sikiric (2020), Large-scale hurricane modeling using domain decomposition parallelization and implicit scheme implemented in WAVEWATCH III wave model, *Coastal Engineering*, 157, doi:10.1016/j.coastaleng.2020.103656. 4
- Albretsen, J., A. K. Sperrevik, A. Staalstrøm, A. D. Sandvik, F. Vikebø, and L. Asplin (2011), NorKyst-800 Report No. 1 User Manual and technical descriptions, *Tech. rep.*, Institute of Marine Research. 2.2.3
- Alves, J. H. G. M., and M. L. Banner (2003), Performance of a Saturation-Based Dissipation-Rate Source Term in Modeling the Fetch-Limited Evolution of Wind Waves, *Journal of Physical Oceanography*, 33(6), 1274–1298. 2.1.3
- Amarouche, K., A. Akpınar, N. E. I. Bachari, R. Çakmak, and F. Houma (2019), Evaluation of a high-resolution wave hindcast model SWAN for the West Mediterranean basin, *Applied Ocean Research*, 84, 225–241, doi:10.1016/j.apor.2019.01.014. 1
- Ardhuin, F., E. Rogers, A. V. Babanin, J. F. Filipot, R. Magne, A. Roland, A. van der Westhuysen, P. Queffelec, J. M. Lefevre, L. Aouf, and F. Collard (2010), Semiempirical dissipation source functions for ocean waves. Part I: Definition, calibration, and validation, *Journal of Physical Oceanography*, 40(9), 1917–1941, doi:10.1175/2010JPO4324.1. 2.1.3, 4
- Asplin, L., J. Albretsen, I. A. Johnsen, and A. D. Sandvik (2020), The hydrodynamic foundation for salmon lice dispersion modeling along the Norwegian coast, *Ocean Dynamics*, 70, 1151–1167, doi:10.1007/s10236-020-01378-0. 4

- Babanin, A. (2011), *Breaking and Dissipation of Ocean Surface Waves*, Cambridge University Press, doi:10.1017/CBO9780511736162. 1, 4
- Babanin, A. V., K. N. Tsagareli, I. R. Young, and D. J. Walker (2010), Numerical investigation of spectral evolution of wind waves. Part II: Dissipation term and evolution tests, *Journal of Physical Oceanography*, 40(4), 667–683, doi:10.1175/2009JPO4370.1. 2.1.3
- BarentsWatch (2016), Enhancing wave alerts - Warnings of cross seas have been added by BarentsWatch to its wave forecasting service, making travel by sea off Norway even more secure, <https://www.barentswatch.no/en/articles/Kryssende-bolger>. 1.1.2
- Barnett, T. P. (1968), On the generation, dissipation, and prediction of ocean wind waves, *Journal of Geophysical Research*, 73(2), 513–529, doi:10.1029/JB073i002p00513. 2.1.3
- Barstad, I., and S. Grønås (2005), Southwesterly flows over southern Norway-mesoscale sensitivity to large-scale wind direction and speed, *Tellus. Series A, Dynamic meteorology and oceanography*, 57(2), 136–152, doi:10.3402/tellusa.v57i2.14627. 2.2.1
- Barstad, I., and S. Grønås (2006), Dynamical structures for southwesterly airflow over southern Norway: the role of dissipation, *Tellus. Series A, Dynamic meteorology and oceanography*, 58(1), 2–18, doi:10.1111/j.1600-0870.2006.00152.x. 2.2.1
- Battjes, J. A. (1994), Shallow water wave modelling, in *Int. Symp. Waves-Physical and Numerical Modeling*, edited by M. Isaacson and M. Quick, pp. –, University of British Columbia, Vancouver. 1.2
- Battjes, J. A., and J. P. Janssen (1978), Energy Loss and Set-Up Due to Breaking of Random Waves, in *Proceedings of the Coastal Engineering Conference*, pp. 569–587, doi:10.9753/icce.v16.32. 2.1.3
- Benetazzo, A., F. Fedele, G. Gallego, P.-C. Shih, and A. Yezzi (2012), Offshore stereo measurements of gravity waves, *Coastal Engineering*, 64, doi:10.1016/j.coastaleng.2012.01.007. 4
- Benetazzo, A., F. Barbariol, F. Bergamasco, A. Torsello, S. Carniel, and M. Sclavo (2016), Stereo wave imaging from moving vessels: Practical use and applications, *Coastal Engineering*, 109, 114–127, doi:10.1016/j.coastaleng.2015.12.008. 4
- Bergamasco, F., A. Torsello, M. Sclavo, F. Barbariol, and A. Benetazzo (2017), WASS: An open-source pipeline for 3D stereo reconstruction of ocean waves, *Computers and Geosciences*, 107, doi:10.1016/j.cageo.2017.07.001. 4
- Bidlot, J.-R., D. J. Holmes, P. A. Wittmann, R. Lalbeharry, and H. S. Chen (2002), Intercomparison of the Performance of Operational Ocean Wave Forecasting Systems with Buoy Data, *Weather and Forecasting*, 17(2), 287–310, doi:10.1175/1520-0434(2002)017<0287:IOTPOO>2.0.CO;2. 1

- Booij, N., R. C. Ris, and L. H. Holthuijsen (1999), A third-generation wave model for coastal regions: 1. Model description and validation, *Journal of Geophysical Research: Oceans*, 104(C4), 7649–7666, doi:10.1029/98JC02622. 1.1.2, 2.1.3
- Bouws, E., and G. J. Komen (1983), On the Balance Between Growth and Dissipation in an Extreme Depth-Limited Wind-Sea in the Southern North Sea, *Journal of Physical Oceanography*, 13(9), 1653–1658, doi:10.1175/1520-0485(1983)013<1653:OTBBGA>2.0.CO;2. 2.1.3
- Breivik, Ø., Y. Gusdal, B. R. Furevik, O. J. Aarnes, and M. Reistad (2009), Nearshore wave forecasting and hindcasting by dynamical and statistical downscaling, *Journal of Marine Systems*, 78, S235–S243, doi:10.1016/j.jmarsys.2009.01.025. 1.1.2, 2.2.3
- Bruserud, K., , and S. Haver (2016), Comparison of wave and current measurements to NORA10 and NoNoCur hindcast data in the northern North Sea, *Ocean Dynamics*, 66(6), 823–838, doi:10.1007/s10236-016-0953-z. 1.1.1
- Carrasco, A., and Y. Gusdal (2014), Validation of the operational wave model WAM for the years 2012 and 2013, *Tech. rep.*, Norwegian Meteorological Institute. 1.1.1
- Cavaleri, L., and P. M. Rizzoli (1981), Wind wave prediction in shallow water: Theory and applications, *Journal of Geophysical Research: Oceans*, 86(C11), 10,961–10,973, doi:10.1029/JC086iC11p10961. 2.1.3, 2.1.3
- Cavaleri, L., and M. Sclavo (2006), The calibration of wind and wave model data in the Mediterranean Sea, *Coastal Engineering*, 53(7), 613 – 627, doi:10.1016/j.coastaleng.2005.12.006. 1
- Cavaleri, L., L. Bertotti, and J. R. Bidlot (2015), Waving in the rain, *Journal of Geophysical Research C: Oceans*, 120(5), 3248–3260, doi:10.1002/2014JC010348. 4
- Cavaleri, L., A. Benetazzo, F. Barbariol, J. R. Bidlot, and P. A. Janssen (2017), The draupner event: The large wave and the emerging view, *Bulletin of the American Meteorological Society*, 98(4), 729–736, doi:10.1175/BAMS-D-15-00300.1. 1.1.1
- Cavaleri, L., S. Abdalla, A. Benetazzo, L. Bertotti, J.-R. Bidlot, Ø. Breivik, S. Carniel, R. E. Jensen, J. Portilla-Yandun, W. E. Rogers, A. Roland, A. Sanchez-Arcilla, J. M. Smith, J. Staneva, Y. Toledo, G. van Vledder, and A. J. van der Westhuysen (2018), Wave modelling in coastal and inner seas, *Progress in Oceanography*, doi:10.1016/j.pocean.2018.03.010. 1, 1.1.2
- Christakos, K. (2013), Characterization of the coastal marine atmospheric boundary layer (MABL) for wind energy applications (MSc thesis), *University of Bergen, Bergen, Norway*. 2.2.1
- Christakos, K. (2021), Ferjefri-E39\_MET-Norway (Metocean analysis tools for Ferjefri E39 dataset), *GitHub repository*. 2.2.4
- Christakos, K., G. Varlas, J. Reuder, P. Katsafados, and A. Papadopoulos (2014), Analysis of a Low-level Coastal Jet off the Western Coast of Norway, *Energy Procedia*, 53, 162 – 172, doi:10.1016/j.egypro.2014.07.225. 2.2.1

- Christakos, K., I. Cheliotis, G. Varlas, and G.-J. Steeneveld (2016), Offshore Wind Energy Analysis of Cyclone Xaver over North Europe, *Energy Procedia*, 94, 37–44, doi:10.1016/j.egypro.2016.09.187. 2.2.1
- Christakos, K., G. Varlas, I. Cheliotis, C. Spyrou, O. J. Aarnes, and B. R. Furevik (2020), Characterization of Wind-Sea- and Swell-Induced Wave Energy along the Norwegian Coast, *Atmosphere*, 11(2), doi:10.3390/atmos11020166. 2.2.1, 2.2.2, 2.1, 4
- Dai, J., B. J. Leira, T. Moan, and H. S. Alsos (2021), Effect of wave inhomogeneity on fatigue damage of mooring lines of a side-anchored floating bridge, *Ocean Engineering*, 219, doi:10.1016/j.oceaneng.2020.108304. 1
- Dankert, H., and W. Rosenthal (2004), Ocean surface determination from X-band radar-image sequences, *J. Geophys. Res.*, 109, 1–11, doi:10.1029/2003JC002130. 4
- Dee, D., d. Rosnay P, Uppala, Simmons, Berrisford, P. Poli, S. Kobayashi, U. Andrae, M. Balmaseda, G. Balsamo, Bauer, Bechtold, Beljaars, v. de Berg, J. Bidlot, N. Bormann, Delsol, R. Dragani, M. Fuentes, and F. Vitart (2011), The ERA-Interim reanalysis: Configuration and performance of the data assimilation system, *Quarterly Journal of the Royal Meteorological Society*, 137, 553–597, doi:10.1002/qj.828. 2.2.3
- Donelan, M. A., and A. K. Magnusson (2017), The Making of the Andrea Wave and other Rogues, *Scientific Reports*, 7, doi:10.1038/srep44124. 1.1.1
- Dunham, K. K. (2016), Coastal Highway Route E39 - Extreme Crossings, in *Transportation Research Procedia*, vol. 14, pp. 494–498, Elsevier B.V., doi:10.1016/j.trpro.2016.05.102. 1
- Dysthe, K., H. E. Krogstad, and P. Müller (2008), Oceanic rogue waves, *Annu. Rev. Fluid Mech.*, 40, 287–310, doi:10.1146/annurev.fluid.40.111406.102203. 1.1.1
- Eidesen, A. O., S. Bystedt, E. Jersin, Drægebø. Einar, R. Teisrud, and O. C. Borge (2000), Hurtigbåten MS Sleipners forlis 26. november 1999 (NOU 2000:31), *Tech. rep.*, Undersøkelseskommisjonen oppnevnt av Justis- og politidepartementet, Oslo. 1.1.2
- Eldeberky, Y., and J. A. Battjes (1996), Spectral modeling of wave breaking: Application to Boussinesq equations, *Journal of Geophysical Research C: Oceans*, 101(C1), doi:10.1029/95JC03219. 2.1.3
- EMODnet Bathymetry Consortium (2018), EMODnet Digital Bathymetry (DTM 2018). 2.2.3
- Fan, Y., S. J. Lin, I. M. Held, Z. Yu, and H. L. Tolman (2012), Global ocean surface wave simulation using a coupled atmosphere-wave model, *Journal of Climate*, 25(18), 6233–6252, doi:10.1175/JCLI-D-11-00621.1. 2.1.3

- Fedele, F., A. Benetazzo, G. Gallego, P. C. Shih, A. Yezzi, F. Barbariol, and F. Ardhuin (2013), Space-time measurements of oceanic sea states, *Ocean Modelling*, 70, 103–115, doi:10.1016/j.ocemod.2013.01.001. 4
- Fergestad, D., O. Økland, C. Stefanakos, C. T. Stansberg, E. Croonenborghs, L. Eliassen, and G. Eidnes (2019), LFCS Review report Environmental conditions. Wind, wave and current in coastal areas, *Tech. rep.*, SINTEF Ocean AS. 4
- Forristall, G. Z. (2000), Wave crest distributions: Observations and second-order theory, *Journal of Physical Oceanography*, 30(8), doi:10.1175/1520-0485(2000)030<1931:WCDOAS>2.0.CO;2. 1.1.1
- Furevik, B. R. (2017), Kystnaere bølgevarsler på Barentswatch og yr, *Tech. rep.*, Meteorologisk institutt. 1.1.2
- Furevik, B. R., and H. Haakenstad (2012), Near-surface marine wind profiles from rawinsonde and NORA10 hindcast, *Journal of Geophysical Research: Atmospheres*, 117(D23), doi:10.1029/2012JD018523. 1.1.1
- Furevik, B. R., and M. Reistad (2006), A forecasting service for the Trondheim shiplane, in *WISE Meeting (Waves In Shallow water Environment)*. 1.1.2
- Furevik, B. R., L. Lønseth, A. L. Borg, V. Neshaug, and M. Gausen (2020), Oceanographic observations for the Coastal Highway E39 project in Mid-Norway, doi:doi.org/10.21343/ef2d-jp97. 2.2.4
- Gelci, R., H. Cazalé, and J. Vassal (1956), Utilization des diagrammes de propagation a la prevision energetique de la houle, *Bulletin d'information du Comite d'Oceanographie et d'Etude des Cotes*, 8(4), 160–197. 2.1.3
- Guddal, J. (1985), The Norwegian Wave Model NOWAMO, in *Ocean Wave Modeling*, pp. 187–191, Springer US, Boston, MA. 1.1.1
- Guenther, H., S. Hasselmann, and P. Janssen (1992), The WAM model cycle 4., *Tech. rep.*, Deutsches KlimaRechenZentrum, Hamburg, Germany. 2.1.3
- Guimarães, P. V., F. Ardhuin, F. Bergamasco, F. Leckler, J. F. Filipot, J. S. Shim, V. Dulov, and A. Benetazzo (2020), A data set of sea surface stereo images to resolve space-time wave fields, *Scientific Data*, 7(1), doi:10.1038/s41597-020-0492-9. 4
- Gusdal, Y., A. Carrasco, B. R. Furevik, and O. Saetra (2010), Validation of the Operational Wave Model WAM and SWAN-2009, *Tech. Rep. 18*, Norwegian Meteorological Institute. 1.1.2
- Haakenstad, H., Ø. Breivik, M. Reistad, and O. J. Aarnes (2020), NORA10EI: A revised regional atmosphere-wave hindcast for the North Sea, the Norwegian Sea and the Barents Sea, *International Journal of Climatology*, doi:10.1002/joc.6458. 1.1.1
- Hasselmann, K. (1974), On the spectral dissipation of ocean waves due to white capping, *Boundary-Layer Meteorology*, 6(1), 107–127, doi:10.1007/BF00232479. 2.1.3

- Hasselmann, K., T. P. Barnett, E. Bouws, H. Carlson, D. E. Cartwright, K. Enke, J. A. Ewing, H. Gienapp, D. E. Hasselmann, P. Kruseman, A. Meerburg, P. Muller, D. Olbers, K. Richter, W. Sell, and H. Walden (1973), Measurements of wind-wave growth and swell decay during the Joint North Sea Wave Project (JONSWAP), *Deut. Hydrogr. Z.*, 8, 1–95. 2.1.3
- Hasselmann, S., and K. Hasselmann (1985), Computations and Parameterizations of the Nonlinear Energy Transfer in a Gravity-Wave Spectrum. Part I: A New Method for Efficient Computations of the Exact Nonlinear Transfer Integral., *Journal of Physical Oceanography*, 15(11), Nov. 1985, doi:10.1175/1520-0485(1985)015<1369:capotn>2.0.co;2. 2.1.3
- Hasselmann, S., K. Hasselmann, J. H. Allender, and T. P. Barnett (1985), Computations and Parameterizations of the Nonlinear Energy Transfer in a Gravity-Wave Spectrum. Part II: Parameterizations of the Nonlinear Energy Transfer for Application in Wave Models, *Journal of Physical Oceanography*, 15(11), 1378–1391, doi: 10.1175/1520-0485(1985)015<1378:CAPOTN>2.0.CO;2. 2.1.3
- Haug, O. (1968), *A numerical model for prediction of sea and swell*, *Meteorologiske annaler*, vol. 5, no. 4, Aschehoug, Oslo. 1.1.1
- Haug, O. (1981), *Hindcasting the wind and wave climate of Norwegian waters : frequency distributions, geographical, long-term and seasonal variations, operational statistics, data access*, Det Norske meteorologiske institutt, Oslo. 1.1.1
- Hersbach, H., B. Bell, P. Berrisford, S. Hirahara, A. Horányi, J. Muñoz-Sabater, J. Nicolas, C. Peubey, R. Radu, D. Schepers, A. Simmons, C. Soci, S. Abdalla, X. Abellan, G. Balsamo, P. Bechtold, G. Biavati, J. Bidlot, M. Bonavita, G. De Chiara, P. Dahlgren, D. Dee, M. Diamantakis, R. Dragani, J. Flemming, R. Forbes, M. Fuentes, A. Geer, L. Haimberger, S. Healy, R. J. Hogan, E. Hólm, M. Janisková, S. Keeley, P. Laloyaux, P. Lopez, C. Lupu, G. Radnoti, P. de Rosnay, I. Rozum, F. Vamborg, S. Villaume, and J. N. Thépaut (2020), The ERA5 global reanalysis, *Quarterly Journal of the Royal Meteorological Society*, 146(730), 1999–2049, doi:10.1002/qj.3803. 2.2.3
- Holthuijsen, L. (2007), *Waves in Oceanic and Coastal Waters*, Cambridge University Press, doi:10.1017/CBO9780511618536. 1.2, 2.1.1, 2.1.3, 2.1.3
- Huang, W., X. Liu, and E. W. Gill (2017), Ocean wind and wave measurements using X-band marine radar: A comprehensive review, *Remote Sensing*, 9(12), doi:10.3390/rs9121261. 4
- Hurdle, D. P., and G. P. van Vledder (2004), Improved spectral wave modelling of white-capping dissipation in swell sea systems, in *Proceedings of the International Conference on Offshore Mechanics and Arctic Engineering - OMAE*, vol. 2, pp. 539–544, doi:10.1115/OMAE2004-51562. 4
- Isobe, M. (1987), A Parabolic Equation Model for Transformation of Irregular Waves Due to Refraction, Diffraction and Breaking, *Coastal Engineering in Japan*, 30(1), 33–47, doi:10.1080/05785634.1987.11924463. 1.1.2

- Izumiya, T., and K. Horikawa (1987), On the Transformation of Directional Random Waves Under Combined Refraction and Diffraction, *Coastal Engineering in Japan*, 30(1), 49–65, doi:10.1080/05785634.1987.11924464. 1.1.2
- Janssen, P. A. E. M. (2008), Progress in ocean wave forecasting, *Journal of Computational Physics*, 227(7), 3572 – 3594, doi:10.1016/j.jcp.2007.04.029. 1
- Janssen, P. A. E. M., and J.-R. Bidlot (2018), Progress in Operational Wave Forecasting, *Procedia IUTAM*, 26, 14 – 29, doi:10.1016/j.piutam.2018.03.003. 1
- Jonassen, M. O. (2012), Local- and mesoscale variability of winds in the complex topography of southwestern Norway and Iceland, Ph.D. thesis, University of Bergen, Bergen. 2.2.1
- Katsafados, P., G. Varlas, A. Papadopoulos, C. Spyrou, and G. Korres (2018), Assessing the Implicit Rain Impact on Sea State During Hurricane Sandy (2012), *Geophysical Research Letters*, doi:10.1029/2018GL078673. 4
- Kirby, J. T. (1986), Higher-order approximations in the parabolic equation method for water waves, *Journal of Geophysical Research*, 91(C1), 933, doi:10.1029/jc091ic01p00933. 1.1.2
- Komen, G. J., S. Hasselmann, and K. Hasselmann (1984), On the Existence of a Fully Developed Wind-Sea Spectrum, *Journal of Physical Oceanography*, 14(8), 1271–1285, doi:10.1175/1520-0485(1984)014<1271:OTEOAF>2.0.CO;2. 2.1.3
- Laxague, N. J. M., and C. J. Zappa (2020), The Impact of Rain on Ocean Surface Waves and Currents, *Geophysical Research Letters*, 47(7), e2020GL087287, doi:10.1029/2020GL087287. 4
- Le Méhauté, B., and J. D. Wang (1982), Wave Spectrum Changes on Sloped Beach, *Journal of the Waterway, Port, Coastal and Ocean Division*, 108(1), 33–47, doi:10.1061/JWPCDX.0000284. 1.1.2
- Li, J. G. (2011), Global transport on a spherical multiple-cell grid, *Monthly Weather Review*, 139(5), doi:10.1175/2010MWR3196.1. 4
- Li, J. G. (2012), Propagation of ocean surface waves on a spherical multiple-cell grid, *Journal of Computational Physics*, 231(24), doi:10.1016/j.jcp.2012.08.007. 4
- Li, J. G., and A. Saulter (2014), Unified global and regional wave model on a multi-resolution grid, *Ocean Dynamics*, 64(11), doi:10.1007/s10236-014-0774-x. 4
- Lin, Y., S. Dong, Z. Wang, and C. Guedes Soares (2019), Wave energy assessment in the China adjacent seas on the basis of a 20-year SWAN simulation with unstructured grids, *Renewable Energy*, 136, doi:10.1016/j.renene.2019.01.011. 4
- Liu, Q., W. E. Rogers, A. V. Babanin, I. R. Young, L. Romero, S. Zieger, F. Qiao, and C. Guan (2019), Observation-Based Source Terms in the Third-Generation Wave Model WAVEWATCH III: Updates and Verification, *Journal of Physical Oceanography*, 49(2), 489–517, doi:10.1175/JPO-D-18-0137.1. 4

- Longuet-Higgins, M. S. (1957), On the transformation of a continuous spectrum by refraction, *Mathematical Proceedings of the Cambridge Philosophical Society*, 53(1), 226–229, doi:10.1017/S0305004100032163. 1.1.2
- Magnusson, A., and M. Donelan (2013), The Andrea Wave Characteristics of a Measured North Sea Rogue Wave, *Journal of Offshore Mechanics and Arctic Engineering*, 135, 31,101–31,108, doi:10.1115/1.4023800. 1.1.1
- Magnusson, A. K., K. Trulsen, E. M. Bitner-Gregersen, O. J. Aarnes, and M. P. Malila (2019), Three sisters measured as a triple rogue wave group, in *Proceedings of the International Conference on Offshore Mechanics and Arctic Engineering - OMAE*, vol. 3, doi:10.1115/OMAE2019-96837. 1.1.1
- Mao, M., A. J. van der Westhuysen, M. Xia, D. J. Schwab, and A. Chawla (2016), Modeling wind waves from deep to shallow waters in Lake Michigan using unstructured SWAN, *Journal of Geophysical Research: Oceans*, 121(6), doi:10.1002/2015JC011340. 4
- Martínez-Asensio, A., M. Marcos, G. Jordà, and D. Gomis Bosch (2013), Calibration of a new wind-wave hindcast in the Western Mediterranean, *Journal of Marine Systems*, doi:10.1016/j.jmarsys.2013.04.006. 1
- Massey, T. C., M. E. Anderson, J. M. Smith, J. Gomez, and R. Jones (2011), STWAVE: Steady-State Spectral Wave Model Users Manual for STWAVE, Version 6.0, *Tech. rep.*, US Army Corps of Engineers. 1.1.2
- Mathiesen, M. (1987), Wave refraction by a current whirl, *Journal of Geophysical Research: Oceans*, 92(C4), 3905–3912, doi:10.1029/JC092iC04p03905. 1.1.2
- Miles, J. W. (1957), On the generation of surface waves by shear flows, *Journal of Fluid Mechanics*, 3(2), 185–204, doi:10.1017/S0022112057000567. 2.1.3
- Müller, M., M. Homleid, K.-I. Ivarsson, M. A. O. Køltzow, M. Lindskog, K. H. Midtbø, U. Andrae, T. Aspelién, L. Berggren, D. Bjørge, P. Dahlgren, J. Kristiansen, R. Randriamampianina, M. Ridal, and O. Vignes (2017), AROME-MetCoOp: A Nordic Convective-Scale Operational Weather Prediction Model, *Weather and Forecasting*, 32(2), 609–627, doi:10.1175/WAF-D-16-0099.1. 2.2.3
- Nieto Borge, J. C., K. Reichert, and J. Dittmer (1999), Use of nautical radar as a wave monitoring instrument, *Coastal Engineering*, 37(3-4), doi:10.1016/S0378-3839(99)00032-0. 4
- Nieto Borge, J. C., P. Jarabo-Amores, D. De La Mata-Moya, and F. López-Ferreras (2006), Estimation of ocean wave heights from temporal sequences of X-band marine radar images, in *European Signal Processing Conference*. 4
- Nieto Borge, J. C., K. Hessner, M.-P. Jarabo-Amores, and D. de la Mata-Moya (2008), Signal-to-noise ratio analysis to estimate ocean wave heights from X-band marine radar image time series, *Radar, Sonar & Navigation, IET*, 2, 35 – 41, doi:10.1049/iet-rsn:20070027. 4

- NORSOK N-003:2017 (2017), Actions and action effects, *Tech. rep.*, Standard Norge, Oslo. 1.1.1
- Oceanweather Inc. (2018), History of Oceanweather, <https://www.oceanweather.com/about/history.html>. 1.1.1
- O'Reilly, W. C., and R. T. Guza (1993), A comparison of two spectral wave models in the Southern California Bight, *Coastal Engineering*, 19(3-4), 263–282, doi:10.1016/0378-3839(93)90032-4. 1.1.2
- Petterson, H. (2004), Wave growth in a narrow bay, Ph.D. thesis, University of Helsinki. 4
- Phillips, O. M. (1957), On the generation of waves by turbulent wind, *Journal of Fluid Mechanics*, 2(5), 417–445, doi:10.1017/S0022112057000233. 2.1.3
- Pierson, W. J. (1966), Computer based procedures for preparing global wave forecasts and wind field analyses capable of using wind data obtained by a spacecraft, in *Sixth Naval Hydrodynamics Symposium*, vol. 2. 2.1.3
- Plant, W. J. (1982), A relationship between wind stress and wave slope, *Journal of Geophysical Research: Oceans*, 87(C3), 1961–1967, doi:10.1029/JC087iC03p01961. 2.1.3
- Ponce de León, S., and A. R. Osborne (2020), Role of nonlinear four-wave interactions source term on the spectral shape, *Journal of Marine Science and Engineering*, 8(4), doi:10.3390/jmse8040251. 4
- Reistad, M., Ø. Breivik, H. Haakenstad, O. J. Aarnes, B. R. Furevik, and J.-R. Bidlot (2011), A high-resolution hindcast of wind and waves for the North Sea, the Norwegian Sea, and the Barents Sea, *Journal of Geophysical Research: Oceans*, 116(C5), doi:10.1029/2010JC006402. 1.1.1, 2.2.3, 2.2.3
- Rogers, W. E., and D. W. Wang (2007), Directional validation of wave predictions, *Journal of Atmospheric and Oceanic Technology*, 24(3), doi:10.1175/JTECH1990.1.4
- Rogers, W. E., A. V. Babanin, and D. W. Wang (2012), Observation-Consistent Input and Whitecapping Dissipation in a Model for Wind-Generated Surface Waves: Description and Simple Calculations, *Journal of Atmospheric and Oceanic Technology*, 29(9), 1329–1346, doi:10.1175/JTECH-D-11-00092.1. 2.1.3
- Segtnan, O. H., T. Lothe, M. Mathiesen, K. Christakos, and A. K. Meyer (2013), Wave forecasting along the Norwegian coastline: lifesaving knowledge available to everyone, *Tech. rep.*, Polytec R&D Institute, Haugesund, doi:10.13140/RG.2.2.13522.15043. 1.1.2
- Semedo, A., R. Vettor, Ø. Breivik, A. Sterl, M. Reistad, and D. Lima (2014), The wind sea and swell waves climate in the Nordic seas, *Ocean Dynamics*, 65, doi:10.1007/s10236-014-0788-4. 1.1.1, 2.2.1

- Skamarock, W. C., J. B. Klemp, J. Dudhia, D. O. Gill, M. Barker, K. G. Duda, X. Y. Huang, W. Wang, and J. G. Powers (2008), A description of the Advanced Research WRF Version 3, *Tech. rep.*, National Center for Atmospheric Research. 2.2.3
- Skjæveland, H., and H. J. Sætre (2016), *Norwegian Deepwater Programme 1996-2016: summary report*, Norwegian Deepwater Programme, Stavanger. 1.1.1
- Smith, J. M., T. Hesser, A. Roland, and M. Bryant (2018), Validation of unstructured WAVEWATCH III for nearshore waves, *Coastal Engineering Proceedings*, 1(36), doi:10.9753/icce.v36.waves.55. 4
- Smith, J. M., T. Hesser, M. A. Bryant, A. Roland, and A. Cox (2020), Advances in the unstructured WAVEWATCH III and application to hurricane Dorian, *Coastal Engineering Proceedings*, -(36v), doi:10.9753/icce.v36v.waves.42. 4
- Snyder, R. L., F. W. Dobson, J. A. Elliott, and R. B. Long (1981), Array measurements of atmospheric pressure fluctuations above surface gravity waves, *Journal of Fluid Mechanics*, 102, 1–59, doi:10.1017/S0022112081002528. 2.1.3
- Solbrekke, I. M., N. G. Kvamstø, and A. Sorteberg (2020), Offshore wind power intermittency: The effect of connecting production sites along the Norwegian continental shelf, *Wind Energy Science Discussions*, pp. 1–27, doi:10.5194/wes-2020-67. 1.1.1
- Stefanakos, C., B. R. Furevik, Ø. Knutsen, and K. Christakos (2020), Nearshore Wave Modelling in a Norwegian Fjord, *Proceedings of the ASME 2020 39th International Conference on Ocean, Offshore and Arctic Engineering*, 6B:Ocean Engineering. 1.1.2
- Stewart, R. H. (2008), *Introduction To Physical Oceanography*, Texas A&M University. 2.2.4
- SWAN team (2017), Scientific and technical documentation SWAN Cycle III version 41.20. 2.1.3, 2.1.3, 2.1.3, 4
- Tamura, H., T. Waseda, Y. Miyazawa, and K. Komatsu (2008), Current-induced modulation of the ocean wave spectrum and the role of nonlinear energy transfer, *Journal of Physical Oceanography*, 38(12), doi:10.1175/2008JPO4000.1. 4
- The Norwegian Ministry of Transport and Communications (2013), Meld. St. 26 (2012–2013) Report to the Storting (White Paper) Summary - National Transport Plan 2014–2023, *Tech. rep.*, The Norwegian Ministry of Transport and Communications. 1
- The Wamdi Group (1988), The WAM Model - A Third Generation Ocean Wave Prediction Model, *Journal of Physical Oceanography*, 18(12), 1775–1810, doi: 10.1175/1520-0485(1988)018<1775:TWMTGO>2.0.CO;2. 1.1.1, 2.1.3, 2.1.3
- The WAVEWATCH III® Development Group (2016), User manual and system documentation of WAVEWATCH III® version 5.16, *Tech. Rep.* 329, NOAA/NWS/NCEP/MMAB. 2.1.3, 2.1.3

- Tolman, H. L. (2008), Optimum Discrete Interaction Approximations for wind waves. Part 3: Generalized multiple DIAs. Environmental Modeling Center Marine Modeling and Analysis Branch, *Tech. rep.*, U.S. Department of Commerce, National Oceanic and Atmospheric Administration, National Weather Service, National Centers for Environmental Prediction. 4
- Torsethaugen, K., M. Mathiesen, S. Løvås, A. Lothe, W. Kanczynski, J. Guddal, and M. Reistad (1998), Varsel om farlige sjøforhold på Norskekysten. Bølgevarsling ved Stad, *Tech. rep.*, SINTEF. 1.1.2
- Tracy, B. A., and D. T. Resio (1982), Theory and calculation of the nonlinear energy transfer between sea waves in deep water, *Tech. rep.*, Hydraulics Laboratory U.S. Army Engineer Waterways Experiment Station. 4
- Undén, P., L. Rontu, H. Järvinen, P. Lynch, J. Calvo-Sanchez, G. Cats, J. Cuxart, K. Eerola, C. Fortelius, and J. García-Moya (2002), HIRLAM-5 scientific documentation, *Tech. rep.*, Sveriges meteorologiska och hydrologiska institut. 2.2.3
- Uppala, S., P. Kallberg, A. J. Simmons, U. Andrae, V. Da Costa Bechtold, M. Fiorino, J. K. Gibson, J. Haseler, A. Hernandez-Carrascal, G. A. Kelly, X. Li, K. Onogi, S. Saarinen, N. Sokka, R. Allan, E. Andersson, K. Arpe, M. Balmaseda, A. Beljaars, and J. Woollen (2005), The ERA-40 re-analysis, *Quarterly Journal of the Royal Meteorological Society*, 131, 2961–3012, doi:10.1256/qj.04.176. 2.2.3
- van der Westhuysen, A. J., M. Zijlema, and J. A. Battjes (2007), Nonlinear saturation-based whitecapping dissipation in SWAN for deep and shallow water, *Coastal Engineering*, 54(2), 151 – 170, doi:10.1016/j.coastaleng.2006.08.006. 2.1.3
- van Vledder, G. P., and D. P. Hurdle (2002), Performance of formulations for whitecapping in wave prediction models, in *Proceedings of the International Conference on Offshore Mechanics and Arctic Engineering - OMAE*, vol. 2, pp. 155–163, doi:10.1115/OMAE2002-28146. 4
- Varlas, G., K. Christakos, I. Cheliotis, A. Papadopoulos, and G.-J. Steeneveld (2017), Spatiotemporal variability of marine renewable energy resources in Norway, *Energy Procedia*, 125, 180 – 189, doi:10.1016/j.egypro.2017.08.171. 1.1.1
- Varlas, G., V. Vervatis, C. Spyrou, E. Papadopoulou, A. Papadopoulos, and P. Kat-safados (2020), Investigating the impact of atmosphere-wave-ocean interactions on a Mediterranean tropical-like cyclone, *Ocean Modelling*, 153, doi:10.1016/j.ocemod.2020.101675. 4
- Vieira, M., P. V. Guimarães, N. Violante-Carvalho, A. Benetazzo, F. Bergamasco, and H. Pereira (2020), A low-cost stereo video system for measuring directional wind waves, *Journal of Marine Science and Engineering*, 8(11), doi:10.3390/jmse8110831. 4
- Virtanen, P., R. Gommers, T. E. Oliphant, M. Haberland, T. Reddy, D. Cournapeau, E. Burovski, P. Peterson, W. Weckesser, J. Bright, S. J. van der Walt, M. Brett, J. Wilson, K. J. Millman, N. Mayorov, A. R. J. Nelson, E. Jones, R. Kern, E. Larson,

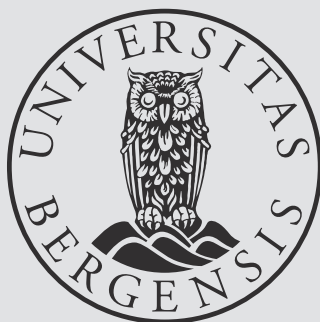
- C. J. Carey, I. Polat, Y. Feng, E. W. Moore, J. VanderPlas, D. Laxalde, J. Perktold, R. Cimrman, I. Henriksen, E. A. Quintero, C. R. Harris, A. M. Archibald, A. H. Ribeiro, F. Pedregosa, P. van Mulbregt, A. Vijaykumar, A. P. Bardelli, A. Rothberg, A. Hilboll, A. Kloeckner, A. Scopatz, A. Lee, A. Rokem, C. N. Woods, C. Fulton, C. Masson, C. Häggström, C. Fitzgerald, D. A. Nicholson, D. R. Hagen, D. V. Pasechnik, E. Olivetti, E. Martin, E. Wieser, F. Silva, F. Lenders, F. Wilhelm, G. Young, G. A. Price, G.-L. Ingold, G. E. Allen, G. R. Lee, H. Audren, I. Probst, J. P. Dietrich, J. Silterra, J. T. Webber, J. Slavič, J. Nothman, J. Buchner, J. Kulick, J. L. Schönberger, J. V. de Miranda Cardoso, J. Reimer, J. Harrington, J. L. C. Rodríguez, J. Nunez-Iglesias, J. Kuczynski, K. Tritz, M. Thoma, M. Newville, M. Kümmerer, M. Bolingbroke, M. Tartre, M. Pak, N. J. Smith, N. Nowaczyk, N. Shebanov, O. Pavlyk, P. A. Brodtkorb, P. Lee, R. T. McGibbon, R. Feldbauer, S. Lewis, S. Tygier, S. Sievert, S. Vigna, S. Peterson, S. More, T. Pudlik, T. Oshima, T. J. Pingel, T. P. Robitaille, T. Spura, T. R. Jones, T. Cera, T. Leslie, T. Zito, T. Krauss, U. Upadhyay, Y. O. Halchenko, Y. Vázquez-Baeza, and S. . Contributors (2020), SciPy 1.0: fundamental algorithms for scientific computing in Python, *Nature Methods*, 17(3), 261–272, doi:10.1038/s41592-019-0686-2. 2.2.4
- Wang, J., L. Li, J. B. Jakobsen, and S. K. Haver (2018), Metocean Conditions in a Norwegian in Relation to the Floating Bridge Design Fjord, *Journal of Offshore Mechanics and Arctic Engineering*, doi:10.1115/1.4041534. 1.1.2
- Wang, W. (2020), Large-Scale Phase-Resolved Wave Modelling for the Norwegian Coast, Ph.D. thesis, Norwegian University of Science and Technology. 1.1.2
- Webb, D. J. (1978), Non-linear transfers between sea waves, *Deep Sea Research*, 25, 279–298. 4
- Welch, P. (1967), The use of fast Fourier transform for the estimation of power spectra: A method based on time averaging over short, modified periodograms, *IEEE Transactions on Audio and Electroacoustics*, 15, 70–73. 2.2.4
- Whitham, G. B. G. B. (1974), *Linear and nonlinear waves*, 636 pp., Wiley. 2.1.2, 2.1.3
- Yamaguchi, M., L. H. Holthuijsen, M. Hino, and Y. Hatada (1988), A new hybrid parametrical wave prediction model taking the wave directionality into account, *Doboku Gakkai Ronbunshu*, 1988(399), 193–202. 2.1.3
- Yan, L. (1987), An improved wind input source term for third generation ocean wave modelling, *Rep. No. 87-8, Royal Dutch Meteor. Inst.* 2.1.3
- Young, I. R., W. Rosenthal, and F. Ziemer (1985), A three-dimensional analysis of marine radar images for the determination of ocean wave directionality and surface currents., *Journal of Geophysical Research*, 90(C1), doi:10.1029/JC090iC01p01049. 4
- Zakharov, V. E., and A. N. Pushkarev (1999), Diffusion model of interacting gravity waves on the surface of deep fluid, *Nonlinear Processes in Geophysics*, 6(1), 1–10, doi:10.5194/npg-6-1-1999. 2.1.3

- Zijlema, M. (2010), Computation of wind-wave spectra in coastal waters with SWAN on unstructured grids, *Coastal Engineering*, 57(3), doi:10.1016/j.coastaleng.2009.10.011. 4
- Zijlema, M., G. P. van Vledder, and L. H. Holthuijsen (2012), Bottom friction and wind drag for wave models, *Coastal Engineering*, 65, 19–26, doi:10.1016/j.coastaleng.2012.03.002. 2.1.3





Graphic design: Communication Division, UIB / Print: Skjipes Kommunikasjon AS



[uib.no](http://uib.no)

ISBN: 9788230866290 (print)  
9788230848005 (PDF)